# Search Strategy Applicable for Breakup Fragments in the Geostationary Region

上津原, 正彦

https://doi.org/10.15017/1398351

# Search Strategy Applicable for Breakup Fragments in the Geostationary Region

Masahiko Uetsuhara

Department of Aeronautics and Astronautics

Kyushu University

A thesis submitted for the degree of

*Doctor of Engineering*

Thesis Committee

Chief examiner: Prof. Dr. Toshiya Hanada
Department of Aeronautics and Astronautics
Faculty of Engineering
Kyushu University

Co-examiner: Prof. Dr. Shinji Hokamoto
Department of Aeronautics and Astronautics
Faculty of Engineering
Kyushu University

Co-examiner: Dr. Toshifumi Yanagisawa
Innovative Technology Research Center
Aerospace Research and Development Directorate
Japan Aerospace Exploration Agency

Day of the defense

1 August 2013

# Abstract

This dissertation proposes an effective search strategy applicable for fragmentation debris generated by energetic breakups of large space objects, e.g., satellites and rocket upper-stages, in the geostationary region. There are two definitive breakups in the geostationary region whose occurrences were occasionally confirmed by observations soon after the breakups. Past observation campaigns for the geostationary region have been found thousands of uncatalogued space objects, which may be associated with breakups. Moreover, it is confirmed that some of large space objects in the geostationary region have experienced unintended orbital change, i.e., orbital anomaly, that might be associated with breakup. Thus, search for the fragmentation debris will directly contribute to verify relations between uncatalogued space objects, breakups, and suspected orbital anomalies for the better understandings of current situations in the geostationary region.

The search strategy to be proposed in this dissertation utilizes orbital debris modeling techniques that describe debris generation and orbit propagation. The orbital debris modeling can predict behaviors of individual and group of fragmentation debris at breakups and also at observations. The search strategy, thus, enables effective observation planning, sensitive detection, straightforward origin identification, and breakup event characterization.

This dissertation introduces five principal roles required for the search strategy and verifies the roles in each chapter. The second chapter formulates the search strategy based on orbital debris modeling techniques. The third chapter addresses the deterministic origin identification of fragmentation debris, which enables simultaneous search for multiple breakup events and identification of unconfirmed breakups. The fourth chapter addresses the probabilistic origin identification of fragmentation debris, which enables characterization of breakup scale and improvement of orbital debris modeling in the search strategy. The fifth chapter

formulates breakup event characterization methodologies including fragmentation profile assessment and breakup scale assessment. The breakup scale assessment is demonstrated by applying a Bayesian approach combined with the probabilistic origin identification technique. The sixth chapter addresses unconfirmed breakup identification by evaluating uncertainties of unconfirmed breakups, and by applying the deterministic origin identification technique.

Along with theoretical confirmations of the search strategy to be addressed in each chapter, this dissertation also conducts empirical confirmations of the search strategy. The empirical confirmations utilize ground-based optical measurement techniques, which is a common approach for the geostationary objects observation. Optical sensor to be used consists of a small aperture telescope ($\leq$ 1 m) equipped with a charge coupled devise camera. Through the theoretical and empirical confirmations from the second chapter to the sixth chapter, this dissertation will finally establish the effective search strategy that contributes to define current situation in the geostationary region.

# Acknowledgements

I would like to acknowledge all the persons who have motivated my research activities and lives while enrolled at Kyushu University. First of all, I would like to express my deep gratitude to my supervisor Prof. Dr. Toshiya Hanada at Kyushu University. He always educated me about essentials of researches and to find such essentials by myself. This dissertation would never be completed without his supervision.

I would like to give special thanks to Dr. Toshifumi Yanagisawa and Mr. Hirohisa Kurosaki at Japan Aerospace Exploration Agency and Dr. Yukihito Kitazawa at IHI corporation. Dr. Yanagisawa and Mr. Kurosaki acceralated this research with their great expertise in optical observations of orbital debris. Dr. Kitazawa supported this research by organizing people, research meetings, and contracts. I would like to show my deep gratitude to Dr. Daisuke Kinoshita at National Central University and Dr. Andrew Wang at Academia Sinica for their dedicated contributions to realize the observation campaign conducted between the JAXA Nyukasa Observatory and the NCU Lulin Observatory in 2011. A lot of important outcomes of this research were acquired from the observation campaign. I would like to deeply acknowledge Dr. Tomoko Fujiwara and Dr. Hitoshi Yamaoka at Kyushu University. They have joined this research since the beginning and gave me a lot of important advices and supports. I wish to acknowledge Japan Society for the Promotion of Science for supporting me by the fellowship program.

I wish to thank students and staffs of the Space Systems Dynamics Laboratory at Kyushu University and my friends. They always made my university life fruitful and unforgettable. To conclude the acknowledgement, I would like to thank my family for understanding me and for encouraging my life.

# Contents

# List of Figures

## LIST OF FIGURES

## LIST OF FIGURES

# List of Tables

# Glossary

**A/m** Area-to-mass ratio

**CCD** Charge-coupled device

**COGO** Classification of geosynchronous objects

**CT** Correlated target

**DBT** Detect-before-track

**ESA** European space agency

**FOV** Field of view

**FPGA** Field gate programmable array

**GEO** Geosynchronous Earth orbit

**GF** Geocentric earth-fixed coordinate

**GI** Geocentric inertial coordinate

**GMST** Greenwich mean sidereal time

**ID** International designator

**ISON** International scientific optical network

**JAXA** Japan aerospace exploration agency

**JNO** JAXA Nyukasa observatory; located at Nagano prefecture, Japan

**k-NN** k nearest neighbors

**LOT** Lulin one-meter telescope

**MC** Monte Carlo

**NASA** National aeronautics and space administration

**NCU** National central university

**OD** Orbital debris

**RCS** Radar cross-section

**SC#** Satellite catalog number

**SOCIT** Satellite orbital debris characterization impact test

**SRP** Solar radiation pressure

**SSN** Space surveillance network

**TAOS** Taiwan American occultation survey

**TBD** Track-before-detect

**TF** Topocentric earth-fixed coordinate

**TLE** Two line elements

**Tracklet** A series of signals associated with a space object

**UCT** Uncorrelated target

**USSTRATCOM** United states strategic command

**UT** Universal time

# 1

# Introduction

The geostationary region, which consists of the geosynchronous Earth orbit (GEO) and its vicinity, is the unique and valuable region where hundreds of infrastructures such as communications, weather, and data-relay satellites are in operation. Along with these valuable satellites, a large number of defunct artificial space objects as known as orbital debris (OD) exist inside the geostationary region. As the growth of solid state image sensors technologies such as charge-coupled device (CCD) sensor and complementary metal-oxide-semiconductor (CMOS) sensor, intensive optical surveys for the geostationary regions have been started since 1990s and begun to reveal the space objects population in the geostationary region (Schildknecht *et al.*, 1999; Talent *et al.*, 1997). For example, observations performed by the European Space Agency (ESA) using the 1 m aperture Tenerife telescope have indicated that the GEO population, to a limiting diameter of approximately 10 cm, exceeds the cataloged population by a factor of two (Schildknecht *et al.*, 2000).

As of the end of 2012, a total of 1369 artificial space objects exist inside the geostationary region according to the classification of the geosynchronous objects (COGO) published by ESA (Flohrer, 2013). Of those, only 422 satellites are now in operation. It should be noted that COGO defines the geostationary region as orbits with mean motion between 0.9 and 1.1 revolutions per day, eccentricity smaller than 0.2 and inclination below 70 deg. Orbital data in COGO is constructed by two sources: the Space Surveillance Network (SSN) catalog maintained by United States Strategic Command (USSTRATCOM), and additional data provided by the International Scientific Optical Network (ISON) (Molotov *et al.*, 2008). The SSN catalog records 1149 individual GEO objects down to a limiting diameter of 1 m in size as of May 2013

(Space-Track, 2013). On the other hand, ISON have been monitored a total of 1704 individual GEO objects down to a limiting diameter of 10 cm in size as of January 2012 by organizing 50 or more optical telescopes around the world (Molotov *et al.*, 2012)(See Figure 1.1 for its magnitude distribution). The difference in population between the SSN catalog and ISON's observation results might come from existence of numerous OD generated by fragmentations of satellites or rockets, i.e., breakups. This dissertation defines such breakup-related OD as fragments or breakup fragments, or fragmentation debris. 490 GEO objects in the ISON database are grouped as fragmentation debris and undermined type objects, which can be regarded as OD. The number of such OD to be discovered will increase exponentially with improving sensitivity limit of optical sensors (Schildknecht *et al.*, 2001). OD have been causing serious threat to operational satellites since the congestion of high demand orbits such as polar orbits in the low Earth orbit region, and of course, the geostationary region. The geostationary region is at once precious and delicate; the natural decay by atmospheric drag does not work for GEO objects because it is far from the Earth thermosphere, which means GEO satellites, upper stages, and even the numerous fragments that might be generated by them are preserved forever in the geostationary region. To mitigate additional breakups and to remediate the precious GEO environment, therefore, measurement and origin identification of unknown OD are necessary to accurately define the current OD environment in the geostationary region.

There are two definitive breakups with regard to those occurred in the geostationary region and their fragments are in the public catalogs to date; the first breakup is an energetic explosion of the CIS Ekran 2 (International Designator (ID) of 1977-092A) on 23 June 1978 induced by battery malfunction, and the second breakup is also an energetic explosion of the US Titan 3C Transtage (ID of 1968-081E) on 21 February 1992 induced by ignition on remnant fuel (Johnson, 2001). These two confirmed breakups are not sufficient to account for the breakup fragments population discovered in the geostationary region, however. Some satellites and upper-stages in the geostationary region experienced orbital anomalies that might be associated with breakups as indicated by several researchers: e.g. Johnson (2001); Pensa *et al.* (1996); Rykhlova *et al.* (1997). There are also attempts to associate unidentified GEO debris population with breakups. For example, Krag (2002a,b) reported that fourteen breakup events in total might have been occurred in the geostationary region by analyzing the ESA's optical survey results. Oswald (2008) further analyzed more observation data and revised down the total event number from fourteen to twelve. These twelve breakup events consist of explosions of

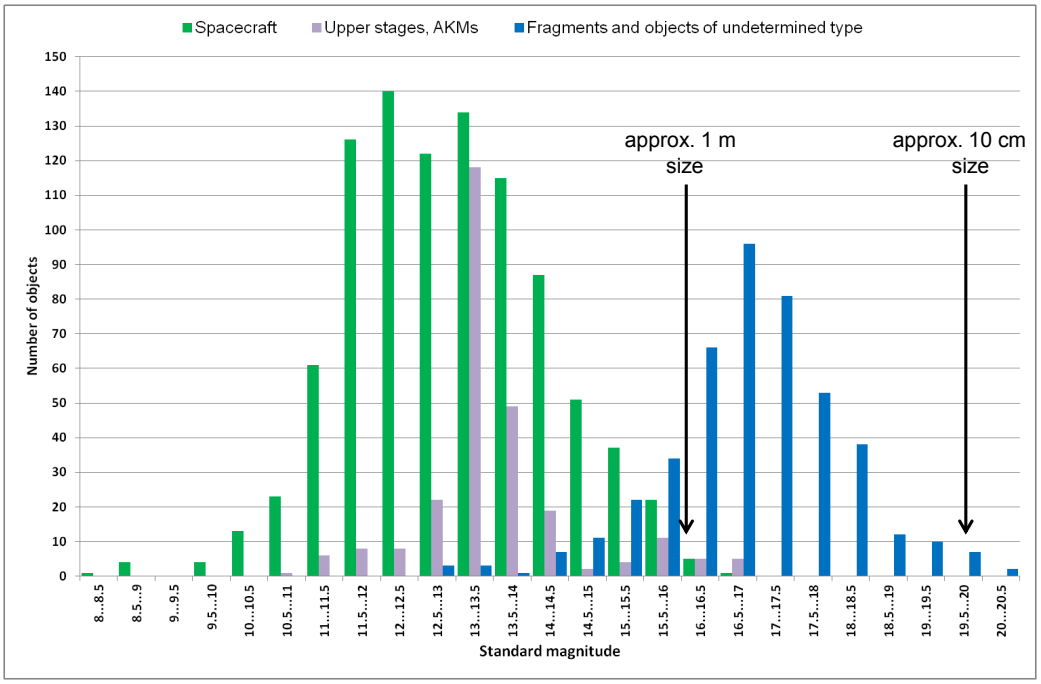


**Figure 1.1: ISON-tracked GEO objects distribution by standard magnitude. Each object is assumed as a Lambert sphere with albedo of 0.15. (Molotov *et al.*, 2012)**

six Titan 3C Transtages (1966-053J, 1967-066G, 1968-081E, 1973-040B, 1975-118C, 1979-053C), four communications satellites (1975-117A, 1977-092A, 1979-087A, 1988-018B) and two unidentified objects. However, uncertainties about relations between unidentified GEO debris, breakups, and orbital anomalies remain to be further investigated.

## 1.1 Research objective

This dissertation aims to establish an effective strategy to search breakup fragments in the geostationary region. The search strategy to be proposed will be effective by mainly two aspects. First, a comprehensive approach is introduced into the search strategy to verify each of the relations between unidentified GEO debris, breakups, and orbital anomalies by a simple and clear viewpoint. Realization of this viewpoint involves not only observations but also predictive analyses that characterize, track, and predict the behaviors of individual and groups of breakup fragments. This aspect will be addressed by applying OD modeling techniques, which mathematically describe debris generation and orbit propagation, into observation planning, de-

tection, origin identification, and characterization of breakup fragments. Second, the proposed strategy is very practical because it will be designed to work well with typical computers and relatively small aperture telescopes (whose diameter is smaller than 1 m) equipped with CCD camera, as will be demonstrated in each chapter. Compatibilities with conventional computers and observation systems are necessary to assess current space situations. Thus, outcomes of this research will contribute to define the current OD environment and to conduct reliable risk assessments for future space explorations.

## 1.2 Identification in orbital debris measurement

Identification, which distinguishes an object from others with regard to a state, is the essential action in OD measurement. Figure 1.2 classifies states of OD to be identified in the search strategy. Predictive analyses to be addressed in each chapter considers the difference of states to properly and effectively be combined with observations. The states can be classified into four types: signal, tracklet, orbit, and origin. What each state stands for in the search strategy can be explained as follows.

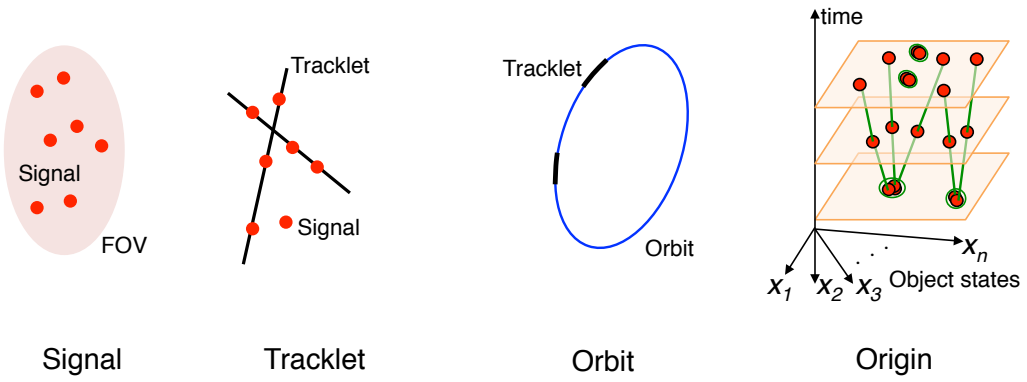


**Figure 1.2: States of orbital debris to be addressed in the dissertation.**

Signal denotes a figure of a space object that will be appeared in an image frame, i.e., a snapshot of a sensor's field-of-view (FOV) pictured by CCD camera. A signal consist of bright pixels distributed around the light center of the object. Object detection algorithms are required to distinguish signals from noise pixels and to measure properties of each signal such as brightness and angular positions in the image frame and in the sky.

Tracklet denotes a series of signals associated with one space object in image series. Object detection algorithms also perform tracklet identifications. A tracklet provides properties such as brightness variation, temporal length, position center, and angular velocity.

Once several pairs of tracklets are associated with one space object, its full trajectory around the Earth, i.e., orbit, can be estimated. This process is so-called orbit determination. Orbit provides further information of the space object than signals or tracklets. It enables to predict temporal position, past orbits, and future orbits of the space object by applying orbit propagation techniques.

Every OD is originated from a satellite or a rocket, thus, origin is identity of OD. Origin identification is the essential approach to associate measured states of OD, such as tracklets and orbits, with origin. Once origin of observed OD is identified, its outcome can be applied to verify each of the relations between unidentified GEO debris, breakups, and orbital anomalies. Ultimately, plentiful origin identification outcomes enable to conduct further environmental assessments, such as breakup event characterization, current environmental assessment, and its future projections.

## 1.3 Thesis overview

This dissertation consists of seven chapters. Figure 1.3 schematically describes relations between each chapter in the dissertation.

The first chapter introduces general backgrounds of this research, and past contributions to reveal current situations of the geostationary region. This chapter classifies issues to be addressed in the dissertation, and proposes the search strategy to solve the issues effectively.

The second chapter formulates the search strategy applicable for breakup fragments in the geostationary region, based on Hanada *et al.* (2013); Uetsuhara *et al.* (2012b). The breakup of 1968-081E is selected as a demonstration target of the search strategy. Actual observations are conducted at the JAXA Nyukasa Observatory (JNO). The predictive analyses of breakup fragments including population prediction and motion prediction, and basic principles of breakup fragments to be applied to the predictive analyses are introduced in this chapter. Predictive analyses results are applied to the observation planning of the 1968-081E fragments at JNO.

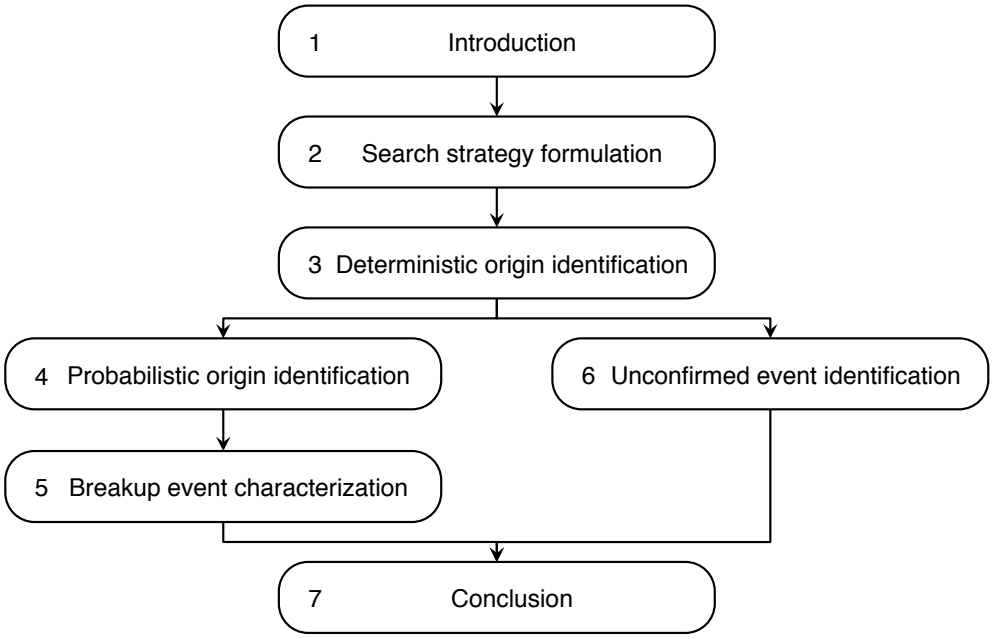


**Figure 1.3: Structure of the dissertation.**

Detection results acquired based on the observation plan are discussed focusing on comparisons of detection results of correlated targets (CTs) and uncorrelated targets (UCTs). Detection process in this chapter also addresses an effective identification of a tracklet with very weak signals in image series by a combination of the motion prediction and a track-before-detect (TBD) detection algorithm. This chapter finally verifies basic performances of origin identification process in the search strategy. In the origin identification process, UCTs will be associated with the breakup of 1968-081E at the observation epochs as a state of a tracklet determined by detection algorithms and also at the breakup epoch as a state of orbital elements determined by follow-up observations.

The third chapter further verifies capabilities of the origin identification as deterministic viewpoints, based on Uetsuhara *et al.* (2012a). Concept of the deterministic origin identification is to deterministically distinguish several breakup events at a same series of measurements. Two known breakups of 1968-081E and 1977-092A is selected as demonstration targets of this chapter. Actual observations are conducted at JNO. First, this chapter theoretically confirms whether or not one can distinguish between populations of the 1968-081E fragments and the 1977-092A fragments at a same observation period. Then, this chapter theoretically and empirically confirms whether or not one can distinguish between motion of tracklets of the

1968-081E fragments and the 1977-092A fragments at the same observation period. Finally, this chapter empirically confirms whether or not one can identify the right origin of orbits of objects detected through actual observations planned for the two selected breakup events.

The fourth chapter addresses a probabilistic origin identification of breakup fragments, based on Uetsuhara *et al.* (2013c). The probabilistic origin identification is a method to quantitatively associate origins of uncorrelated tracklets with possible breakup events. This chapter formulates the probabilistic origin identification method by applying a pattern recognition technique. The breakup of 1968-081E is selected as a main observation target for demonstration of the probabilistic origin identification. Actual observations are conducted as an observation campaign employing a 35-cm telescope located at JNO, a 50-cm telescope of the Taiwan-America Occultation Survey (TAOS) project located at the Lulin observatory in Taiwan, and the Lulin 1-m telescope (LOT) located at the same observatory as the TAOS. The observation plan for this campaign is optimized to detect 1968-081E fragments with a consideration of angular velocity characteristics on sensors. The proposed method is verified by evaluating origins of the tracklets detected at TAOS.

The fifth chapter addresses breakup event characterization, based on Uetsuhara & Hanada (2013a); Uetsuhara *et al.* (2013b). The breakup event characteristics to be assessed include fragmentation profile and breakup scale. The breakup of 1968-081E is selected as a demonstration target of this chapter. First, this chapter introduces a detailed approach to assess fragmentation profile of a breakup object by using orbital data of 1968-081E fragments catalogued by the SSN. Delta-velocity given to each fragment at breakup is evaluated to assess the fragmentation profile. Second, this chapter introduces a detailed approach to assess a scale of an explosion breakup by using the identified tracklets acquired and processed through the search strategy. Scaling factor, introduced in the NASA standard breakup model 2001 revision (Johnson *et al.*, 2001), is evaluated to assess the breakup scale. The probabilistic origin identification results, which are evaluated in the fourth chapter, are applied to demonstrate the breakup scale assessment. Finally, demonstration results are applied to discuss breakup fragments environment in the geostationary region.

The sixth chapter addresses identifications of an orbital anomaly as a breakup event, whose occurrence is unconfirmed by the observation of the moment, based on Uetsuhara & Hanada (2013b); Uetsuhara *et al.* (2013a). The orbital anomaly of 1967-066G is selected as a demonstration target of the identification method. Formulating a hypothesis involved in identifying

an orbital anomaly as a single breakup event, this chapter evaluates long-term behaviors of 1967-066G fragments generated based on the hypothesis to theoretically confirm whether or not one can identify an orbital anomaly as a breakup event by actual observations. To acquire orbital data of 1967-066G fragments candidates, actual observations are conducted at JNO. The deterministic origin identification methods established in the third chapter are applied to the acquired orbital data to verify the hypothesis formulated.

The seventh chapter concludes the dissertation with essential and novel outcomes discovered in the research. Through the theoretical and empirical confirmations from the second chapter to the sixth chapter, this dissertation finally establishes the effective search strategy that contributes to define current situation in the geostationary region.

# 2

# Search strategy formulation

This chapter proposes a strategy to search breakup fragments in the geostationary region by means of ground-based optical observations based upon predictive analyses. Breakup fragments have uncertainties in the states such as their position and motion, or even in their existence. This chapter introduces the predictive analyses, named population prediction and motion prediction, to resolve those uncertainties. Population prediction evaluates the time-averaged distribution of fragments, whose position at a given time is unknown, in the celestial sphere. Motion prediction evaluates the expected motion of fragments appeared in image series acquired by a telescope's CCD camera. This chapter logically describes procedures of the search strategy, and provides mathematical expressions of population prediction and motion prediction. This chapter also validates the search strategy via actual observations, in which a confirmed breakup of 1968-081E is selected as a target. The observations are conducted during the new moon term in December 2010. It will be concluded that the proposed strategy is valid even for searching uncatalogued breakup fragments in the geostationary region.

OD modeling techniques, which describe debris generation and orbit propagation, enable to predict fragments distribution in the celestial sphere, hereinafter called population, and their two-dimensional motion on a sensor, hereinafter called motion, during observations. The population prediction of fragments specifies effectively when, where, and how one should conduct optical measurements using ground-based telescopes, which is the most capable device for GEO environment resolution. On the other hand, the motion prediction of fragments specifies effectively and precisely how one should acquire and process image sequences of objects in GEO acquired using ground-based telescopes.

## 2. SEARCH STRATEGY FORMULATION

First of all, this chapter introduces overview of the search strategy to be proposed. The search strategy consists of the six procedures as follows: hypothesis formulation, population prediction, motion prediction, observation, detection, and origin identification. A workflow of the search strategy is schematically shown in Figure 2.1. Search target, each procedure, and outcome of each procedure are surround with a narrow green frame, a bold blue frame, and a narrow red frame, respectively. Input and output relations between each frame are indicated by arrows. Main tasks of each procedure are described in the following paragprahs.

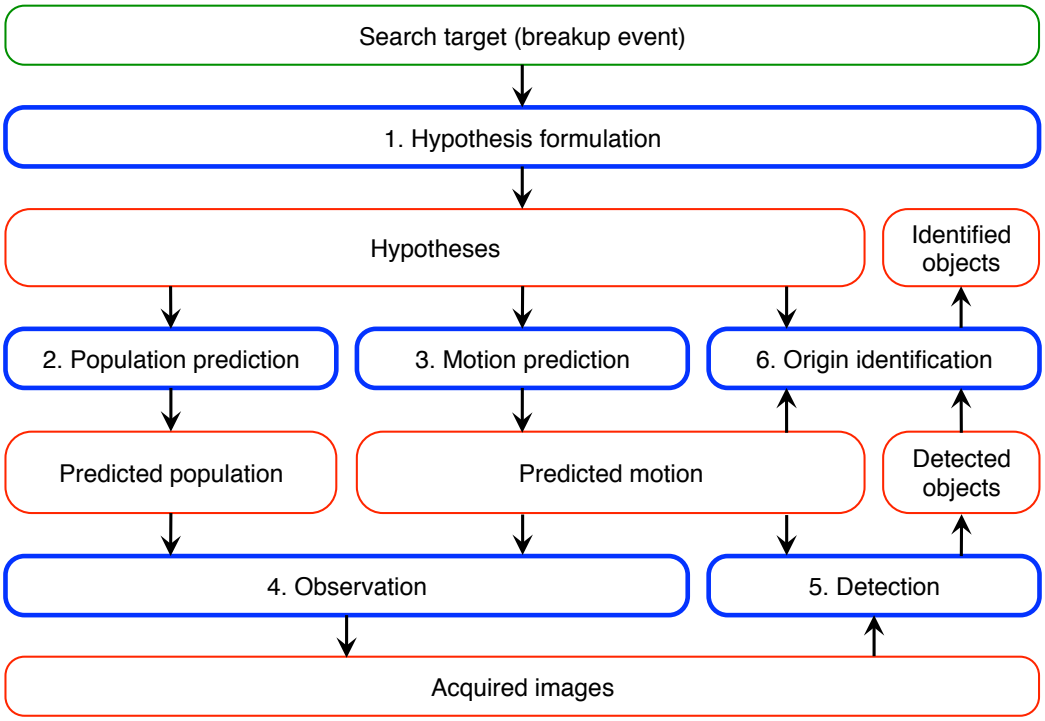


**Figure 2.1: Workflow of the search strategy.**

The first procedure "hypothesis formulation" formulates hypotheses involved in the search strategy to conduct predictive analyses of breakup fragments. The hypothesis formulation mainly consists of four actions as follows.

1. selection and characterization of a breakup event such as orbit of the parent body, breakup epoch, and breakup scale
2. selection of OD modeling techniques to be applied to estimate states of each fragment from the selected breakup conditions
3. characterization and location of observation sites

4. evaluation of orbital data of breakup fragments to be used in population prediction, motion prediction, and origin identification

The second procedure "population prediction" provides a probability that breakup fragments will be in a bin specified by the geocentric right ascension ($\alpha$) and declination ($\delta$) during observation periods. Size of a bin will be determined by a sensor's FOV to be employed.

The third procedure "motion prediction" provides a probability distribution of the motion vectors ($\boldsymbol{m}$) of breakup fragments that may be appeared in image sequences acquired at a planned observation coordinate. The predicted motion has a variety of applications as will be described so that one must carefully define temporal resolution and the motion vector's unit suited to each application.

The fourth procedure "observation" plans observations by referring predictive analyses results and conducts optical surveys for breakup fragments using telescopes based on the observation plan. One selects an observation coordinate indicating a higher probability in the predicted population, considering the telescope tracking sequence and the avoidances of saturation by other bright stars and blind directions by surrounding environments at a planned observation site. Observation period and imaging conditions are planned in this procedure, too. Finally, image sequences are acquired through the optical surveys conducted based on the observation plan.

The fifth procedure "detection" analyzes image sequences acquired at observations to detect fragments by image-processing algorithms. Once the temporal positions and motion vector of detected object is correlated with the known objects cataloged by the SSN, the debris is labeled as correlated target (CT). Otherwise labeled as uncorrelated target (UCT).

The final procedure "origin identification" identifies the origin of each UCT. This procedure uses the predicted motion and hypothesis orbits with a reverse propagation technique to correlate UCTs with a selected breakup. To conduct the reverse propagation, the orbit of a UCT must be determined by follow-up observations. Once the origin of the breakup that released UCTs is successfully identified, the origin identification results can be applied to characterize the selected breakup as will be demonstrated in Section 5.2.

## 2.1 Hypothesis formulation

This section addresses selection and characterization of a search target and selection of observation site to conduct actual observations. OD modeling techniques to evaluate orbits of breakup fragments of the search target are also introduced in this section.

### 2.1.1 Selected target

This study selects a confirmed breakup of the Titan 3C Transtage, whose ID is 1968-081E and the satellite catalog number (SC#) identified by the SSN is 3432, to demonstrate and validate the search strategy. Details of the breakup of 1968-081E was first reported by Pensa *et al.* (1996). The Maui GEODSS system accidentally observed 23 objects clustered within 0.5° of the nominal location of 1968-081E on 21 February 1992. They conducted intensive follow-up observations and analyses, and concluded that the clustered objects must be fragments of 1968-081E and the breakup epoch estimated was 09:31:12 UT on 21 February 1992. Here UT denotes the universal time. Eight fragments (1968-081 G, H, J, K, L, M, N, and P) are being tracked by the SSN to be catalogued as of March 2011, when the demonstration of this chapter was conducted. It should be noted that 1968-081G and H are identified as debris of the Transtage's payload Lincoln Experimental Satellite 6 (LES 6) in the COGO catalogue.

### 2.1.2 Observation site

To demonstrate the search strategy in this chapter, observations are conducted at JNO located at Mt. Nyukasa, Nagano Prefecture, Japan. A 2048 pixels × 2048 pixels CCD sensor mounted on 35cm aperture equatorial telescope is available at the observatory to search 1968-081E fragments. Table 2.1 provides the specification of the observatory and the sensor. This sensor in combination with commonly used image processing algorithms can detect objects with 17th magnitude. The FOV of 1.27° × 1.27° is feasible to capture GEO objects in a frame for about 5 minutes with fixed right ascension and declination observation.

### 2.1.3 OD modeling techniques

The OD modeling techniques to be applied for the hypothesis formulation are debris generation and orbit propagation. This section describes essential information of the OD modeling

**Table 2.1:** Specifications of JNO and the sensor

| Keyword | Parameter |
|---|---|
| Longitude | 138°10'18" east longitude |
| Latitude | 35°54'05" north latitude |
| Altitude | 1870 m |
| Lens tube type | Reflector telescope, $\epsilon$-350 (TAKAHASHI SEISAKUSHO Ltd.) |
| Focal length | 1,248 mm |
| Aperture | 350 mm (f/3.6) |
| Mount type | Fork-Type equatorial mount (SHOWA Industry Co., Ltd.) |
| CCD type | Back-illuminated CCD (N.I.L. Inc.) |
| Resolution | 2.23 "/pixel |
| FOV | $1.27^\circ \times 1.27^\circ$ |
| Readout time | 10 sec/frame |

techniques. The detailed theories of debris generation and orbit propagation algorithms are described in Appendix C and Appendix D, respectively.

First, debris fragments down to 10 cm in size are generated on the assumption made at the hypothesis formulation using the NASA standard breakup model 2001 revision (Johnson *et al.*, 2001). Debris generation has a significant uncertainty in nature so that it is unfeasible or impossible to compute an exact result with a deterministic algorithm. Therefore, a Monte Carlo (MC) method is applied to aggregate the results of the individual computations into the final result. 100 iterations or more are needed to get a statistically averaged result mainly derived from normalization distributions included in the NASA standard breakup model. Second, debris orbits are propagated till a planned observation epoch to evaluate the orbits of fragments of a selected breakup.

Perturbations to be considered for the orbit propagation are non-spherical part of the Earth gravity, solar radiation pressure (SRP) effects, and gravitational attractions due to the Sun and the Moon. This study applies general perturbation theories to evaluate each perturbations. SRP is a function of the area-to-mass ratio (A/m) so that larger SRP will act on a higher A/m object. Fragments will have higher A/m than large intact space objects so that inclusion of variation of A/m may have a significant impact on results of long-term propagation and thus may significantly change predictive analyses results of the targeted fragments. This study adopts the A/m probability density functions in the NASA model to assign an A/m to each of the breakup

fragments considered in the hypotheses formulation.

Table 2.2 summarizes breakup conditions applied to the search target 1968-081E. The breakup orbit is retrieved by propagating the two-line elements, which is available at the Space-Track catalog, to the estimated breakup epoch. This study assumes the scaling factor of explosion breakup as 1.0 for the NASA standard breakup model to generate fragments. The scale factor 1.0 means that the parent object totally fragmented with generating 238 fragments larger than 10 cm in size, and may be appropriate as the initial guess.

**Table 2.2:** Breakup conditions

| Keyword | Parameter |
|---|---|
| Semi-major axis | 41834.973 km |
| Eccentricity | 0.008 |
| Inclination | 11.909° |
| Right ascension of ascending node | 21.721° |
| Argument of perigee | 76.490° |
| Mean anomaly at breakup epoch | 31.803° |
| Breakup epoch | 21 February 1992 09:31:12 UT |
| Scaling factor | 1.0 |

## 2.2 Predictive analyses

This section introduces a pre-process step and basic principles of breakup fragments to be applied to the predictive analyses. The predictive analyses of breakup fragments including population prediction and motion prediction are formulated after introductions of the pre-process.

As schematically demonstrated in Figure 2.2, the pre-process divides a whole orbit of each fragment into small segments in terms of the geocentric right ascension ($\alpha$) and declination ($\delta$), and evaluates the effective number of each fragment at every segment. This effective number can be treated as time-averaged distribution of each fragment, whose position at a given time is unknown, at each segment. As will be discussed, the long-term orbit propagation between the breakup epoch and the observation epoch (approximately 18 years in this case) can appropriately simulate the gyroscopic precession in the geostationary region. True anomaly after long-term orbital evolution can be considered to be random, however.

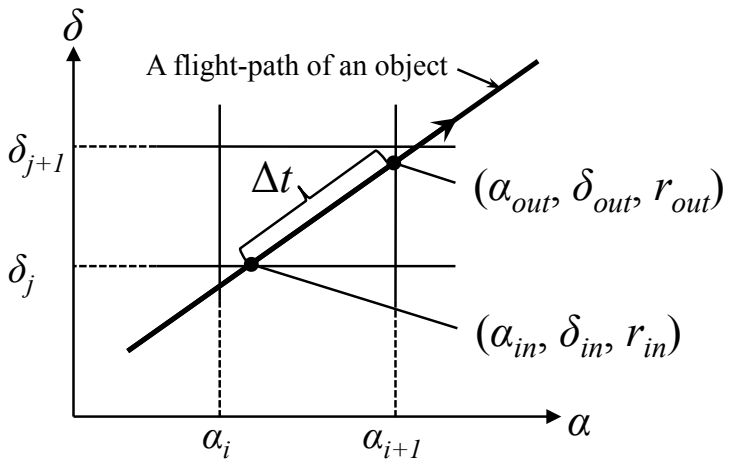


**Figure 2.2: Geometry of the pre-process.**

The states of each fragment in the bin ($\alpha_i$, $\delta_j$) include position vectors at the incoming time ($\alpha_{in}$, $\delta_{in}$, $r_{in}$) and the outgoing time ($\alpha_{out}$, $\delta_{out}$, $r_{out}$), a flight time ($\Delta t$) spent in the bin, and the effective number of the fragment ($n$) calculated by $\Delta t/T$, where $T$ is the orbital period of the fragment. Dimension of each bin can be set equal to the FOV of a selected ground-based sensor. The states of each fragment also include its satellite catalog number and cross-sectional area ($A$). The satellite catalog number specifies the parent object that released the fragment. The cross-sectional area will be applied to estimate brightness and size of the fragment. Table 2.3 shows an example of the pre-process data of several fragments at a bin of ($\alpha_i$, $\delta_j$) = (64°, 12°) with an assumption of the bin size = 1° × 1°.

**Table 2.3:** An example of the pre-process data

| SC# | $\alpha_{in}$[°] | $\alpha_{out}$[°] | $\delta_{in}$[°] | $\delta_{out}$[°] | $r_{in}$[km] | $r_{out}$[km] | $\Delta t$[sec] | $n$[-] | $A[m^2]$ |
|---|---|---|---|---|---|---|---|---|---|
| 3432 | 64.000 | 65.000 | 12.701 | 12.767 | 50446.188 | 50453.815 | 322.763 | 0.330 | 0.006 |
| 3432 | 64.000 | 64.028 | 12.998 | 13.000 | 49513.549 | 49515.018 | 8.647 | 0.009 | 0.007 |
| 3432 | 64.847 | 65.000 | 12.000 | 12.005 | 47018.956 | 47017.704 | 43.593 | 0.047 | 0.031 |

The pre-process data can be evaluated by the following calculations. Here one can define the position of the k-th fragment in its orbit as $u_k = f_k + \omega_k$ by applying Napier's rules between $u_k$, $\alpha_k - \Omega_k$, and $i_k$, where $f_k$ is the true anomaly at a given time, $\omega_k$ is the argument of perigee,

$\Omega_k$ is the right ascension of ascending node, and $i_k$ is the inclination.

$$u_k = f_k + \omega_k = \tan^{-1}\left[\frac{\tan(\alpha_k - \Omega_k)}{\cos i_k}\right] + \omega_k \tag{2.1}$$

One can get the time that the k-th fragment spends in a bin $\Delta t_k(\alpha_i, \delta_j)$ by the Kepler's equation using incoming true anomaly ($f_{in}$) and outgoing true anomaly ($f_{out}$). To determine the incoming and outgoing true anomalies of an object in a bin, one must judge whether flight path between $\alpha_i$ and $\alpha_{i+1}$ crosses two or more bins toward the declination direction. One can calculate the crossing coordinate ($\alpha_c$, $\delta_c$) using following equation, which can be obtained by Napier's rule between $\delta_c$, $i_k$, and $\alpha_c - \Omega_k$.

$$\delta_c = \tan^{-1}\left[\tan i_k \sin(\alpha_c - \Omega_k)\right] \tag{2.2}$$

The effective number is defined as the fractional time, per orbital period, which a fragment spends in a given bin. For the k-th object, therefore, the effective number is expressed by

$$p_k(\alpha_i, \delta_j) = \frac{\Delta t_k(\alpha_i, \delta_j)}{T_k} \tag{2.3}$$

where $p_k(\alpha_i, \delta_j)$ is the effective number of the k-th object at $(\alpha_i, \delta_j)$ bin, $\Delta t_k(\alpha_i, \delta_j)$ is a the flight time that of the k-th object spends in a bin given by $(\alpha_i, \delta_j)$, and $T_k$ is an the orbital period of the k-th object.

The pre-process proposed herein just discretizes the flight path onto the spherical grid without time step-size dependency of position calculation of an object. Thus, the pre-process approach is directly applicable to any orbits around the Earth.

### 2.2.1 Population prediction

The population prediction provides a probability that a fragment from a breakup will be in a bin specified by the geocentric right ascension ($\alpha$) and declination ($\delta$). Dimension of each bin can be set equal to the FOV of selected ground-based telescope's CCD sensor. The probability, $P_P(\alpha_i, \delta_j)$, is given by

$$P_P(\alpha_i, \delta_j) = \frac{1}{N_P} \sum_k p_k(\alpha_i, \delta_j) \tag{2.4}$$

where $N_P$ is the total number of fragments generated by MC runs.

Figure 2.3 predicts the population of 1968-081E fragments based on the pre-process data generated on the conditions defined in Table 2.2. It may be noted that the longitudinal axis is in the inverse order because one does not see the celestial sphere from the space, but the ground. As demonstrated in Figure 2.3, there are two regions indicating the highest probability density. The two regions correspond with the breakup point and its opposite phase in the orbit. Actually, approximately 80% of fragments pass through the two regions.

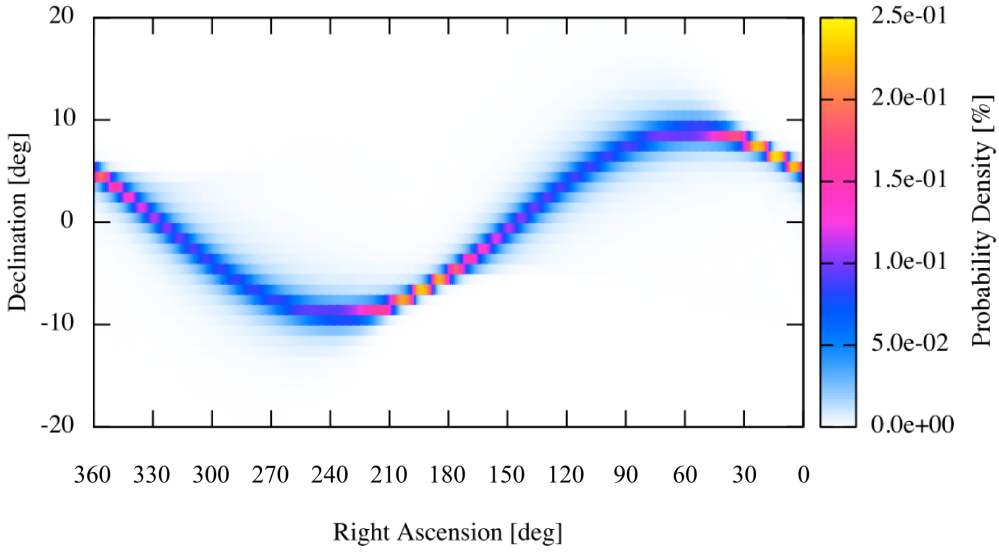


**Figure 2.3: Predicted population of 1968-081E fragments as of 5 December 2010 (Debris size 10cm, Bin size:** $1^\circ \times 1^\circ$**, 100 MC runs).**

### 2.2.2 Motion prediction

Apparent motion of fragments on the sensor plane is formulated in the motion prediction. To formulate the apparent motion, one has to project the orbital motions of fragments into the sensor plane so that the sensor's tracking mode during exposures should be assumed. Orbital period of objects in the geostationary region are nearly same as the Earth rotation period, one can see like they are fixed on the sky at any time. Thus, the CCD sensor should be fixed on the sky during exposures to get higher signal-to-noise ratio (S/N) of GEO fragments. The search strategy assumes that a telescope points in a definite direction with constant azimuth and elevation during exposures.

Considerations of curvatures of object's trajectories on the sensor plane make the motion prediction algorithm and detection algorithms complex. Usually, GEO objects seem to move linearly in a series of images taken within several minutes, if the telescope tracking is pointed to the fixed azimuth and elevation or the right ascension and declination. The search strategy assumes one observation period as several minutes, from 4 to 8 minutes depending on the sensor's FOV, the detection algorithm, and the tracking mode, to regard the two-dimensional motion as linear.

Motion prediction provides the probability ($P_M$) that the k-th fragment in an image sequence taken at the s-th observation has a two-dimensional motion vector specified by $m_k(s) = (\Delta X_k(s), \Delta Y_k(s))$. The two-dimensional motion vector is defined in the topocentric earth-fixed coordinate (TF) or in an image coordinate to be expressed in arcsec/sec unit or pixel/sec unit, respectively. To evaluate $P_M$, one must assume a fragment at a planned observation point can be captured any time except for the time when a telescope's tracking elevation angle becomes under 0°, because one cannot know the position of an unseen fragment at a given time. If the number of two-dimensional motion vectors ($m_k(s)$) at $(\Delta X_i, \Delta Y_j)$ bin is denoted as $p_s(\Delta X_i, \Delta Y_j)$, the probability, $P_M(\Delta X_i, \Delta Y_j)$, is obtained by

$$P_M(\Delta X_i, \Delta Y_j) = \frac{1}{N_M} \sum_s p_s(\Delta X_i, \Delta Y_j) \tag{2.5}$$

where $N_M$ is the product of the total number of fragments generated ($N_P$) and the number of observations planned. The motion vector ($\boldsymbol{m}$) can be calculated by the following coordinate and scale transformations. Here one assumes a typical observation method, where the CCD sensor is mounted on an equatorial telescope tracking at an azimuth-elevation coordinate while taking an image sequence. First, the position vector ($\boldsymbol{r}$) and velocity vector ($\boldsymbol{v}$) of an object at a bin in the geocentric inertial coordinate (GI) are calculated from the pre-process data given in Table2.3. Thus, $\boldsymbol{r}_{GI}$ and $\boldsymbol{v}_{GI}$ in the spherical coordinates are given by

$$\boldsymbol{r}_{GI} = \begin{pmatrix} r_{GI} \\ \alpha_{GI} \\ \delta_{GI} \end{pmatrix} = \frac{1}{2} \begin{pmatrix} r_{in} + r_{out} \\ \alpha_{in} + \alpha_{out} \\ \delta_{in} + \delta_{out} \end{pmatrix} \tag{2.6}$$

$$\boldsymbol{v}_{GI} = \begin{pmatrix} \dot{r}_{GI} \\ \dot{\alpha}_{GI} \\ \dot{\delta}_{GI} \end{pmatrix} = \frac{1}{\Delta t} \begin{pmatrix} r_{out} - r_{in} \\ \alpha_{out} - \alpha_{in} \\ \delta_{out} - \delta_{in} \end{pmatrix} \tag{2.7}$$

Once $\boldsymbol{r}_{GI}$ and $\boldsymbol{v}_{GI}$ are transformed from the spherical coordinate system to the rectangular coordinate system, those two vectors are transformed into TF by

$$\boldsymbol{r}_{TF} = {}^{GF}[R]_{GI}\boldsymbol{r}_{GI} - \boldsymbol{r}_{siteGF} \tag{2.8}$$

$$\boldsymbol{v}_{TF} = {}^{GF}[R]_{GI}\boldsymbol{r}_{GI} + \omega_{Earth} \times \boldsymbol{r}_{GI} \tag{2.9}$$

where ${}^{GF}[R]_{GI}$ is the transformation matrix from GI to the geocentric earth-fixed coordinate (GF), $\boldsymbol{r}_{siteGF}$ is the observer's position vector in GF, and $\omega_{Earth}$ is the rotation rate of the Earth. For near earth orbits such as GEO, a rotation matrix for earth axis, whose rotation angle is Greenwich mean sidereal time (GMST), is a good approximation for the transformation matrix ${}^{GF}[R]_{GI}$. One gets an angular velocity vector of the object in TF $(\dot{\alpha}_{TF}, \dot{\delta}_{TF})$ by the coordinate transformation from the rectangular coordinate system to the spherical coordinate system, and then $(\dot{\alpha}_{TF}, \dot{\delta}_{TF})$ is transformed into the image coordinate by multiplying a scale factor. The product of the temporal length of an image sequence, $L$, and the sensor resolution, $R$ in pixel/arcsec, gives the scale factor. One has to multiply -1, because the axial direction of image coordinate and the spherical coordinate seen from the ground is inverted. Thus, the motion vector can be expressed by several units as follows:

$$\boldsymbol{m} = \begin{pmatrix} \Delta X \\ \Delta Y \end{pmatrix} = -\begin{pmatrix} \dot{\alpha}_{TF} \\ \dot{\delta}_{TF} \end{pmatrix} \tag{2.10}$$

in the arcsec/sec unit, or

$$\boldsymbol{m} = \begin{pmatrix} \Delta X \\ \Delta Y \end{pmatrix} = -R\begin{pmatrix} \dot{\alpha}_{TF} \\ \dot{\delta}_{TF} \end{pmatrix} \tag{2.11}$$

in the pixel/sec unit, or

$$\boldsymbol{m} = \begin{pmatrix} \Delta X \\ \Delta Y \end{pmatrix} = -RL\begin{pmatrix} \dot{\alpha}_{TF} \\ \dot{\delta}_{TF} \end{pmatrix} \tag{2.12}$$

in the pixel unit.

To demonstrate the motion prediction, this section defines the conditions by referring the observatory's specifications in Table 2.1 and the observation point to be planned in Table 2.4. The sensor resolution factor ($R$) refers to the CCD's resolution specified in Table 2.1, and the temporal length of an image sequence ($L$) is measured as 7.0 minutes. The period of motion prediction is set as one-night observation period (4 December 2010 18:00-24:00 JST), which is also feasible to predict a motion of several nights around the defined period. Here JST denotes

the Japan standard time, which is 9 hours ahead of UT. Figure 2.4 shows the predicted motion of 1968-081E fragments in the pixel unit evaluated by Eq.(2.12). The color gradient in Figure 2.4 represents the probability density of the motion vector of 1968-081E fragments in each bin.

As Figure 2.4 demonstrates a remarkable feature of the motion prediction, fragments from a breakup forms a uniform and clear distribution at a fixed observation coordinate. In addition, the predicted motion has a peak region in its single distribution. The reason why those remarkable features appear can be concluded by the two facts; the first one is that the orbital plane elements (i.e. $i$ and $\Omega$) of fragments from a breakup, which are the functions of $\boldsymbol{m}$, distribute in a group (see also Figure 2.9 for the orbital plane vector distribution of fragments as of 6 December 2010), and the second one is that the around 80% of the fragments will be in the peak bin specified by $(\alpha_i, \delta_j)$ as discussed in Section 2.2.1.

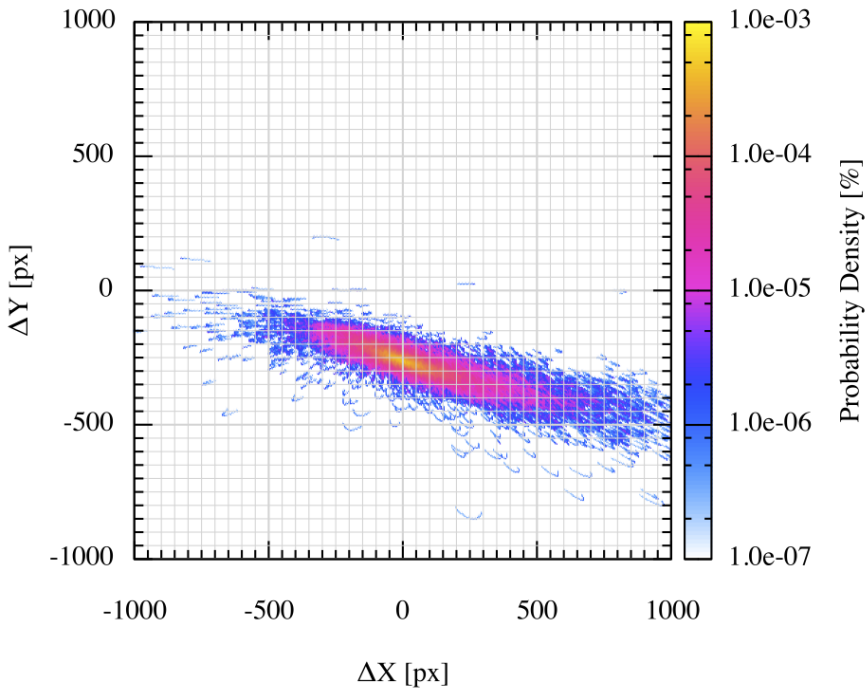


**Figure 2.4: Predicted motion of 1968-081E fragments as of 5 December 2010 (Debris size 10cm, Bin size:** $1^\circ \times 1^\circ$**, 100 MC runs, Bin size: 5pixel×5pixel).**

Those features indicate that one may be able to identify the origin of detected UCT without further investigation such as backward propagation of its orbit, if the motion vector $\boldsymbol{m}$ of an UCT appears in a uniform and clear distribution, especially at a higher probability density bin in Figure 2.4. In Section 2.5, it will be proved that one can conduct such quick-look origin identification using predicted motion of fragments from a target breakup.

The predicted motion also may be able to utilized to detect small fragments. Observation planning in combination with predicted motion evaluated in arcsec/sec unit or pixel/sec unit (Eqs.(2.10) & (2.11)) can gain better S/N for detected objects by comparing the statistics such as mean, variance, and covariance of predicted motions at several observation coordinates. The smaller mean, variance, and covariance make the magnitude of $\boldsymbol{m}$ smaller to gain better S/N. This observation planning technique will be introduced in Section 4.2.3. Moreover, motion prediction can enhance the detection process, as will be demonstrated in Section 2.4. Usually, huge computational time is required for detection algorithms that are designed to detect faint objects, almost buried under background noise level of image sequences. The predicted motion evaluated in pixel unit (Eq.(2.12)) can specify the shifting pixel values of such objects in image sequences so that it provides constraints to the faint objects detection algorithms to reduce computational time.

## 2.3 Observation

This section addresses the observation planning of 1968-081E fragments at JNO. As mentioned in Section 2.2.1, one of remarkable features of population prediction is that one can specify effective observation coordinate to search fragments in terms of geocentric right ascension and declination. Therefore, a telescope should be oriented at a fixed geocentric coordinate specified by the population prediction. For the new moon term in December 2010, the most suitable observation coordinate is $(\alpha, \delta) = (24.5°, 7.5°)$, which corresponds with the peak region on the right side in Figure 2.3. One also has to define the geocentric radius ($r$) to track by a sensor on the ground besides the geocentric right ascension and declination. Figure 2.5 shows the geocentric radius distribution of 1968-081E fragments in the FOV of the planned observation coordinate. This demonstration selects 42700 km as the tracking radius, which corresponds with the mean value of the distribution in Figure 2.5. Almost all fragments distribute around the selected geocentric radius. The 1000-km difference in radius between the 1968-081E fragments

makes little change in the velocity of GEO objects to be ignored. This fact enables us to get a similar magnitude of $\boldsymbol{m}$ for those fragments at the observation coordinate, and one can get suitable S/N for almost all fragments. The selected observation coordinate is summarized in Table 2.4.

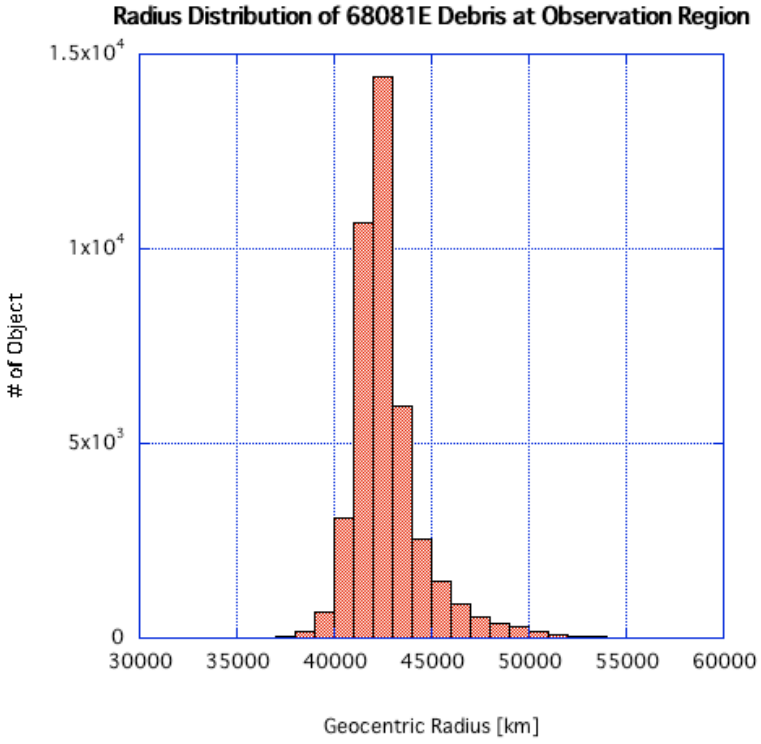


**Figure 2.5: Geocentric radius distribution of 1968-081E fragments at observation FOV (Bin size: 1000 km).** - The latitudinal axis shows the cumulative number of objects from 100 MC runs in the FOV.

**Table 2.4:** Selected observation coordinate

| Start epoch (JST) | End epoch (JST) | $\alpha$ [°] | $\delta$ [°] | $r$ [km] |
|---|---|---|---|---|
| 18:00:00 | 24:00:00 | 24.5 | 7.5 | 42700.0 |

As discussed in the Section 2.2.2, the fixed azimuth-elevation tracking is preferred during exposures to get a higher S/N of GEO objects, however. During the fixed azimuth-elevation tracking, the FOV drifts from the planned geocentric coordinate due to the Earth rotation. Therefore the telescope's tracking direction should switch between the fixed azimuth-elevation and the fixed geocentric coordinate at every observation to search and detect target fragments

as many as possible. This tracking sequence is illustrated in Figure 2.6. A sensor points a fixed azimuth and elevation while taking an image sequences, which consists of 32 images taken by 3 seconds exposure. Because of the readout time of the CCD sensor, tracking direction specified as a function of azimuth and elevation moves every 8 minutes as illustrated in Figure 2.6.

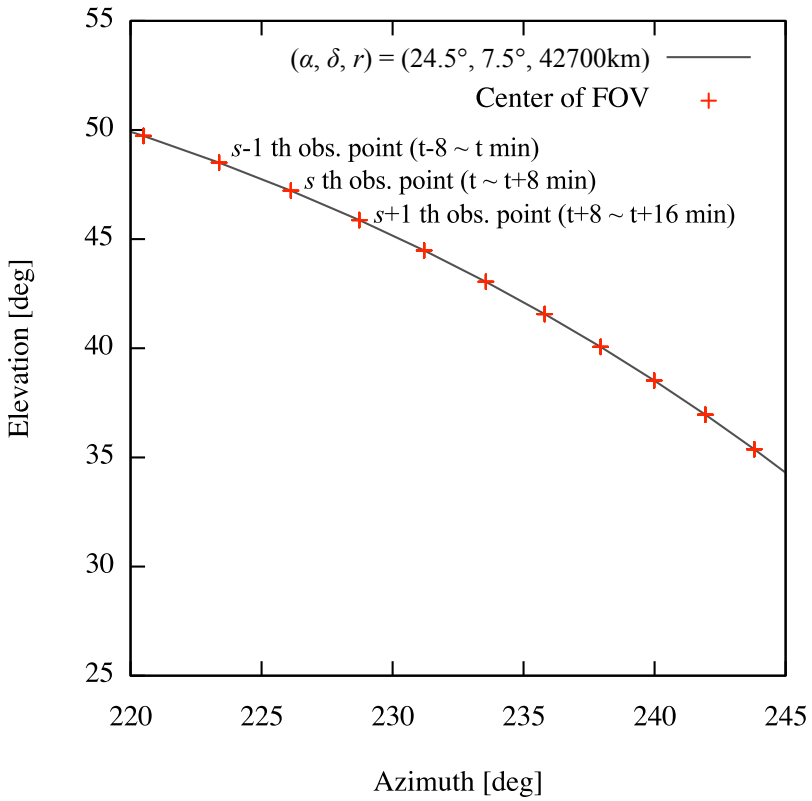


**Figure 2.6: Tracking sequence for 1968-081E fragments.** - In the figure, *t* denotes the time epoch imaging the first frame at s-th observation point.

## 2.4 Detection

Based on the observation plan, 90 sets of image sequence (each consists of 32 frames) were acquired during 2-night observations of December 4th and 5th of 2010. To analyze acquired images, the line identifying technique developed by Yanagisawa *et al.* (2009) is used to detect debris. The line identifying technique detects candidate OD in an image frame using a brightness threshold and a shape parameter, and then finds any series of candidate OD that are arrayed on a straight line from the first frame to the last frame.

The detection result of 90 sets of image sequences by the line identifying technique is shown in Figure 2.7 and Table 2.5. In total, 18 CTs and 10 UCTs have been detected. The required process time for 1-night observation images (45 sets of image sequences) is approximately 5 hours using 4 PCs, each of which consists of Intel(R) Core 2 Duo processor E8400 3GHz and 4GB DDR2-SDRAM memory, so that one can complete a detection analysis of 1-night data before the next night observation starts. The tendency of the distribution in Figure 2.7, where UCTs have fainter magnitude than CTs, indicates that UCTs may be fragmentation debris. The remarkable result shown in Table 2.5 is that some cataloged fragments originated from 1968-081E are detected (J and K). This result proves the validation of population prediction because the fragmentation debris from the target breakup have successfully detected via the observations based on the predicted population (appeared in Figure 2.3).

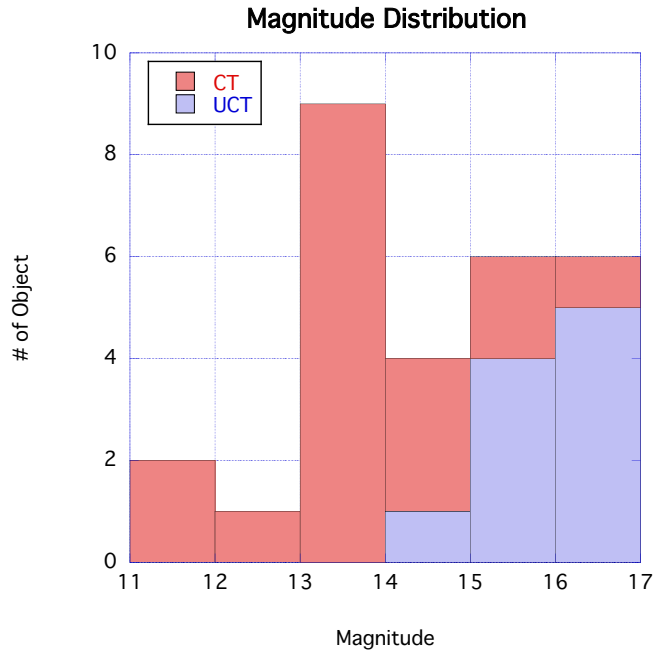


**Figure 2.7: Magnitude distribution of objects detected by the line identifying technique during 4-5 December 2010.**

Faint objects detection in combination with the predicted motion is also demonstrated in this section. Detection methods for moving celestial objects can be two folds: 1) Detect-Before-Track (DBT), and 2) Track-Before-Detect (TBD) (Gural *et al.*, 2005). DBT methods detect features in each image frame first, and then track individual features to estimate their trajectory. The S/N detectable with DBT methods is reasonably high so as individual features

**Table 2.5:** Detection summary by the line identifying technique during 4-5 December 2010

| Date | ID | $\Delta X$ [pixel] | $\Delta Y$ [pixel] | Magnitude |
|---|---|---|---|---|
| 4 December 2010 | 1968-081K | -85 | -248 | 13.24 |
| | 1975-091B | 969 | -1,078 | 11.58 |
| | 1976-101A | 167 | -583 | 14.08 |
| | 1982-020A | 81 | -698 | 13.40 |
| | 1982-031A | 46 | -675 | 14.15 |
| | 2003-043B | 1,402 | 40 | 13.26 |
| | 2003-043D | 1408 | 17 | 13.99 |
| | UCT1 | -56 | -721 | 16.09 |
| | UCT2 | 309 | -366 | 15.71 |
| | UCT3 | -117 | -686 | 15.73 |
| | UCT4 | 124 | -270 | 16.07 |
| | UCT5 | -244 | -602 | 15.75 |
| 5 December 2010 | 1968-081J | 21 | -259 | 15.02 |
| | 1968-081K | -85 | -252 | 13.27 |
| | 1974-075A | 56 | -668 | 15.91 |
| | 1976-101A | 167 | -586 | 14.17 |
| | 1979-038A | 103 | -704 | 11.72 |
| | 1981-061A | 38 | -644 | 12.66 |
| | 1981-061F | -56 | -714 | 16.67 |
| | 1981-069F | 106 | -721 | 13.15 |
| | 1982-020A | 92 | -736 | 13.37 |
| | 2003-043B | 1,425 | 21 | 13.10 |
| | 2003-043D | 1,430 | 11 | 13.59 |
| | UCT6 | -280 | -241 | 16.18 |
| | UCT7 | -174 | -512 | 16.24 |
| | UCT8 | -46 | -199 | 15.11 |
| | UCT9 | 85 | -238 | 14.01 |
| | UCT6 | -280 | -241 | 16.18 |
| | UCT10 | 124 | -270 | 16.11 |

are recognizable by naked eyes. The line identifying technique also adopts the DBT algorithm. On the other hand, TBD methods assume appropriate hypothetical trajectories in a sequence of images first, and then stack each image by shifting along the hypothesized trajectories to emphasize moving faint objects. Therefore, the S/N detectable with TBD is relatively low in comparison to DBT, and can reach down to 1.0 theoretically and ideally. Since large telescopes can observe faint debris with sufficient S/N a combination of large telescopes and DBT methods have been believed as the most effective solution. A combination of small telescopes and TBD methods also could be an effective solution to detect faint debris. A problem here is that TBD methods may require longer computational time to detect moving faint objects than DBT methods. However, computational time can be reduced effectively and drastically if appropriate hypothetical trajectories are provided. The stacking method developed by Yanagisawa *et al.* (2005) is a unique TBD method that is designed to detect faint asteroids and OD. Stacking method can detect faint objects by stacking a series of images that have been shifted according to the assumed motion of target objects. In order to detect invisible moving object, various shift values of target objects must be investigated, which causes high computational workload without proper information of target objects, i.e, the predicted motion.

This study applies the stacking method to demonstrate faint OD detections effectively in combination with motion prediction, for the first time. The stacking method requires shift values to be tried as rectangle areas in the motion plane. This study applies the predicted motion (in Figure 2.4) to define the rectangle areas. To search several regions in parallel, three rectangles are defined in Table 2.6 to cover the boundaries of the predicted motion. A desktop PC, which consists of Intel(R) Core i7 870 2.93GHz and 8GB DDR3-SDRAM, is used to process same sets of image sequences analyzed by the line-identifying technique. The rectangle areas specified in Table. 2.6 are investigated by parallel processing. As a result of detection trials, one faint UCT that is not detected by the line-identifying technique is found from an image sequence taken at 5th December 2010. Motion of this faint object is $\boldsymbol{m}$ = (−123pixel, −205pixel) inside the rectangle area 1, and brightness is 17.3 magnitude. Approximately 3 hours are taken for each image sequence to finish the investigations of all rectangle areas, which equal to process 1-night observation data by 6 days, in a case of this demonstration. This processing time seems quite long, though process would never end in presumable periods if one did not apply the motion constraints to the stacking method. Thus, it is confirmed that the stacking method is capable of detecting faint OD by applying the motion prediction. It can be concluded that

offline process is suited for the stacking method without any hardware or software improvements. It may be noted that a stacking method improved by the Field Gate Programmable Array (FPGA) hardware technique is applied later in Section 4.3.1.

**Table 2.6:** Rectangle areas in the motion plane searched by the stacking method.

| Rectangle # | Min. $\Delta X$ [pixel] | Max. $\Delta X$ [pixel] | Min. $\Delta Y$ [pixel] | Max. $\Delta Y$ [pixel] |
|---|---|---|---|---|
| 1 | -150 | -50 | -300 | -150 |
| 2 | -49 | 50 | -325 | -175 |
| 3 | 51 | 150 | -350 | -200 |

## 2.5 Origin identification

This section verifies the aforementioned quick-look origin identification theory by comparing the measured motion vector $\boldsymbol{m}$ as shown in Table 2.5 with the predicted motion as shown in Figure 2.4. And finally, this section validates the feasibility of the proposed search strategy by addressing the origin identification of the detected UCTs using backward propagation techniques.

First, Figure 2.8 compares the motion of 1968-081E fragments predicted in Figure 2.4 with the motion of detected objects summarized in Table 2.5. The remarkable features here are that the measured motion vectors of 1968-081J and K are inside the higher probability density region, besides the measured motion vector of other CTs not from 1968-081E (e.g. 1981-061A) are completely outside the region of the predicted motion. The UCTs have the similar tendency in Figure 2.8. In total, 4 UCTs (UCT4, 8, 9, and 10) are plotted near 1968-081J and K. Those results indicate that the UCTs inside the aforementioned higher probability density region may originate from 1968-081E.

Second, the orbit determination of the UCTs are conducted by follow-up observation of the UCTs to assess the precise origin identification of the UCTs by backward propagation of their orbits to the breakup epoch of 1968-081E. This study applies the follow-up observation method developed by Yanagisawa & Umehara (2009), which defines a pear object from 2-night observation data and estimates the orbital elements of the defined pear object by the follow-up observation at the 3rd night. The detection result from 2-night observations as shown in Figure 2.8 provides one pear UCT (4 and 10), and the UCT has been successfully tracked at the 3rd

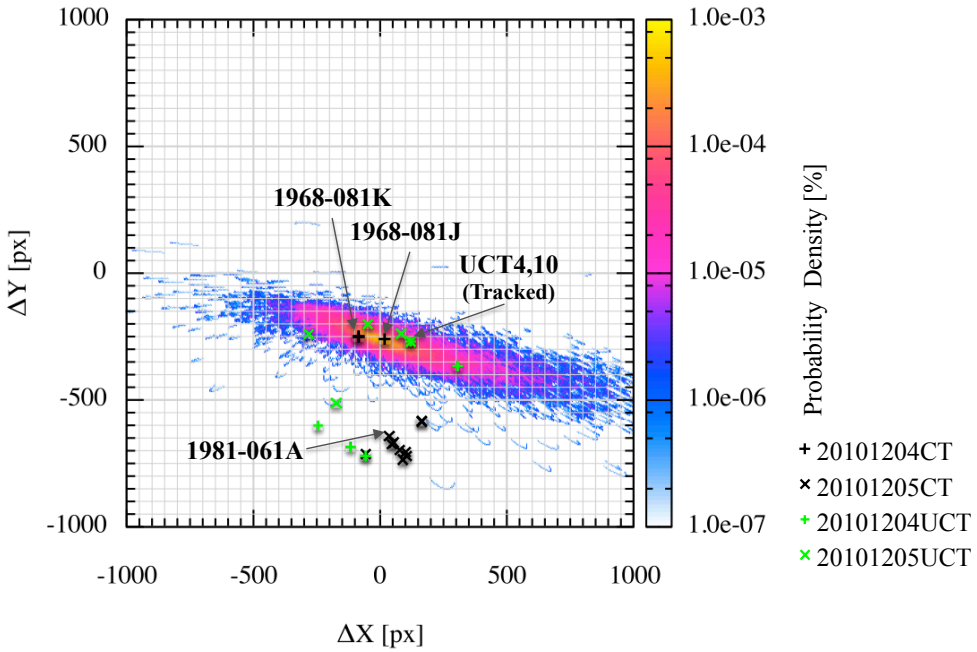


**Figure 2.8: The comparison result of the predicted motion of 1968-081E fragments and the measured motion vectors.**

night. The orbital transition of GEO fragments has a remarkable feature in $i\cos(\Omega) - i\sin(\Omega)$ coordinate system, which can identify whether the fragments are generated by breakups or not (Hanada & Matney, 2002; Hanada & Yasaka, 2005; Ikeda *et al.*, 2008). The $(i\cos(\Omega), i\sin(\Omega))$ coordinate system represents the orbital plane vector, and GEO objects shows clockwise transition in the coordinate system due to perturbation effects from the non-spherical part of the Earth gravity (e.g. $J_2$ term) and the gravitational attractions due to the Sun and the Moon. This backward propagation study adopts special perturbation theories including perturbation forces by non-spherical part of the Earth gravity (by applying EGM96 to the 8th order), third bodies (the Sun and the Moon), and SRP. A/m of 0.01 $m^2$/kg is assumed for the tracked UCT. Figure 2.9 compares the evolutionary history of the backward propagation data of the tracked UCT and the 1968-081E fragments at the breakup epoch (21 February 1992 09:31:12 GMT) in $i\cos(\Omega) - i\sin(\Omega)$ coordinate system. The fragments forms a linear distribution right after the breakup, as plotted by "+" in red in Figure 2.9. The blue plots show the orbital evolution of 1968-081E which is retrieved from the Space-Track catalog, from the observation epoch to the close breakup epoch. The cyan plots show the backward orbital evolution of the tracked UCTs. Those two orbital evolutions have a similar tendency and the distribution feature of red,

blue, and cyan plots at the breakup epoch is well correlated. What is more, an orbital evolution of the debris not from the 1968-081E breakup (e.g. 1981-061A) shows a different tendency from the others, and the plot of 1981-061A at the breakup epoch of 1968-081E shows different distribution feature from 1968-081E and the tracked UCT at the same epoch. Those evidences can conclude that the tracked UCT originates from 1968-081E.

Consequently, the proposed search strategy is validated by the origin identification result of the tracked UCT. Also, the aforementioned quick-look origin identification using the predicted motion is validated. As one of the application ways of the quick-look origin identification, one can conduct probabilistic origin identification of tracklets as will be described in Section 4.3.

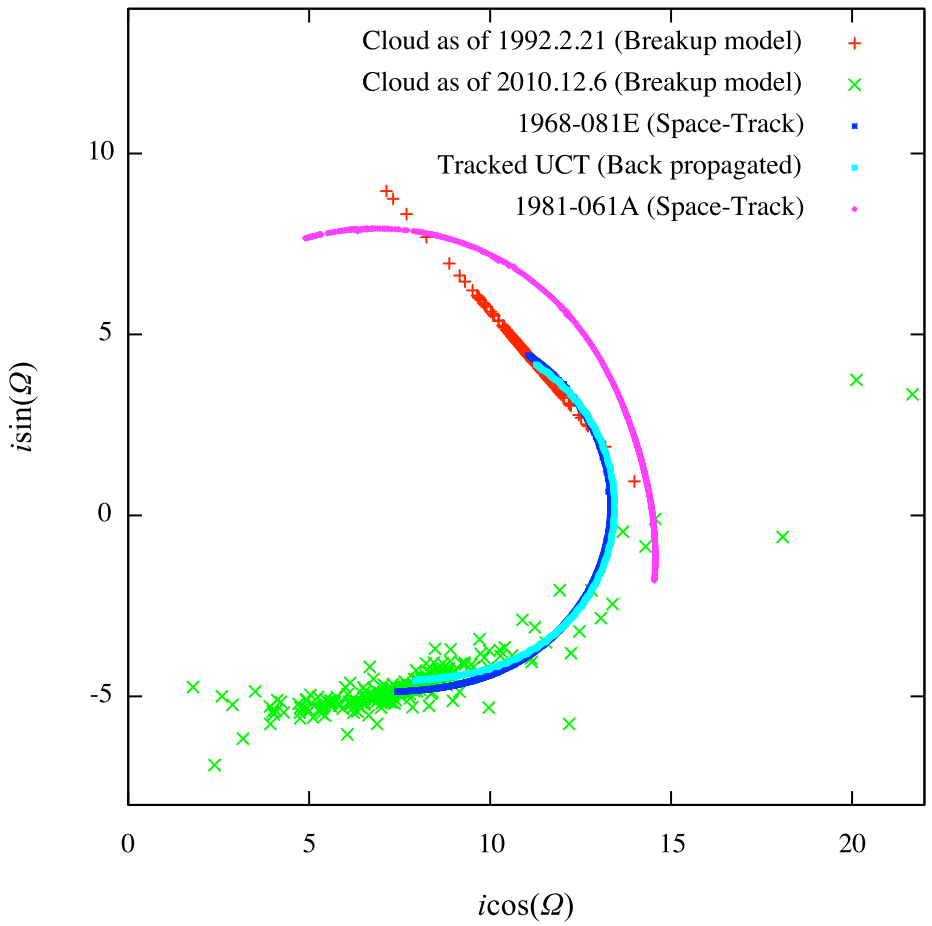


**Figure 2.9: Orbital plane vector distribution of 1968-081E fragments** - Red points represents the predicted 1968-081E fragments at breakup epoch, and Green ones at observation epoch. Transition histories of 1968-081E (Blue), the tracked UCT (Cyan), and not 1968-081E debris 1981-061A (Pink) between the observation epoch and the breakup epoch are also plotted. The time stamps of the transition plots (Blue, Pink, and Cyan) become older counterclockwise.

## 2.6 Summary

This chapter validated the proposed search strategy by selecting actual breakup event of 1968-081E as the search target. The population prediction specified when, where, and how to conduct observations. The observation result verified that there is a high correlation between measured and predicted two-dimensional motion of fragments in image sequences. This evidence enabled to utilize the motion prediction as a tool for various aspects of the search strategy such as observation planning, detection, and origin identification.

The proposed strategy detected 2 correlated fragments of 1968-081E and 4 suspicious UCTs that may originate from 1968-081E, which are inferred from the quick-look origin identification theory. What was more, the faint UCT undetected in a single image frame was detected by the stacking method inside the predicted motion of 1968-081E fragments. The proposed strategy also identified that one UCT (not cataloged object) originated from 1968-081E by the comparison of predicted orbital plane vectors and measured ones. It took only three nights observations to identify the origin of target fragments. In conclusion, it was validated that the search strategy was capable of searching uncataloged fragments in the geostationary region.

# 3

# Deterministic origin identification

Identifying breakups in observations is an essential measure to define and understand current OD situations. This chapter proposes and verifies a deterministic origin identification method applicable to multiple breakup events occurred in the geostationary region. The method aims to effectively detect and identify the breakup fragments by means of optical measurements. The predictive analyses and origin identification techniques demonstrated in Chapter 2 are applied to conduct the deterministic origin identification, and then the proposed method is verified by both theoretical and empirical approaches. The two definitive breakup events of 1977-092A and 1968-081E are selected for verifications of this study. It will be concluded that the proposed method can identify a right origin of each detected object in a single series of observations.

This chapter aims to deterministically identify the features of target breakups from the view points of population, tracklet, and orbit. When one targets two breakups in a single survey, the population prediction enables to specify an observation coordinate to search one breakup, and also an observation coordinate to search both breakups. In both cases, it is necessary to identify a right origin of each detected object by utilizing motion and orbital plane features of breakups. This chapter theoretically and empirically confirms that one can distinguish the tracklet motions of the two breakups at observations. After the verification of origin identification of tracklets using the motion feature, this chapter empirically confirms one can distinguish orbital plane features of the objects that are detected in follow-up observations and might be associated with one of the breakups.

## 3.1 Population identification

This section theoretically demonstrates the observation planning to identify two breakup events by applying the population prediction. In optical surveys of fragments of multiple breakup events, one can classify identification targets by two approaches:

I. A single breakup event in a set of observations to be identified
II. Multiple breakup events ($x$) in a set of observations to be simultaneously identified

Assuming there are $n$ breakup events to be considered as search targets, the approach I requires $n$-sets of observations for $n$-targets at least, whereas the approach II can decrease necessary sets of observations to $n/x$. In the approach I, the presence of fragments of untargeted breakups will be ignorable so that a right origin of each detected object can be distinguished uniquely. The approach II will be effective than the approach I in terms of the detection rate of fragments of targeted breakups, but requires to distinguish features of targeted breakups to identify a right origin of each detected object. This study assumes $x = 2$ and $n = 2$, which is an essential condition for deterministic origin identification of multiple breakup events, and confirms whether or not observation planning based on each approach is possible regarding an observation point selection and the origin identification of objects to be detected.

The observation point selection utilizes the population prediction of target fragments. The population in this study is evaluated as a time-averaged distribution of breakup fragments in the celestial sphere as is introduced in Section 2.2.1. The time-averaged distribution is suitable for qualitatively evaluating presence of the breakup fragments of 1968-081E and 1977-092A in the celestial sphere, because a long-term propagation of them results in feasible predictions for the orbital elements except for the temporal position.

The pseudo observation epoch is set to be 6th March 2011, when this theoretical confirmation is conducted. For theoretical and empirical confirmations of this study, the definitive breakups of 1977-092A and 1968-081E are selected as the search targets. As of March 2011, 8 breakup fragments (1968-081G, H, J, K, L, M, N, and P) of 1968-081E and 4 breakup fragments (1977-092H, J, K, and L) of 1977-092A are in the SSN catalogue, respectively. The breakup fragments of 1977-092A and 1968-081E are propagated till the observation epoch after the OD generation process at each breakup epoch. The OD generation applies the NASA breakup model 2001 revision (Johnson *et al.*, 2001) to generate fragments larger than 10cm.

The orbit propagation applies the general perturbation techniques including the $J_2$ effect, the lunisolar third-body effect, and SRP. The breakup conditions of 1977-092A to be applied to this study is summarized in Table 3.1, whereas those of 1968-081E are already summarized in Table 2.2.

**Table 3.1:** Breakup conditions of 1977-092A

| Keyword | Parameter |
|---|---|
| Semi-major axis | 42165.781 km |
| Eccentricity | 0.001 |
| Inclination | 0.172 deg |
| Right ascension of ascending node | 70.868 deg |
| Argument of perigee | 54.384 deg |
| Mean anomaly at breakup epoch | 244.847 deg |
| Breakup epoch | 23 June 1978 00:00:00 UT |
| Scaling factor | 1.0 |

Figure 3.1 shows the predicted populations of the fragments. The horizontal axis shows the geocentric right ascension ($\alpha$) and the vertical axis shows the geocentric declination ($\delta$). The bin size of predicted population is defined as 1° by 1°, which is a proper scale to consider a typical optical sensor's FOV adopted in this study. The gray-scale shows the time-averaged number of fragments at a given coordinate. At dense regions, one can observe the debris with higher probability than the light regions. There are two specific distribution groups in Figure 3.1. The distribution with larger amplitude corresponds to the 1977-092A fragments, and another distribution corresponds to the 1968-081E fragments. There are two dense regions in near $\alpha = 0°$ and $\alpha = 180°$. The overlap of each fragment path results in forming those dense regions. The both populations cross at the most dense coordinate, where one can observe the fragments originating in 1977-092A or 1968-081E with the highest probability. But in such region, one has to identify a right origin of a detected object from 1977-092A or 1968-081E. Thus, this region will be applicable to the approach II. As shown in Figure 3.1, on the other hand, it is also obvious that one can also select the observation coordinate where the population of one breakup is dominant, which will be applicable to the approach I. This study defines an observation coordinate suitable for the approach I as "Coordinate I", and that for the approach II as "Coordinate II".

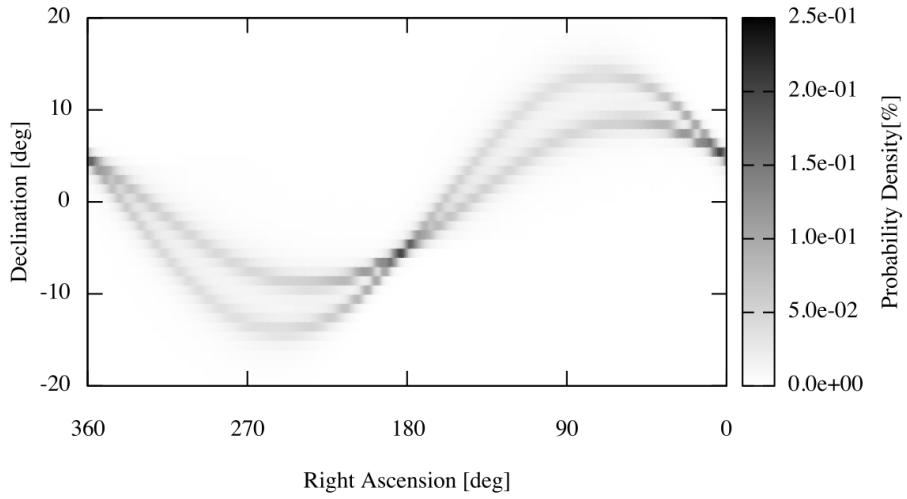


**Figure 3.1: Predicted populations of 1968-081E and 1977-092A fragments as of 6th March 2011 (100 MC runs, debris size ≥ 10 cm).**

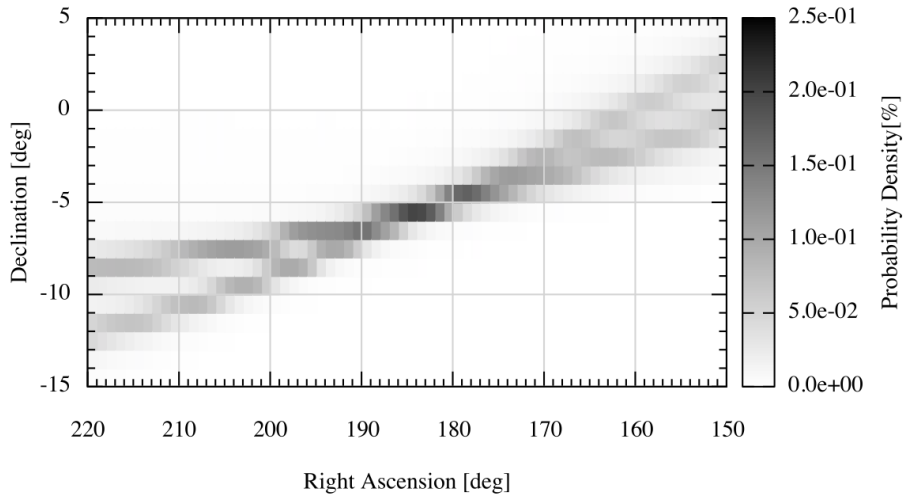


**Figure 3.2: Predicted populations of 1968-081E and 1977-092A fragments as of 6th March 2011 (Extracted from the Figure 3.1 around the observable region at JNO).**

To conduct theoretical and empirical confirmations of the approach I and II, one has to select the specific observation coordinates. As specified in Figure 3.2, the dense region around $\alpha = 180°$ is observable during a night at JNO in the observation epoch (6th March 2011). Table 3.2 specifies the observation coordinates chosen from Figure 3.2. In Table 3.2, the fraction of fragments population indicates the number of paths of each breakup fragments at each population prediction bin. The coordinate I, where the center of a bin ($\alpha$, $\delta$) is (195.5°, -6.5°), has dominant population of 1968-081E fragments by 93% ratio between both populations. On the other hand, the coordinate II, where the center of a bin ($\alpha$, $\delta$) is (184.5°, -5.5°), has nearly 1:1 population ratio.

**Table 3.2:** Specification of observation coordinates

| Coordinate name | $\alpha$ [°] | $\delta$ [°] | Percentage of population (1968-081E fragments) | Percentage of population (1977-092A fragments) |
|---|---|---|---|---|
| Coordinate I | 195.5 | -6.5 | 93 | 7 |
| Coordinate II | 184.5 | -5.5 | 55 | 45 |

## 3.2 Tracklet identification

This section theoretically and empirically confirms whether or not one can distinguish between motion of tracklets of the 1968-081E fragments and the 1977-092A fragments at an observation period. The origins of tracklets can be distinguished deterministically if the predicted motions of fragments of target breakups are clearly distinguished as will be demonstrated in this study.

### 3.2.1 Theoretical confirmation

This section addresses origin identification process at the observation points specified in Table 3.2 using the predicted motions of 1968-081E fragments, 1977-092A fragments generated by the OD generation process, and the catalogued fragments of 1968-081E and 1977-092A as the pseudo observation data.

To conduct motion prediction, the conditions are defined as follows. The sensor resolution factor refers to the CCD's resolution specified in Table 2.1, and the temporal length of an image sequence is measured as 7.0 minutes. The period of motion prediction is set as one-night observation period (5 March 2011 21:00-29:00 JST), which is also feasible to predict a

motion of several nights around the defined observation term. The FOV size is assumed as 1° by 1°. The orbits of the catalogued fragments whose trajectories will exist at the FOV during the observation period are extracted from the SSN catalogue.

Figure 3.3 shows the predicted motions of the target fragments and the possible motions of pseudo tracklets of the catalogued fragments at the coordinate I. Possible regions of the predicted motions are represented as contour distribution with green-blue-pink probability lines. As the contour distribution indicates, a predicted motion of fragments from a breakup forms a uniform and clear distribution at a fixed observation coordinate. In addition, the predicted motion has a peak region in its single distribution. Coordinate I has only a contour of 1968-081E fragments because the population of 1968-081E is dominant here. Vertical motion of the fragments is dominant in the coordinate I. The cataloged objects (1968-081G, L, H), which are represented in red plots, can be detected inside the higher probability region (green line). The variations of red plots, i.e., the motion vectors of the known fragments, are due to the temporal variation of the observation site's position and velocity relative to the observation coordinate. Also, the cataloged objects associated with 1977-092A do not present in the coordinate I. Thus, one can selectively observe and identify the fragments associated with 1968-081E at the coordinate I.

Figure 3.4 shows the predicted motions of the target fragments and the possible motions of pseudo tracklets of the catalogued fragments at the coordinate II. Because the coordinate II has both populations of 1968-081E fragments and 1977-092A fragments, there are two contour distributions; the bottom one indicates the predicted motion of 1968-081E fragments and the top one indicates the 1977-092A fragments. Vertical motion is dominant for each contour distribution, and the difference of vertical motion magnitude separates the both contour distributions. The cataloged objects (1968-081G, and 1977-092A, K), which are represented in red plots, can be detected inside a higher probability region at a corresponding contour distribution. In this case, one can hardly distinguish the origins of detected objects if the motion vector plots in the lower probability region such as between 1e-5 % and 5e-5 % lines. Consequently, one can selectively observe and identify the fragments associated with 1968-081E or 1977-092A at the coordinate II if motion vectors of detected objects correspond to the higher probability region.

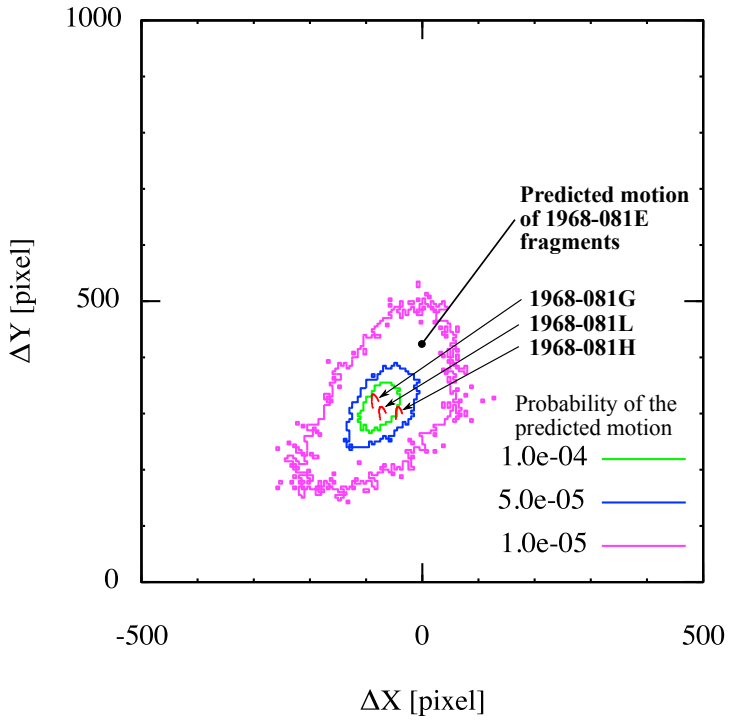


**Figure 3.3: Predicted motion of 1968-081E and 1977-092A fragments at the coordinate I as of 6th March 2011 (100 MC Runs, Debris Size ≥ 10 cm).**

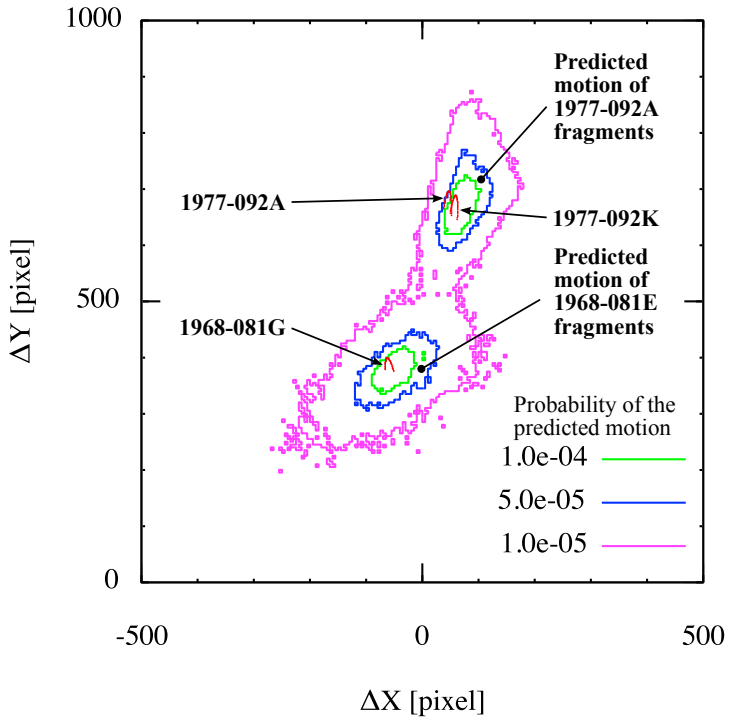


**Figure 3.4: Predicted motion of 1968-081E and 1977-092A fragments at the coordinate II as of 6th March 2011 (100 MC Runs, Debris Size ≥ 10 cm).**

### 3.2.2 Empirical confirmation

To further verify capabilities of the approach II, an observation campaign of 1968-081E and 1977-092A fragments is conducted at JNO in February 2012. The campaign consists of 2-night survey observation and 1-night follow-up observation. The populations of 1968-081E and 1977-092A fragments at the observation period are predicted for the observation coordinate selection. Figure 3.5 represents the predicted population of the target fragments at the observation period by an illustration technique different from the previous one (Figure 3.1) to try to provide an intuitive viewpoint for the multiple breakups populations. The number of trajectories of fragments are counted in each bin, whose size is 1° by 1°. This illustration technique represents the features of the populations by Red-Green-Blue (RGB) color. The 1968-081E fragments population is proportional to the red component, and the 1977-092A fragments population is proportional to the blue component, whereas the sum of each population is proportional to the green component. 8-bit resolution (i.e., 0-255 counts) is allocated to each color component. Thus, the orange distribution specifies the 1968-081E fragments population, and the light-blue distribution specifies the 1977-092A fragments population. The regions, where a large number of trajectories exist, are represented in brighter colors. The white region, especially, represents both 1968-081E fragments and 1977-092A fragments exist at the highest number. The observation point for this empirical confirmation is at ($\alpha$, $\delta$) = (176.5°, -4.5°). At this coordinate, trajectories of 77% of all 1968-081E fragments and 66% of all 1977-092A fragments will exist, thus characteristics of this coordinate are same as the aforementioned coordinate II.

The sensor at JNO consists of the 35-cm aperture telescope and the CCD camera, whose FOV is 1.27° by 1.27°. The readout chips on the CCD camera are modified to improve the readout time to be 1.6 seconds per one image, compared with the CCD camera used in the Chapter 2. It may be noted that the sensor resolution remains same. Thus, this empirical confirmation sets the temporal length of an image sequence to be 200 seconds, and the observation period to be 240 seconds to make use of the faster read-out time. One image sequence consists of 36 images with 4.0 seconds exposure time for each image.

As a result of the observation campaign, 180 sets of image sequences are acquired from 2-night surveys. A total observation period for each night is 6 hours. The line-identifying technique (Yanagisawa *et al.*, 2009) is applied to the acquired image sequences to detect debris

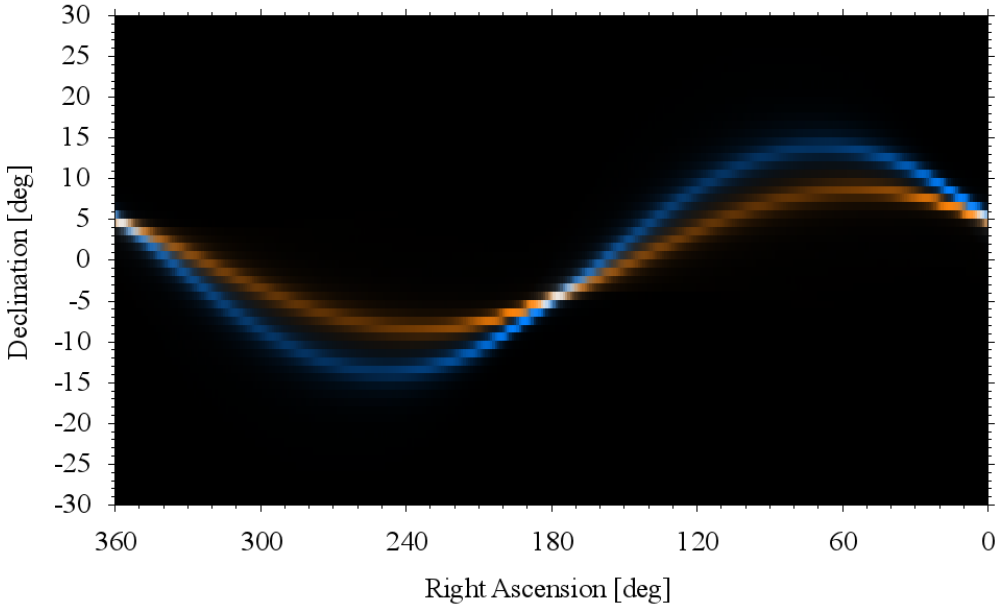


**Figure 3.5: Predicted populations of 1968-081E and 1977-092A fragments at the observation period (100 MC runs, debris size ≥ 10 cm).**

in near-real time at JNO. 16 UCTs are detected from the 2-night surveys, and finally 2 physical objects, which are named UCT1 and UCT2 respectively, are identified from the 16 UCTs.

Figure 3.6 compares the predicted motion of 1968-081E fragments and 1977-092A fragments with the motion of CTs and UCTs detected by the two-night survey observation. Motion vectors of UCT1 are measured as $(\Delta X, \Delta Y)$ = (-48, 220) at the first night and $(\Delta X, \Delta Y)$ = (-49, 220) at the second night, whereas those of UCT2 are measured as $(\Delta X, \Delta Y)$ = (48, 380) at the first night and $(\Delta X, \Delta Y)$ = (48, 385) at the second night. UCT1 appears inside the predicted motion of 1968-081E fragments, whereas UCT2 appears inside the predicted motion of 1977-092A fragments. Thus, UCT1 and UCT2 are associated with 1968-081E and 1977-092A, respectively. On the other hand, there are 6 CTs (1973-100B, 1974-094A, 1977-048G, 1977-071F, 1977-092G, 1978-073A) which appear inside the predicted motion of 1977-092A fragments, since their orbital evolution is quite similar to the orbital evolution of 1977-092A. Thus, the origin identification of UCTs using backward propagation must be performed even though they appear inside the predicted motion of fragments at the observation period.

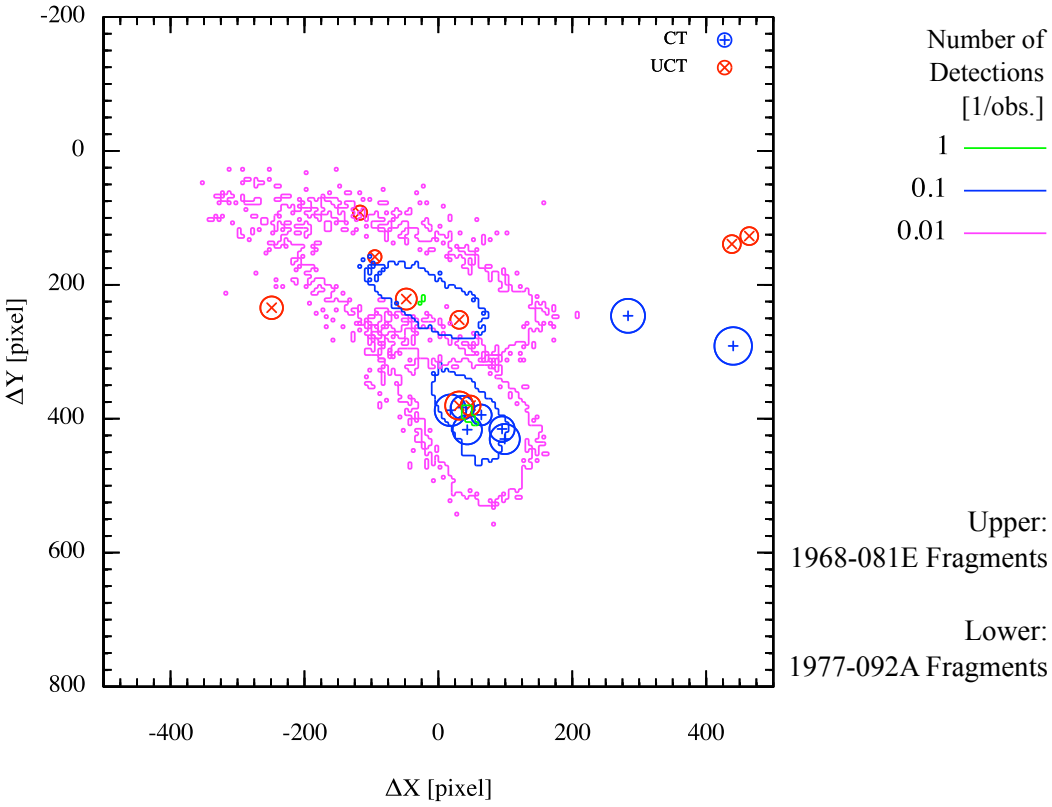


**Figure 3.6: Comparison in motion between predictions and measurements.** - A measured motion with a larger circle represents a brighter object. The upper contours distribution represents the predicted motion of 1968-081E fragments, and the lower contours distribution represents the predicted motion of 1977-092A fragments.

## 3.3 Orbit identification

This section empirically confirms whether or not one can identify the right origins of UCT1 and UCT2 detected through the survey observation conducted in Section 3.2.2. 1-night follow-up observation is conducted to track UCT1 and UCT2 to precisely determine their orbits. This study evaluates the evolution of the orbital plane vectors of UCT1 and UCT2, which is acquired as a result of backward propagation. The orbital plane vector of an object in the geostationary region experiences a clock-wise evolution around a stable point in the $i\cos(\Omega) - i\sin(\Omega)$ plane as demonstrated in Section 2.5. On this plane, moreover, fragments of a single breakup form a linear distribution at the breakup epoch. A combination of these evidences and the backward orbit propagation will enable to identify a right origin of each UCT at the breakup epoch.

Figure 3.7 demonstrates the backward propagation of UCT1 (colored in magenta) and UCT2 (colored in cyan) in the $i\cos(\Omega) - i\sin(\Omega)$ plane. This backward propagation adopts special perturbation theories including perturbation forces by non-spherical part of the Earth gravity (by applying EGM96 to the 8th order), third bodies (the Sun and the Moon), and SRP. A/m of 0.01 $m^2$/kg is assumed for each UCT. Red dots and blue dots represent the initial distribution of 1968-081E fragments and 1977-092A fragments, respectively. UCT1 is on the initial distribution of 1968-081E fragments at the time of the 1968-081E explosion (+ in magenta), but not on the initial distribution of 1977-092A fragments at the time of the 1977-092A explosion ($\times$ in magenta). Thus, UCT1 can be associated with the 1968-081E explosion. However, UCT2 is not only on the initial distribution of the 1968-081E fragments at the time of 1968-081E explosion (+ in cyan) but also on the initial distribution of 1977-092A fragments at the time of the 1977-092A explosion ($\times$ in cyan). Thus, UCT2 cannot be associated with the 1977-092A explosion, deterministically.

Here this study adopts a pinch point analysis in the $\alpha - \delta$ plane in order to identify the right origin of UCT2. In the immediate aftermath of a breakup, orbits of all breakup fragments cross at the breakup position, which is defined as the pinch point. Figure 3.8 plots the orbit of 1968-081E, UCT1 and UCT2 at the time of the 1968-081E explosion. The symbol + in red represents the pinch point where the Transtage (1968-081E) exploded. The orbit of 1968-081E and UCT1 passes through the pinch point, but the orbit of UCT2 does not. Therefore, Figure 3.8 confirms that UCT1 is originated from the 1968-081E explosion. Figure 3.8 also confirms

that UCT2 is not originated from 1968-081E explosion. Finally it is concluded that UCT2 can be associated with the 1977-092A explosion.

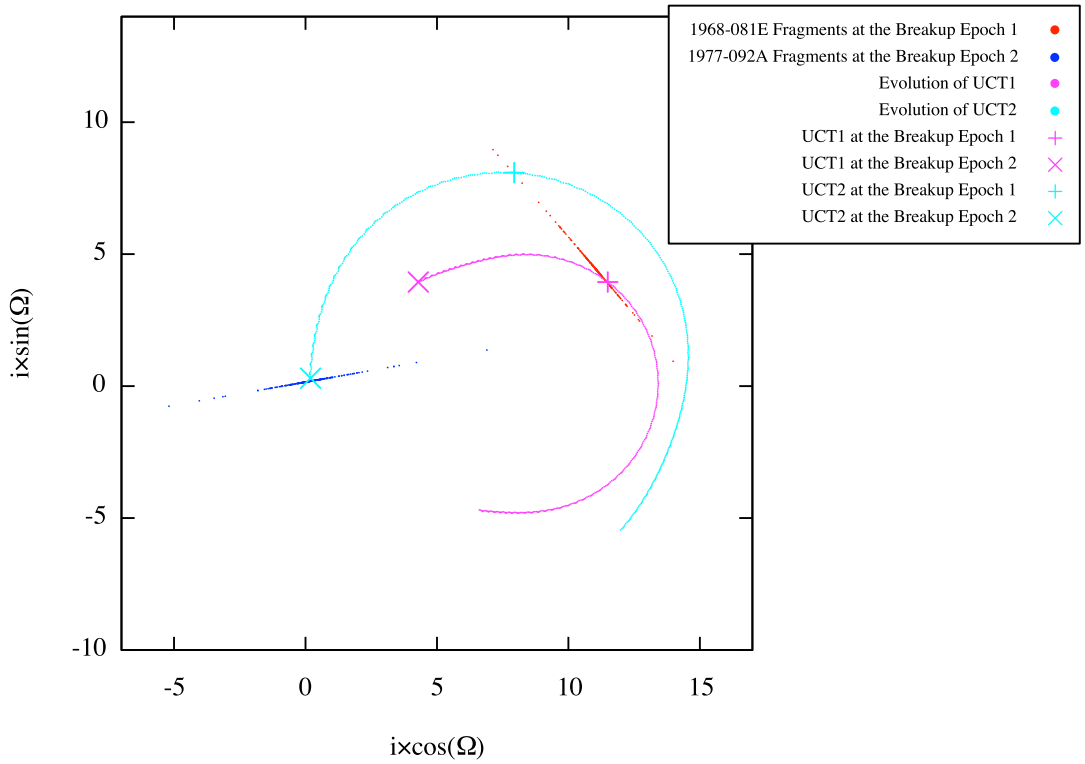


**Figure 3.7: Backward propagation of UCT1 and UCT2.**

## 3.4 Summary

This chapter demonstrated the deterministic origin identification that one could distinguish between multiple breakups in a single series of observations and identify a right origin of a UCT detected at the observation point where trajectories of fragments originated from the multiple events exist. Capabilities of the deterministic origin identification were confirmed by theoretical and empirical aspects.

The theoretical confirmation showed that one could specify an observation point to observe fragments of a single breakup and also an observation point to observe fragments of multiple breakups. The predicted motions of multiple breakups at both types of the observation points were distinguished at a certain degree, which could be applied to origin identification of

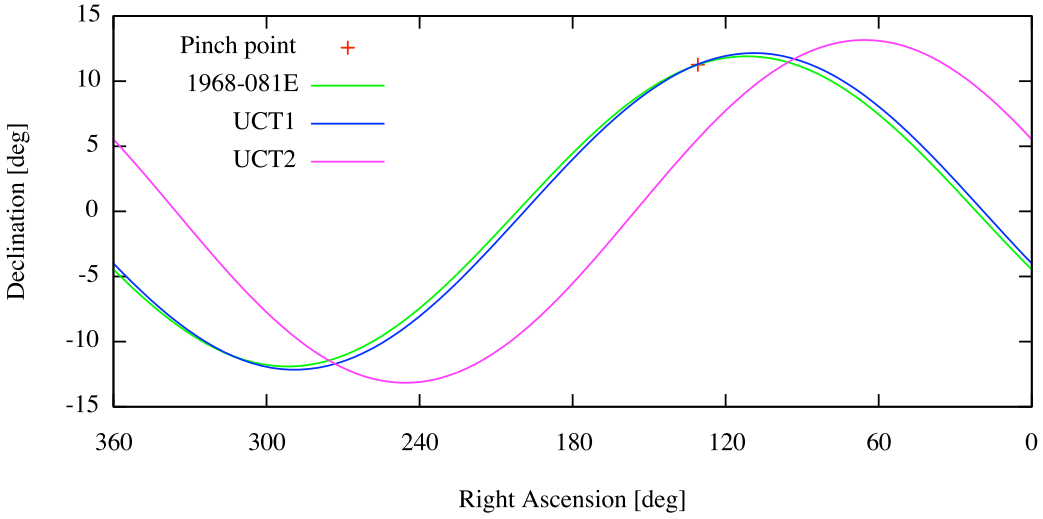


**Figure 3.8: Pinch point analysis at the breakup epoch of 1968-081E.**

detected UCTs at the specified observation points.

The empirical confirmation performed actual observations, based on the outcomes of the theoretical confirmation, to search fragments of multiple breakups and to identify a right origin of each object detected. The follow-up observations successfully observed two UCTs, named UCT1 and UCT2 respectively to determine their orbits. Two origin identification approaches using the orbital plane vector and the pinch point clearly identified the right origins of UCT1 and UCT2. From the results obtained, it was confirmed that a detected fragment had to be associated with every one of the breakup features: the motion vector, the orbital plane vector, and the pinch point.

This chapter concludes that one can identify a right origin of each fragment detected in optical surveys when hypotheses of breakups to be considered are well-known and a proper observation point is selected. The deterministic origin identification demonstrated in this chapter can be applied to verify relations between orbital anomalies and breakups as will be demonstrated in Chapter 6.

# 4

# Probabilistic origin identification

This chapter proposes an approach to associate origins of tracklets with spacecraft breakup events occurred in the geostationary region. The tracklet denotes a spatial-temporal series of signals associated with a space object. In typical OD observations of the geostationary region, one usually detects tracklets from optical images taken during observations. By analyzing a detected tracklet in the optical images, one can acquire parameters of a space object at each of the observation epochs such as position in the celestial sphere, the angular velocity, and brightness. Origin identification of tracklets is an essential matter in the observations. When maintaining an orbital catalogue of space objects, one usually classifies origins of detected tracklets into the catalogued objects and the uncatalogued objects by associating the propagated states of a cataloged object with the measured states of a tracklet at the observation epoch. Once having found an origin of a tracklet, one can apply the results to such matters as orbit determination of the space object, population analyses in surveyed regions, and OD environmental modeling. To contribute to the OD environmental modeling, however, the aforementioned classification is insufficient. If the uncatalogued objects are unlikely to associate with newly launched objects, operational debris, or intentionally uncatalogued objects, one should associate their origins with events that generated OD. In the optical observations in the geostationary region, the majority of the observable OD, whose size is on the order of ten centimeters or larger, will be associated with spacecraft breakup events.

The approach to be proposed utilizes OD modeling techniques to effectively conduct prediction, detection, and classification of breakup fragments. Two techniques are applied to get probable results for origin identifications. First, the proposed approach selects an observation

point where a high detection rate for one breakup event among others can be expected. Second, tracklets are associated with the prediction results according to their angular velocities. The second technique investigates which breakup event a tracklet would belong to, and its probability by using a k-nearest neighbor (k-NN) algorithm.

This chapter verifies the proposed approach by applying optical observation data of breakup fragments. A well-known breakup event of the rocket body US Titan 3C Transtage (1968-081E) is selected as the primary observation target, and then optical observations are conducted by the campaign between two sensors in Taiwan and one sensor in Japan. While three nights observations, an enhanced stacking method detects 96 tracklets that are uncorrelated with the SSN catalogue at the observation epochs, and finally 50 tracklets among them are associated with the breakup event of 1968-081E.

## 4.1 Approach

Figure 4.1 schematically illustrates the framework of the proposed approach. The framework consists of the OD modeling, the predictions, the observation, the detection, and the two-step origin identifications. The main component of the framework is the two-step origin identification, so that this section mentions it first, and then the other components.

The first step of the origin identification adopts a common method: the orbits of catalogued space objects are propagated to the observation epochs of detected tracklets first, and then each of the propagated space objects are associated with a detected tracklet in terms of the angular position and the angular velocity in the celestial sphere. If a space object matches a tracklet within defined thresholds, the tracklet is regarded as the space object. The threshold for the angular position should be the scale of the FOV or smaller, whereas the threshold for the angular velocity should be in the order of arc-minute or smaller. By this step, one can classify the detected tracklets into the catalogued and the uncatalogued space objects. This method is only valid for space objects involving short-term orbit propagation (i.e., not months nor years). The short-term propagation is capable of predicting appropriate angular positions, but the long-term propagation is not. Usually most of orbits of catalogued space objects are refreshed at days or weeks so that their angular positions at observation epochs will be predicted appropriately. Breakup fragments, however, require long-term propagation from their breakup

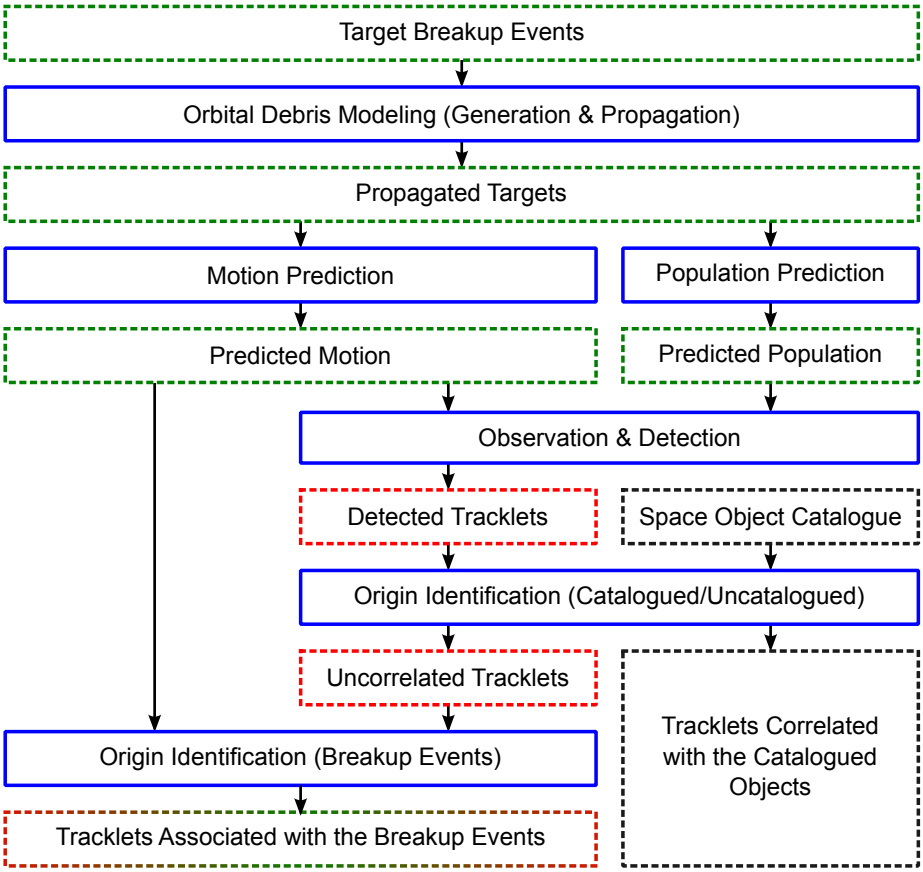


**Figure 4.1: The framework of the proposed approach.**

epochs to an observation epoch so that their predicted angular positions at observation epochs become random anymore and therefore another origin identification step is required.

The second step of the origin identification applies an observable characteristic of breakup fragments: a group of fragments associated with a breakup event would have single and distinct distribution in the angular velocity plane when one observes them in an inertial point overnight, as verified in Section 2.2.2. This feature, thus, can associate tracklets with breakup events. To quantitatively associate the observations and the predictions, the classification method widely used in pattern recognition researches is adopted: the k-NN algorithm (e.g., Bishop *et al.* (2006)). Figure 4.2 illustrates the concept of the k-NN algorithm. The origin of an observation is determined by the majority voting by the k-predictions near to the observation in an observable space. The k-NN algorithm is superior to classification algorithms using histogram, because accuracy of the classification by the k-NN algorithm does not depend on the grid scale or origin. One has to be careful about selecting the number of the neighbors (k) to reduce error judgments. The advantage of this origin identification method is that one requires orbital propagation for the objects generated by the OD modeling only so that orbit determination nor orbit propagation are not required for detected tracklets. This approach enables to reduce uncertainty that may come from detected tracklets.

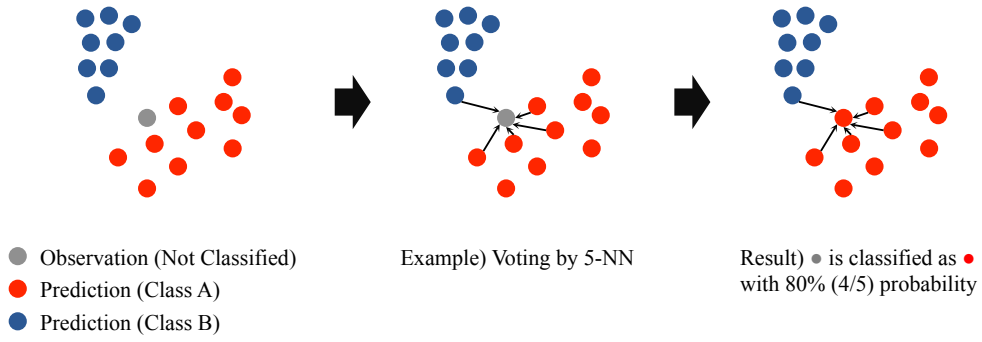


**Figure 4.2: Concept of the k-NN algorithm.**

As shown in Figure 4.1, the population prediction and motion prediction introduced in Section 2.2.1 and 2.2.2 are applied to the proposed approach. One selects an observation point where the detection rate for tracklets associated with a breakup event, which is defined as the primary target, will be high, so that one can determine the probable origins for the primary target. The predicted motion is also applied to optimize an exposure time for the primary target.

## 4.2 Observation planning

This section demonstrates the proposed approach from the beginning to the population prediction and motion prediction. Final outcomes in this section include a single observation point where the high detection rate for a selected target will be expected, and an optimum exposure time for the selected target.

### 4.2.1 Target breakup events

To verify the proposed approach, breakup fragments are going to be searched by utilizing the breakup event list investigated by Oswald (2008), as summarized in Table 4.1. The list includes the breakup events of six Titan 3C Transtages, four satellites, and two artificial events (AE-02 and AE-03) that could not be associated with real space objects. In the list, each of the breakup events also include such as a probable parent object and its event epoch. The orbital elements at the event epochs are detailed in the reference (Oswald, 2008).

**Table 4.1:** Breakup events in the geostationary region (Oswald, 2008)

| ID | Name | Event epoch (YYDDD.DDDD) |
|---|---|---|
| 1966-053J | TITAN 3C TRANSTAGE R/B | 87276.6882 |
| 1967-066G | TITAN 3C TRANSTAGE R/B | 94045.4161 |
| 1968-081E | TITAN 3C TRANSTAGE R/B | 92053.3745 |
| 1973-040B | TITAN 3C TRANSTAGE R/B | 81067.2007 |
| 1975-117A | SATCOM 1 | 99257.6799 |
| 1975-118C | TITAN 3C TRANSTAGE R/B | 87072.6430 |
| 1977-092A | EKRAN 2 | 78174.0000 |
| 1979-053C | TITAN 3C TRANSTAGE R/B | 82309.0000 |
| 1979-087A | EKRAN 4 | 82157.7550 |
| 1988-018B | TELECOM 1C | 02263.0000 |
| (AE-02) | - | 98180.0000 |
| (AE-03) | - | 92280.0000 |

A primary target is selected from the twelve breakup events to make the detection rate of the primary target become the majority among the other events. The most adequate target is the confirmed event of the Titan 3C Transtage (1968-081E) because large number of fragments has been spotted at near the breakup epoch, as reported in Pensa *et al.* (1996). The US SSN

now tracks 24 fragments associated with 1968-081E that are catalogued as of May 2013 (including 1968-081G, H). It should be noted that, only eight fragments were catalogued when the observations for this research were conducted.

### 4.2.2 Observation conditions

An observation campaign for the breakup fragments is conducted from 20 October 2011 to 22 October 2011. To detect breakup fragments, whose individual presences, individual orbits, and temporal positions are not confirmed yet, one should observe a specific coordinate for long period. Change of weather condition and any operational troubles will suffer detectability at observation sites. Thus, the reason to take a campaign style observation is to gain a good detectability, i.e. to detect a sufficient number of tracklets associated with 1968-081E to characterize the breakup event of 1968-081E.

Observation campaign is conducted between two sites: one is the National Central University (NCU) Lulin Observatory in Taiwan, located at 120°52'25"E, 23°28'07"N, and 2862-m altitude, and the other is JNO, located at 138°10'18"E, 35°54'05"N, and 1870-m altitude. Two sensors at the NCU Lulin Observatory were used for the observation campaign, so that this study distinguishes between them. One, called TAOS, consists of 50-cm aperture telescope and 2k by 2k cooled CCD, with a FOV of 1.74° by 1.78°. The other, called LOT, consists of 1-m aperture telescope and 4k by 2k cooled CCD, with a FOV of 26.4' by 13.2'. On the other hand, this study calls one sensor at the JAXA Nyukasa Observatory by JNO. JNO consists of 35-cm aperture telescope and 2k by 2k cooled CCD, with a FOV of 1.27° by 1.27°. The locations and properties of the sensors are depicted in Figure 4.3. TAOS and JNO will have a priority in survey observations because of their large format CCD, and LOT will be suited for follow-up observations by its fine sensor resolution. It should be noted that the following contents are focused on the results acquired from TAOS, because TAOS acquires a sufficient number of images that contribute to the verifications whereas JNO is affected by bad weather conditions and LOT is troubled by minor issues of sensor operations.

### 4.2.3 Predictions and observation point selection

The proposed approach adopts the NASA standard breakup model 2001 revision (Johnson *et al.*, 2001) to OD generation. In the OD generation, one has to configure the scaling factor

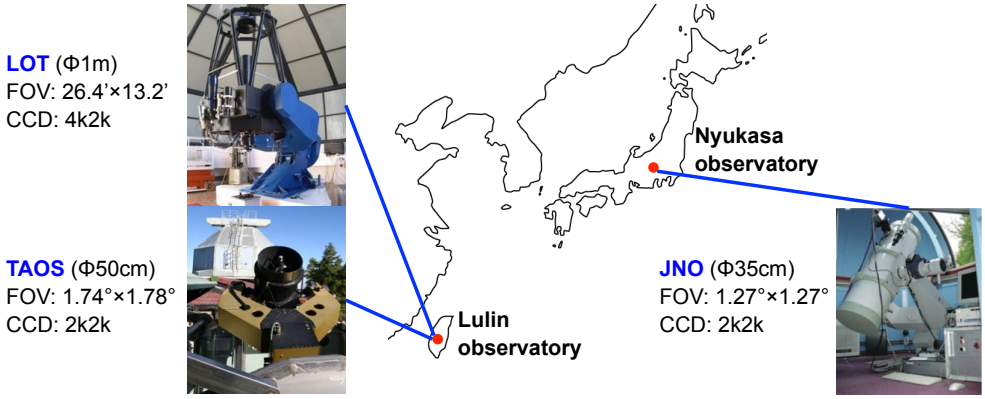


**Figure 4.3: Locations of the sensors employed in the observation campaign.**

that governs the number of fragments to be generated by a breakup event in the NASA model. The scaling factors for all the twelve breakup events are coordinated to 1.0 for the initial guess. For the scaling factor of 1.0, the NASA model generates 238 fragments larger than 10 cm. The orbital propagator adopts the general perturbation techniques including the $J_2$ effect, the lunisolar gravitational attraction effect, and the solar radiation pressure effect. One hundred MC runs are applied to the OD generation and propagation processes to represent mean value and standard deviation of prediction results.

First, this section overviews the predicted population of 1968-081E fragments. This section proposes to evaluate the population at a FOV as the time-integrated number of fragments during a given observation period. The time-integrated number is calculated by adding coverage of the orbit of each fragment during the observation period ($T_{obs}$) to the effective number of each fragment, introduced in Eq.(2.3). This theory considers the detection probability at the moment the observation starts and the detection probability during the observation period. Hence, the time-integrated number of k-th fragment in a FOV, $d_k$, during the observation time, $T_{obs}$, can be expressed by

$$d_k = p_k + \frac{T_{obs}}{T_k} \tag{4.1}$$

The summation of Eq.(4.1) represents the expected number of detections of fragments at the FOV during observations.

Figure 4.4 represents the predicted population of 1968-081E fragments in terms of the time-integrated distribution during a given observation time. For the initial guess, Figure 4.4 assumes the observation time as the operational time of the sensor, which is six hours per night.

In this case, the time-integrated distribution represents the number of fragments that will pass through a bin (1° by 1° for this case) at each night. If the observation time is defined as the sum of exposure time of a sensor at a night, then the time-integrated distribution represents the detection rate of the fragments at the bin. As described in the previous section, the predicted population of 1968-081E fragments clearly distinguishes a dense region from others at each geocentric right ascension column. Considering the Earth shadow and the visible and invisible region during the observation period, one should select the observation point from the dense regions in the right side of Figure 4.4. Up to 51.6 fragments will pass through the densest bin at ($\alpha$, $\delta$) = (6°, 5°) during six hours.

Fig. 4.5 represents the angular velocity of 1968-081E fragments at a peak bin in each geocentric right ascension column that is specified in Figure 4.4. As mentioned in the previous section, an observer measures a space object with non-sidereal mode (i.e. fixed in azimuth and elevation), so that TAOS becomes the observer to measure the angular velocity predicted in Figure 4.5. The mean angular velocity has a maximum difference of approximately 2.0 ”/seconds. If one wants to keep the motion of center-of-light of the fragments within one pixel (e.g. 1 pixel = 3” by 3”) per each shot, the maximum difference of the angular velocity will alternate the exposure time by 1.5 seconds. Such a difference in an exposure time results in a serious one in the total exposure time of a night.

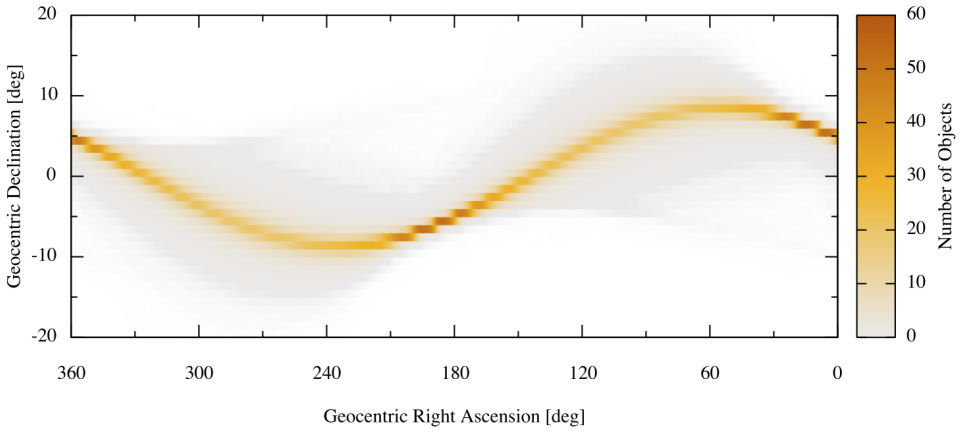


**Figure 4.4: Predicted population of 1968-081E fragments in time-integrated distribution during six hours.** - Bin size is 1° by 1°.

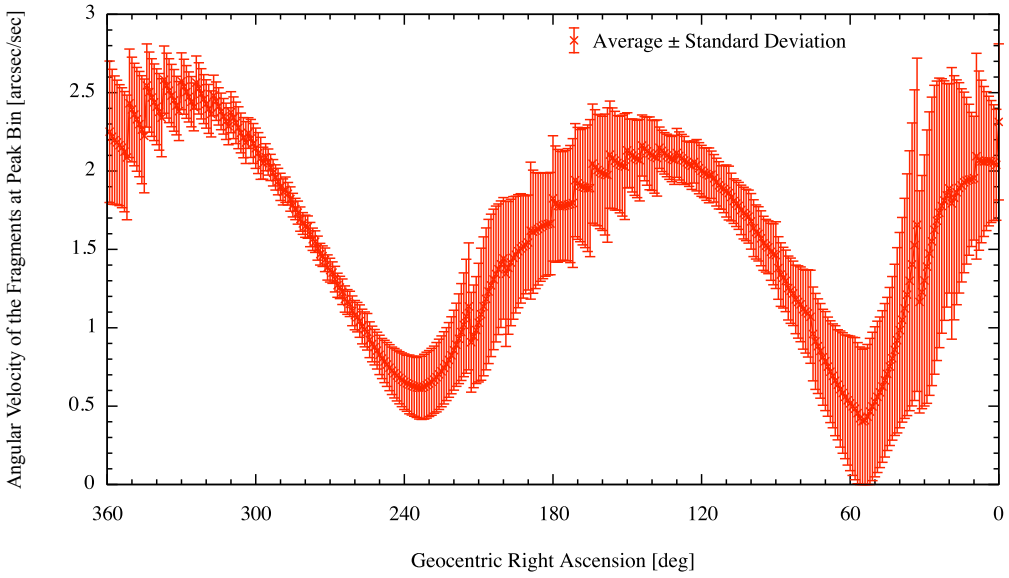


**Figure 4.5: The angular velocity of 1968-081E fragments at peak bins specified in Figure 4.4.** - The observer is at the Lulin Observatory in this case.

Second, this section determines the observation point by evaluating the predicted population and motion. Table 4.2 summarizes the predicted population scaled for the sensor size of TAOS, and the angular velocity in terms of average ± standard deviation. Two points (A and B) are compared as candidates. Point A is the bin of (6°, 5°) where the predicted population is the highest among whole bins, whereas Point B is the bin of (43°, 8°) where the traveling speed is almost half of Point A but the predicted population is also half.

**Table 4.2:** Comparisons of the predicted population and the angular velocity of 1968-081E fragments at TAOS during six hours observation.

| Profile | Point A | Point B |
|---|---|---|
| Predicted population | 56.47 ± 1.09 | 39.95 ± 1.80 |
| Angular velocity [”/sec] | 2.01 ± 0.55 | 0.87 ± 0.61 |

For this observation campaign, Point B is selected as the observation point because the detectability for individual fragments largely depends on the signal-to-noise ratio affected by the exposure time. The detectability resulting from the population is the second priority at this observation campaign. To maximize an exposure time with assumptions of keeping the motion of the fragment within one pixel or within the seeing size, the exposure time is determined as 5.9 seconds at Point B, whereas this values would decrease to 3.0 seconds at Point A.

As previously mentioned, this observation campaign aims to get a high detection rate for 1968-081E fragments among the targeted twelve breakup events. Figure 4.6 compares the detection rates of fragments from each of the targeted breakup events. In this evaluation, the detection rate represents the expected number of detections during six hours observations at TAOS. The result shows that the detection rates of 1968-081E fragments and 1967-066G fragments become the majority in the selected observation point. The detection rate of 1968-081E fragments spares 42% of the sum. Thus, even if one does not demonstrate the origin identification using the k-NN algorithm, it can be said from the Bayesian estimation viewpoint that all of the tracklets uncorrelated with the catalogued space objects will be associated with 1968-081E fragments with 42% probability.

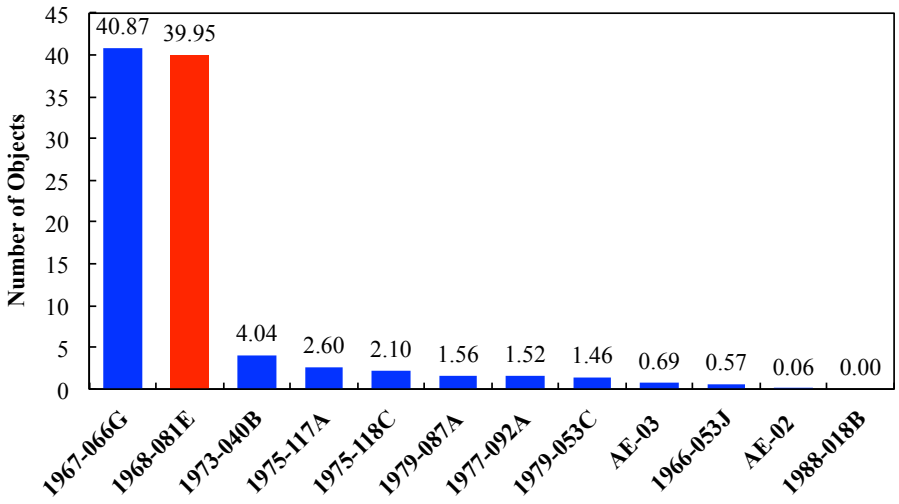


**Figure 4.6: Comparison of the detection rates between the twelve breakup events during six hours observation at Point B.**

## 4.3 Tracklets identification

As a result of the observation campaign, TAOS acquires 189 sets of valid image sequences during three nights. In this section, the proposed approach is finally verified by conducting the origin identification of uncorrelated tracklets. First this section summarizes tracklet detections at TAOS and their origin identifications using the SSN catalogue, and then devotes to the demonstration of the origin identifications using the OD modeling results and the k-NN algorithm.

### 4.3.1 Tracklet detection and the SSN catalogue correlation

In this research, the FPGA-based stacking method (Yanagisawa *et al.*, 2012) is applied to detect tracklets from image sequences acquired at TAOS. The stacking method is based on the TBD algorithm, which assumes the motion vector of tracklets on a sensor frame first, and then stacks image sequences shifted along with the motion vector. The TBD algorithm can detect fainter signals by one or two apparent magnitude than conventional detection algorithms, which detect signals in an image first and then track the detected signals in image sequences to identify tracklets. TBD generally requires, though, very high computational performance because it has to try a lot of motion vectors to stack image sequences to detect tracklets. The FPGA-based

stacking method resolves the problem by implementing the algorithms onto FPGA. Thirty minutes are taken to process a set of image sequences with trials of 262,144 motion vectors (i.e. the motion vectors whose components are within the range of 256 pixels per a image sequence).

In total, 147 tracklets are detected from the 189 sets of TAOS images by the FPGA-based stacking method. By applying the first step of the origin identification to the 147 tracklets, 51 tracklets are correlated with space objects in the SSN catalogue whose release date is near to the observation period, whereas the others (i.e., 96 tracklets) are judged as uncataloged ones. The faintest object detected is down to 19.0 apparent magnitude, which corresponds to approximately 16 cm in diameter assuming a Lambert sphere object whose albedo is 0.1.

### 4.3.2 Origin identification by the k-NN algorithm

This section addresses the origin identification of the 96 tracklets that are uncorrelated with the space objects in the SSN catalogue. To begin with this step, this section evaluates the predicted motion of the fragments of the twelve breakup events. In Figure 4.7, the predicted motion of 1968-081E fragments is visualized as red, and the others as blue. Transparent gradient is applied to both colors to distinguish the frequency of the presence of fragments in the motion plane grid. The gradient scale is same for both colors. This two-dimensional distribution will give more probable decision viewpoint to the origin identification than the information in Figure 4.6. It should be noted that, 1968-081E fragments near the dense red region are overlapped by the other breakup fragments. For example, 1967-066G fragments are appeared in the densest blue region. They may give some votes to a tracklet to be plotted in and near the overlapped region.

To apply the k-NN algorithm to the origin identification, one has to determine the adequate k for the observation point of TAOS because too small k or too large k will result in increasing misclassification for origins of tracklets. As a preliminary analysis this section conducts the cross validation using the predicted motions of the entire breakup fragments. In the cross validation, one of the predictions is regarded as a pseudo tracklet (i.e., an observation) and perform the k-NN algorithm for each of the pseudo tracklets. The cross validation result is summarized in Figure 4.8. As a result of the cross validation, it is found that 10-NN is adequate: the misclassification rate well converges with the minimum degree (the order of 8%) from k =

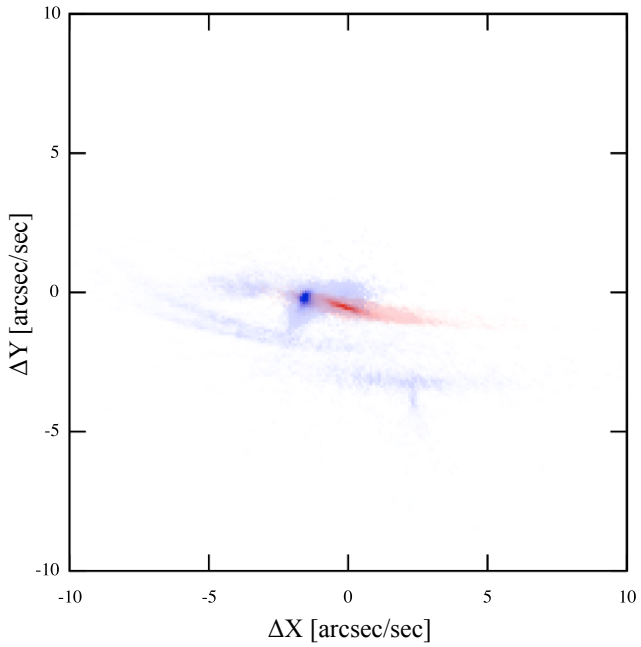


**Figure 4.7: Predicted motions of 1968-081E fragments in red gradation and the other fragments in blue gradation.**

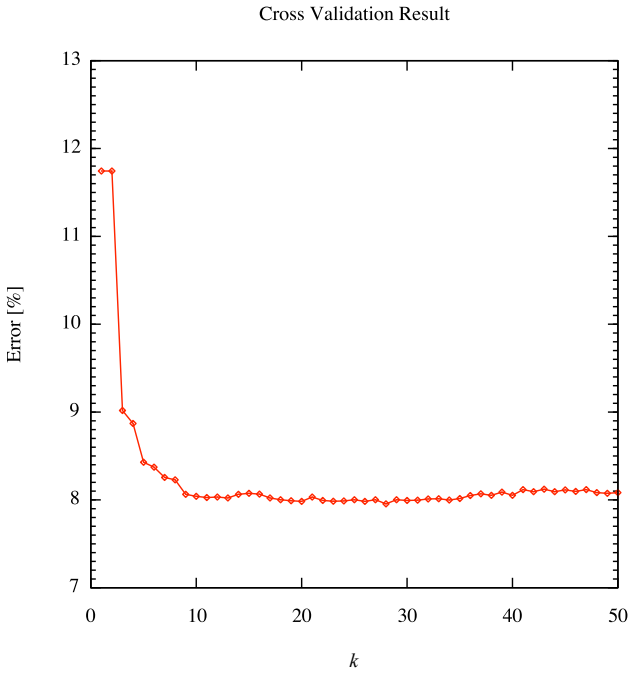


**Figure 4.8: The cross validation result to determine the number of voters ($k$).**

10. To prevent a misleading, it should be noted that k = 10 does not denote ten nearest grids in Figure 4.7, but denotes ten nearest tracklets in the raw data of Figure 4.7.

Figure 4.9 visualizes the result of the origin identification of the 96 tracklets in comparison with the predicted motion. In the figure, a detected tracklet is represented as a point colored by the gradient from blue to red. The color gradient is linear to the ratio ($P$) of 1968-081E fragments in the 10-NN. For example, a tracklet of $P$ = 100% is colored red, a tracklet of $P$ = 50% is colored violet, and a tracklet of $P$ = 0% is colored blue. The 10-NN clearly distinguishes the probable origins of tracklets between 1968-081E and the others. Following the classification concept using the k-NN algorithm, this section classifies the origin of a detected tracklet from the viewpoint that which breakup event among the twelve becomes the majority of the 10-NN for the detected tracklet.

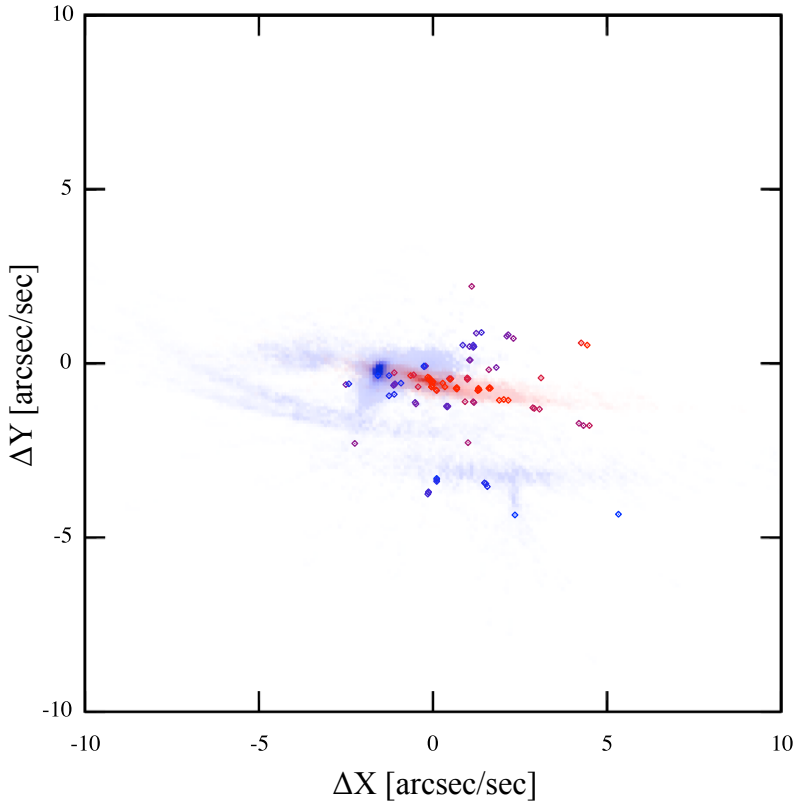


**Figure 4.9: Comparison between predicted motions of 1968-081E fragments and measured motions of the 96 tracklets uncorrelated with the SSN catalogue.** - The origin identification results for the tracklets are visualized by the gradation from blue to red. A red tracklet represents its probable origin is 1968-081E, and a blue tracklet represents its probable origin is one of the other breakup sources.

As a result, 50 tracklets are classified as 1968-081E fragments. Figure 4.10 shows the distribution of the 50 tracklets in comparison with the predicted motion of 1968-081E fragments (in left) and the predicted motion of the other fragments (in right). The 50 tracklets are distributed in and around the predicted motion of 1968-081E fragments, and apart from the predicted motion of the other breakup fragments. Among the 50 tracklets, 29 tracklets have $P$ = 100%, 10 tracklets have $P$ = 80%, and 11 tracklets have $P$ = 60%. Some of the tracklets having lower $P$ are distributed near the dense blue region, and the other lower $P$ tracklets are distributed apart from the dense red region. Two tracklets plotted at $(\Delta X, \Delta Y)$ = (4.26, 0.60) and (4.43, 0.54) are unlikely to be associated with 1968-081E, but are voted by 1968-081E fragments because there are no other predicted fragments between the two tracklets and 1968-081E fragments. This case is a typical example of the misclassification by k-NN. One may need to revise hypotheses used in the predictions such as breakup conditions to reduce unlikely classification. It may be noted that there are 11 more tracklets voted by 1968-081E fragments but their votes are too small to take into consideration major revisions of the hypotheses.

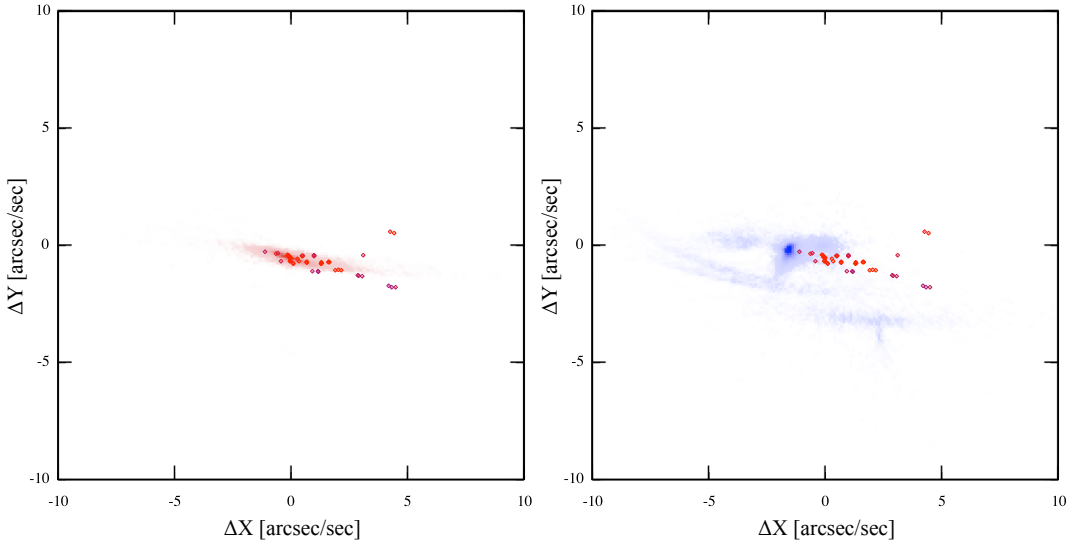


**Figure 4.10: Comparison between measured motions of the 50 tracklets associated with 1968-081E and predicted motions of 1968-081E fragments (in left) and the other fragments (in right).**

## 4.4 Summary

This chapter proposed a comprehensive approach to associate tracklets with the breakup events in the geostationary region. This chapter verified the proposed approach by conducting the predictive analyses, the actual observations, the tracklet detections, and the origin identifications. This verification study adopted the breakup event list investigated by (Oswald, 2008) that can be regarded as the most probable sources at this time for the historical breakup events in the geostationary region. The breakup event of 1968-081E was selected from the event list as the primary target to effectively verify the proposed approach. The observation campaign for the primary target was conducted at the NCU Lulin Observatory and the JAXA Nyukasa Observatory. From three-nights survey observations, a significant number of tracklets were detected by the FPGA-based stacking method, and the two-step origin identification method finally associated 50 tracklets with the primary target 1968-081E.

The proposed approach was verified to be capable of investigating the probable origins of detected tracklets. It should be noted that the proposed approach may not be able to deterministically identify the origins of tracklets, but can evaluate a probability of relation between a breakup event and origin of a tracklet. Thus, applications of the proposed approach may include the probabilistic estimation of breakup event characteristics, and the development of an iterative search strategy that can improve the confidences of hypotheses on breakup events, resulting predictions, and origin identification. Those applications will be addressed in Section 5.2.

# 5

# Breakup event characterization

An explosion of an orbiting satellite or rocket generates a large number of fragmentation debris that may induce risk of additional collision breakups between the fragmentation debris and other space objects. This chapter aims to develop a practical method to characterize an explosion breakup, i.e., how fragmentation debris would be generated in an explosion event. The breakup of the Titan 3C Transtage (1968-081E) is selected to demonstrate the characterization. Two characteristics will be assessed in this study. The first one is the fragmentation profile assessment to evaluate the delta-velocity ($\Delta V$) given to each fragment by the parent object at the breakup epoch. The second one is the breakup scale assessment to evaluate the scaling factor ($S$) introduced in the size distribution model of the NASA standard breakup model 2001 revision (Johnson *et al.*, 2001). The delta-velocity estimation result can be utilized to discuss how a parent object experienced the breakup. The scaling factor estimation result, on the other hand, can be utilized to quantitatively assess how the breakup contributed to OD environment. The scaling factor estimation, especially, may not be an essential approach to understand the physical process of a breakup but be a practical approach to measure quantitative contributions from the breakup to OD environment, because better initial states of fragmentation debris can be retrieved by only inputting the reasonable scaling factor to the NASA breakup model. If initial states are properly estimated and thus the breakup event is properly modeled, predictions involving the initial states will be improved. Such initial states are, therefore, important factors to better understand current OD situations and to predict realistic future OD situations for effective OD mitigation and OD remediation.

## 5.1 Fragmentation profile assessment

This section introduces an algorithm to estimate the $\Delta V$ given to each fragment at the breakup epoch and a coordinate system to be applied to the estimation. The fragmentation profile of the 1968-081E breakup will be assessed based on the $\Delta V$ estimation result.

Fragments are scattered from the parent object at the time of the breakup, thus this situation can be translated as follows; the orbits of the parent object and its fragment shares a same inertial point at the breakup epoch, and the $\Delta V$ is given to the fragment at the inertial point. In actual situation, however, one cannot specify the inertial point shared by the parent object and its fragment even at the breakup epoch due to uncertainties caused by orbit determination errors and orbit propagation errors. Thus, $\Delta V$ of each fragment should be estimated at each probable breakup point, where the distance between the parent object and the fragment becomes minimum. This study applies a close approach analysis to find the closest points between the parent object and each fragment at the breakup epoch. The Nelder-Mead method (Nelder & Mead, 1965), which is a well-known extremum-seeking algorithm, is applied to find closest points between each fragment and the parent object at the breakup, i.e., to derive a proper $\Delta V$ for each fragment. Thus, the orbital states of each fragment and the parent object are required for the analyses so that this study uses the latest TLEs of the 22 fragments catalogued in SSN as of January 2013, including 1968-081J, K, L, M, N, P, Q, R, S, T, U, V, W, X, Y, Z, AA, AB, AC, AD, AE, and AF. Orbits of the parent object and its fragments are back propagated to the breakup epoch of 1968-081E, and then a probable breakup point for each fragment is estimated by conducting a close approach analysis between the parent object and each fragment. The orbit propagation adopts special perturbation theories including perturbation forces by non-spherical part of the Earth gravity (by applying EGM96 to the 8th order), third bodies (the Sun and the Moon), and SRP. A/m of 0.01 $m^2$/kg is assumed for each object. Figure 5.1 shows an example of the close approach between the parent object and a fragment. It is demonstrated that the extremum-seeking algorithm is capable of finding the global minimum of the distance between the parent object and the fragment.

In this section, $\Delta V$ vector components of each breakup fragment are discussed in terms of the satellite coordinate system $NTW$ (Vallado, 2001). Figure 5.2 schematically illustrates the relation between a parent object and its breakup fragment in the $NTW$ coordinate system. The $NTW$ coordinate system is centered at a spacecraft, where $N$ axis is on the orbital plane

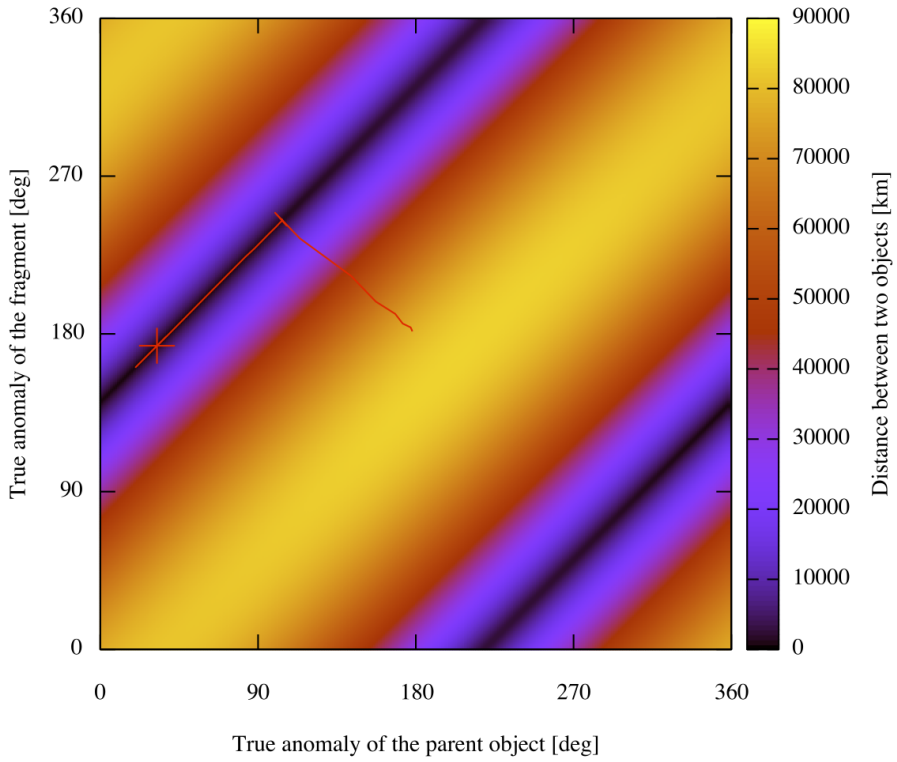


**Figure 5.1: A demonstration of the close approach between the parent object and a fragment.** - The minimum distance detected by the close approach algorithm is represented as the red point. The initial point where the close approach starts is centered in the figure. The histories of the minimum seeking is depicted as the red line.

and directs outward from the Earth (in-plane), $T$ axis points to a velocity vector direction of the spacecraft in the geocentric inertial frame (in-track), and $W$ axis is orthogonal to $N$ and $T$ axes with the right-hand rule (cross-track). The $NTW$ frame can describe the relative position and relative motion of an object with respect to the object centered at the frame. This study defines the velocity vector components of a fragment in a $NTW$ frame as the $\Delta V$ vector of the fragment.

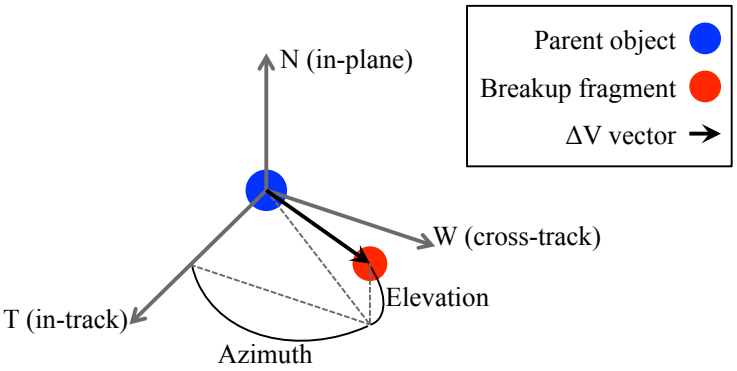


**Figure 5.2: Relation between a parent object and its breakup fragment in the $NTW$ frame.**

To begin with discussions of the estimated $\Delta V$ distribution, this study confirms that the 22 catalogued fragments are good for representing the fragmentation profile of 1968-081E. For this study, it is verified whether or not observation point selection in survey observations causes biased characteristics in the $\Delta V$ distribution of breakup fragments acquired by the observations. To evaluate this hypothesis, four quadrants are defined in the $\Delta V$ direction, i.e., azimuth-elevation, as specified in Figure 5.3. This study generates 1968-081E fragments by using the NASA standard breakup model 2001 revision with the scaling factor of 1.0, and divides them into 4 groups with respect to the quadrants. The NASA breakup model is implemented to assume that the breakup fragments are released into every direction with a uniform probability at the breakup, so that each group of the fragments represents characteristics of the quadrant. Figure 5.4 compares the predicted populations of 1968-081E fragments generated by the NASA breakup model in each $\Delta V$ quadrant at the breakup. The time-averaged distribution evaluated by 100 MC runs is applied to the OD generation and orbit propagation processes to represent each population. Fragments detection can be expected at the regions emphasized by the orange gradient, though there is no significant difference between each quadrant population other than the foot regions colored in gray. As an approximation, the actual population can

be regarded as a superposition of each quadrant population. Thus, it can be concluded that no biased characteristics in the $\Delta V$ distribution are not induced by the observation points selection in survey observations.

The evaluated $\Delta V$ distribution of the 22 fragments, which represents the fragmentation profile of the 1968-081E breakup, is shown in Figure 5.5 as an orthographic projection of the $NTW$ frame. The subframe illustrated in each plane represents the $\Delta V$ caused to the after-breakup parent object by the before-breakup parent object at the breakup epoch. Most of the fragments have $\Delta V$ smaller than 100 m/s, whereas the maximum $\Delta V$ in the data set is 195.106 m/s. It is obvious that the fragments $\Delta V$ distribution is represented by one direction and its reverse direction. What is more, $\Delta V$ vector of the parent object points to one of the directions. From these features, it can be hypothesized that the fragments were scattered from one side and its opposite side of the Transtage 1968-081E at the breakup. This hypothesis is consistent with the shape of the Transtage 1968-081E estimated by inverse photometric analysis, as reported in (Rykhlova *et al.*, 1997). Usually, isotropy is assumed for $\Delta V$ direction modeling of a breakup event, but anisotropy can be confirmed in the breakup event of 1968-081E.

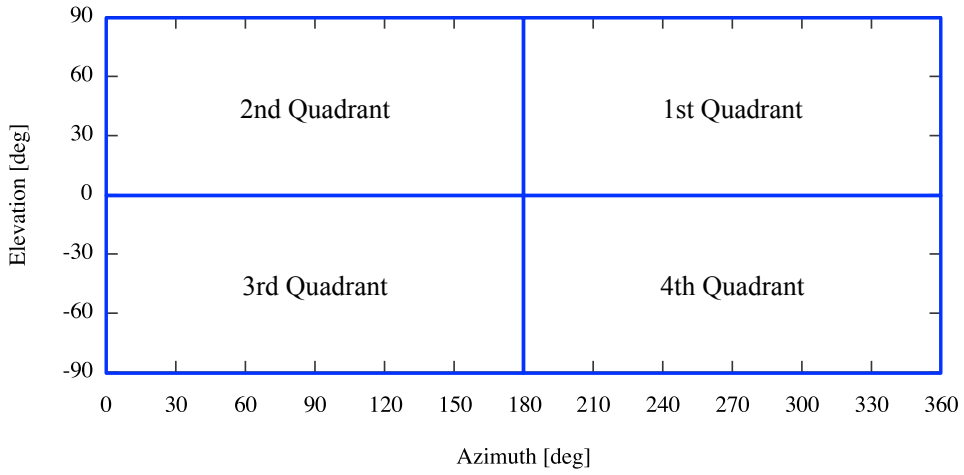


**Figure 5.3: The definition of four quadrants in the azimuth-elevation plane.**

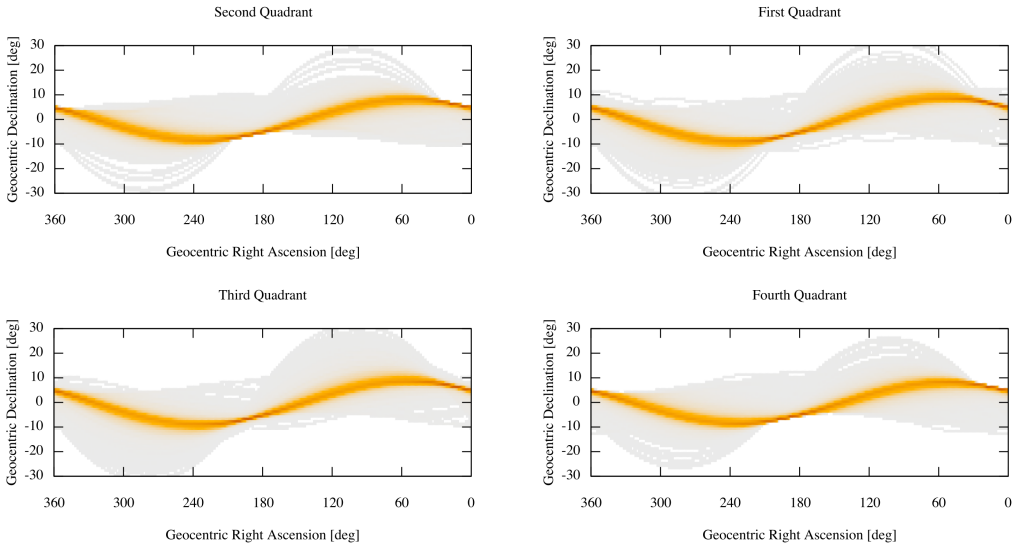


**Figure 5.4: Comparison of 1968-081E populations generated by the NASA breakup model in each $\Delta V$ quadrant.** - The epoch of each population is set to be 21 October 2011. The scaling factor of 1.0 is assumed in the OD generation. 100 MC runs are applied to represent the resulting populations.

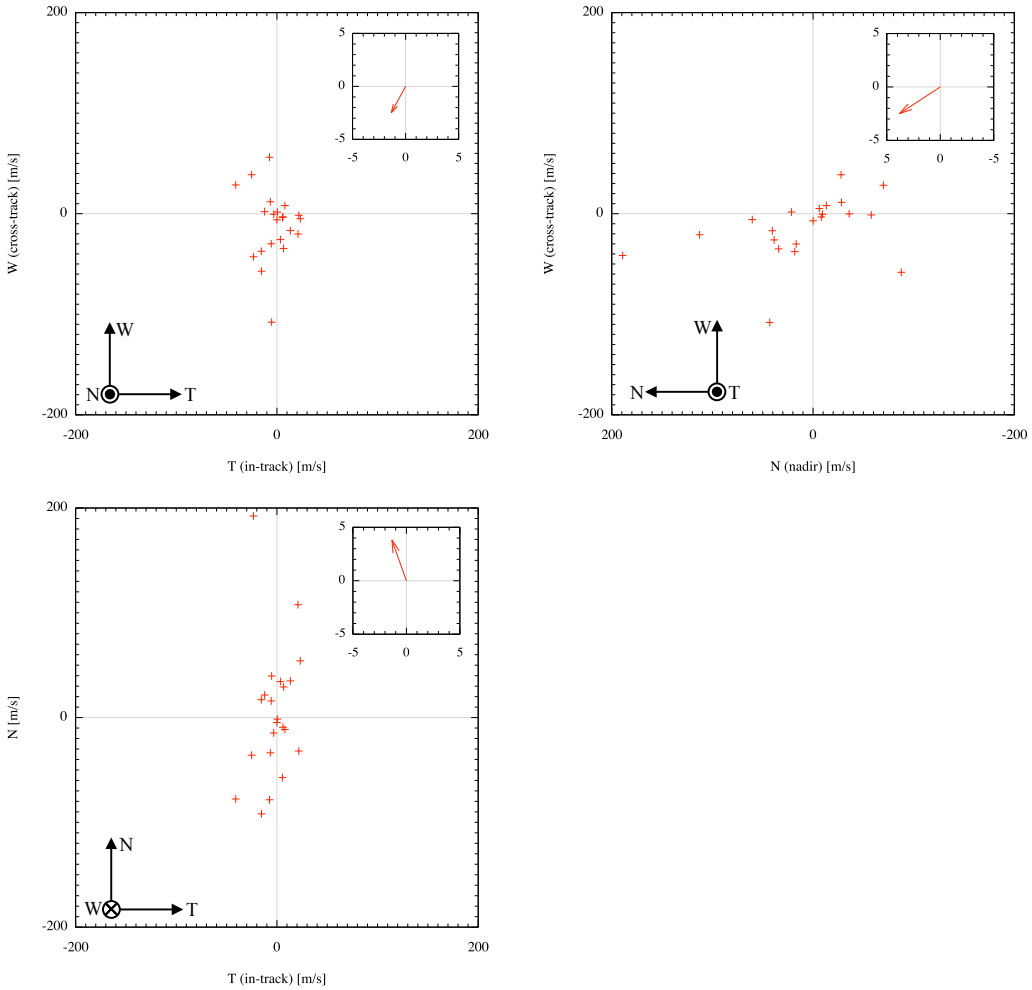


**Figure 5.5: The $\Delta V$ distribution of 1968-081E fragments in the $NTW$ frame of the parent object at the breakup epoch.** - A vector plot in the sub-frame indicates the $\Delta V$ change caused to the parent object.

## 5.2 Breakup scale assessment

This section proposes a method to assess the scaling factor of an explosion breakup by using the identified tracklets acquired through the search strategy and applies the method to the 1968-081E breakup for a demonstration. The scaling factor, introduced in the NASA standard breakup model 2001 revision (Johnson *et al.*, 2001), is estimated for the assessment. The breakup of 1968-081E is selected to demonstrate the breakup scale assessment.

In the NASA standard breakup model 2001 revision, the scaling factor ($S$) is introduced in the size distribution model for fragmentation debris generated by an explosion event as follows.

$$N(L) = 6S\,L^{-1.6} \tag{5.1}$$

where $L$ denotes a characteristic size of a fragment and $N(L)$ denotes the cumulative number of fragments whose size are larger than $L$. In this study, the size distribution, $N(L)$, is retrieved by extrapolating an observed size distribution, $N_{obs}(L)$, consisted of a tracklet data set associated with the 1968-081E breakup event. In addition, the tracklet data set must be acquired by the search survey of an inertial point where the detection rate of breakup fragments were expected to be high. Thus, this demonstration adopts the tracklets that were detected in the 2011's observation campaign at TAOS and probabilistically associated with the 1968-081E breakup, as demonstrated in Section 4.3.

The size distribution retrieval mainly consists of two steps. Figure 5.6 schematically illustrates the two steps to be addressed in the following paragraphs. After the two steps, the retrieved size distribution is fitted by Eq.(5.1) with respect to the scaling factor ($S$) by using a typical least square method.

The first step is to acquire the observed size distribution, $N_{obs}(L)$. This step requires the brightness analyses to acquire a characteristic size ($L$) of each tracklet and to select the tracklets to be accumulated into $N_{obs}$. In this study, physical object of each tracklet is modeled as the Lambert sphere assuming its albedo is 0.1, and thus a characteristic size is defined as a diameter of the sphere. The size estimation process involves range and separation angle information between the Sun, observed objects, and the observer, so that a circular orbit is estimated for each tracklet to calculate its inertial position at its observation epoch. After the size estimation, one has to define a lower limit for the size range of tracklets that is eligible to be accumulated

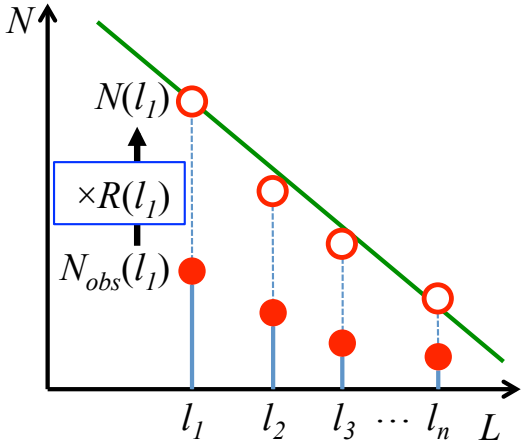


**Figure 5.6: The size distribution retrieval process.**

into the size distribution. Detection sensitivity for faint objects becomes low due to sensors capabilities and atmospheric disturbances, thus an actual sensor may miss detections of some of such faint objects that can be detected by ideal sensor having full detection sensitivity for space objects (of any types of origins). The detection sensitivity of the sensor used must be evaluated to define the eligible size regime (or the brightness regime in other words) where 100 % detection sensitivity is assured. Sensitivity analysis is, thus, conducted and sensitivity curves are acquired for each night of the data set. This study adopts the sensitivity curves of the TAOS sensor analyzed by Yanagisawa *et al.* (2012). The correlated 53 tracklets are filtered by the sensitivity curves, and it is revealed that 31 tracklets are eligible to be accumulated into $N_{obs}(L)$. It should be noted that the probability of origin association between each tracklet and 1968-081E, which is evaluated by the k-NN method in Section 4.3, must be considered in the accumulation process.

The second step retrieves the size distribution, $N(L)$, by extrapolating the observed size distribution, $N_{obs}(L)$. The observed size distribution acquired in the first step is insufficient to represent the size distribution of all the fragmentation debris in the considered size regime, because it just represents the number of fragments in a sensor's FOV during the observation. Denoting the cumulative number of tracklets at n-th observation data point as $N_{obs}(l_n)$, one can assume the following extrapolation between $N(l_n)$ and $N_{obs}(l_n)$.

$$N(l_n) = R(l_n)N_{obs}(l_n) \tag{5.2}$$

where the coefficient, $R(l_n)$, is defined by

$$R(l_n) = \frac{N_{all}(l_n)}{N_{ti}(l_n)} \tag{5.3}$$

where $N_{all}(l_n)$ represents the cumulative number of fragments ($\geq l_n$) generated by the NASA breakup model, whereas $N_{ti}(l_n)$ represents the expected number of detections of fragments ($\geq l_n$) in the sensor's FOV during the total observation period in a night. $N_{ti}(l_n)$ is evaluated by integrating Eq.(4.1) for each fragment whose trajectory exists in the FOV. In the observations at TAOS during 20-22 October 2011, the total observation period for each night is 222.9866 minutes, 277.5609 minutes, and 315.4042 minutes, respectively. To evaluate $N_{all}(l_n)$ and $N_{ti}(l_n)$, the scaling factor of 1.0 is assumed as an initial guess to generate fragments by the NASA breakup model. In this study 100 MC runs are applied to the $R(l_n)$ calculation process in combination with the accumulation process of the identified tracklets to $N_{obs}(l_n)$.

The size distribution is finally retrieved by conducting all the steps aforementioned. Figure 5.7 plots the size distribution retrieved and draws the fitting result of Eq.(5.1) in log-log scale. As a result, the scaling factor of the breakup event of 1968-081E is estimated as $2.827 \pm 0.013$. A validation of the estimation result is conducted by evaluating the summation of mass of fragmentation debris larger than 10 cm generated by the NASA breakup model applied with the estimated scaling factor. One hundred MC runs are conducted for this evaluation, and the number of fragments ($\geq$ 10 cm) generated in each MC run is 668. The total mass consumed by fragmentation debris ($\geq$ 10 cm) in the one hundred MC runs is $1659.70 \pm 383.40$ kg. It may be noted that in three cases the consumed mass exceeds the mass of the parent object. According to Johnson *et al.* (2001), on the other hand, the scaling factor of 1.0 appears to be valid for upper stages with masses of 600-1000 kg. When one assumes the mass of the Transtage as the total mass of fragments (i.e., $1659.70 \pm 383.40$ kg), the estimated scaling factor would be a possible value if the linearity between the mass at breakup and the scaling factor is assured.

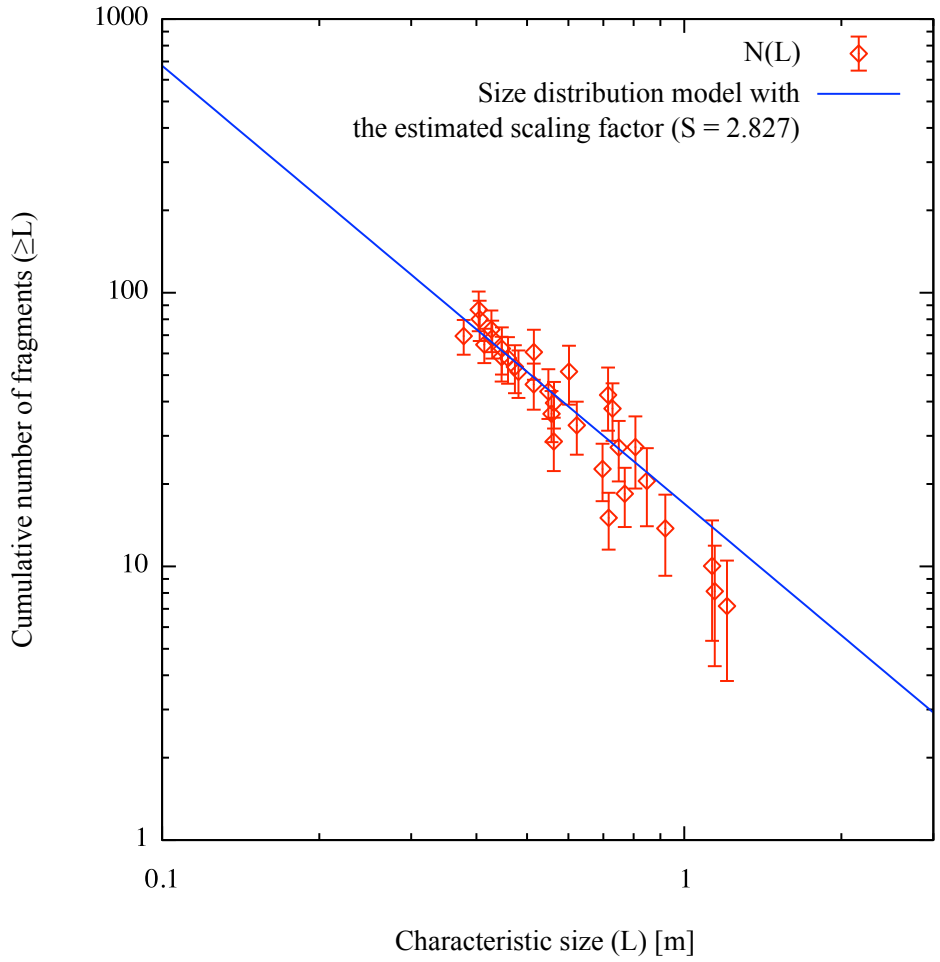


**Figure 5.7: The estimated size distribution of 1968-081E fragments.** - Each data point of $N(L)$ represents the mean value and the standard deviation of the 100 MC runs.

### 5.2.1 Revisiting observation plan

This section discusses the observation planning process based on the outcomes of the breakup scale assessment in order to realize an iterative search strategy. Figure 5.8 schematically illustrates the workflow of the iterative search strategy. The workflow of the original search strategy (Figure 2.1) is revised to the workflow of the iterative search strategy (Figure 5.8) by inserting the "breakup scale assessment" procedure after the "origin identification" procedure. The iterative search strategy utilizes the estimated breakup scales to better understand current situations of fragments of the target breakups. The better understandings can be contribute to improve accuracy and efficiency of predictive analyses, observation, detection, origin identification, and characterization of search targets.

This section evaluates the population of 1968-081E fragments by using the estimated scaling factor. The 1968-081E fragments population, in terms of the time-integrated distribution, is predicted by using Eq.(4.1). In Figure 5.9 the predicted populations are compared between the scaling factor of 1.0 as an initial guess and the estimated scaling factor of 2.827. Here should be noted that all conditions to evaluate the both populations are same, except for the scaling factor. In the OD generation process, thirty centimeter or larger fragments, whose tracklets can be detected by small aperture telescopes, are considered. In the population prediction process, a total observation period of 4.0 hours is assumed. Same color map is applied to compare the both populations on an equal footing as visualized in Figure 5.9.

High population densities are appeared in the same regions between the initial guess population and the estimated population. The pinch point shaped at the breakup point at the breakup epoch, of which conditions are same between the both populations, results in forming the high-density regions. An observation point, thus, would remain same if the scaling factor is estimated. However, areas where the time integrated number, i.e., an expected detection number, exceeds 1.0 is not consistent between the initial guess population and the estimated population. Such difference between the populations may affect the probabilistic assessments for origin identification of tracklets. An observer who plans to search for fragmentation debris of breakup events other than the 1968-081E may want to select an observation point where influence of the population of 1968-081E fragments is low or can be ignored. In this case, thus, an observation point to be selected may be altered by whether the observer knows the revised scaling factor.

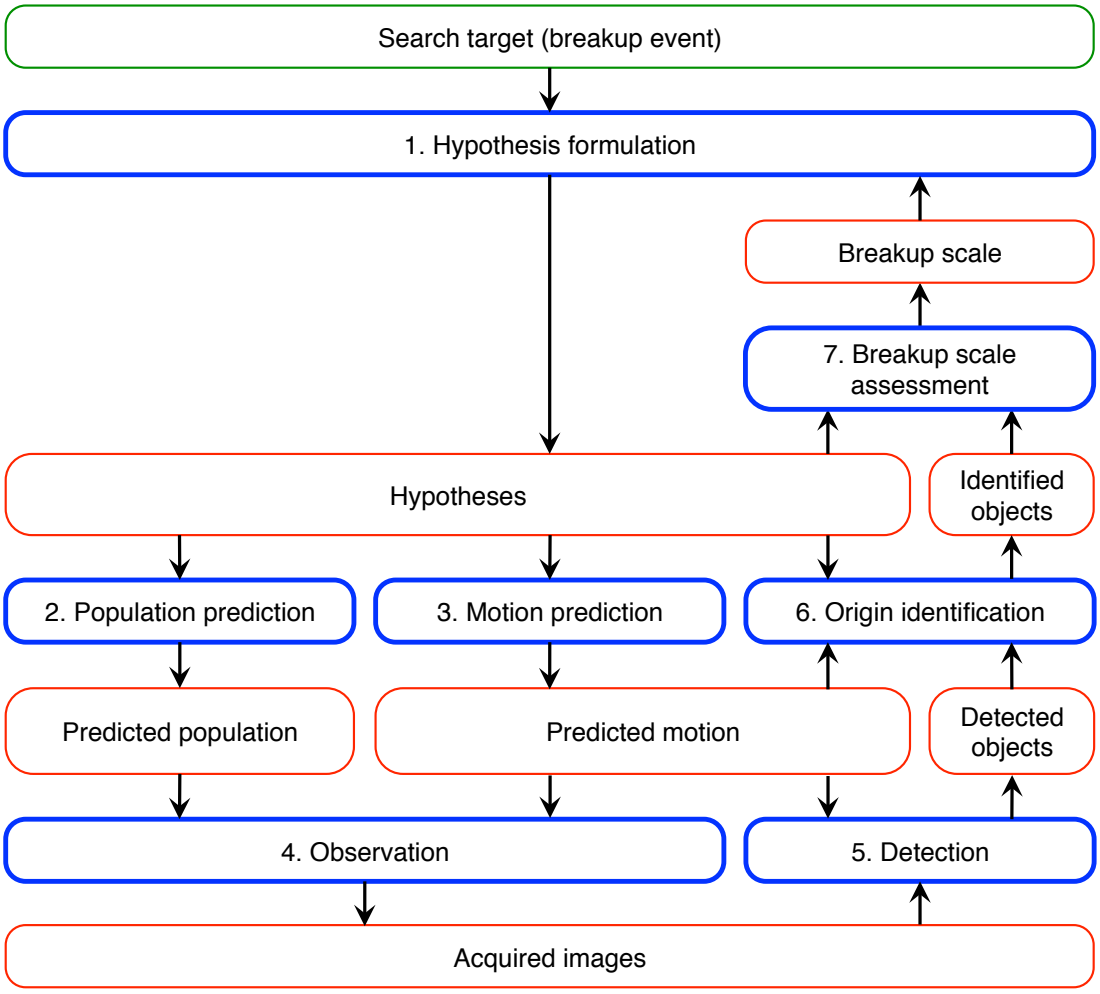


**Figure 5.8: The iterative search strategy.**

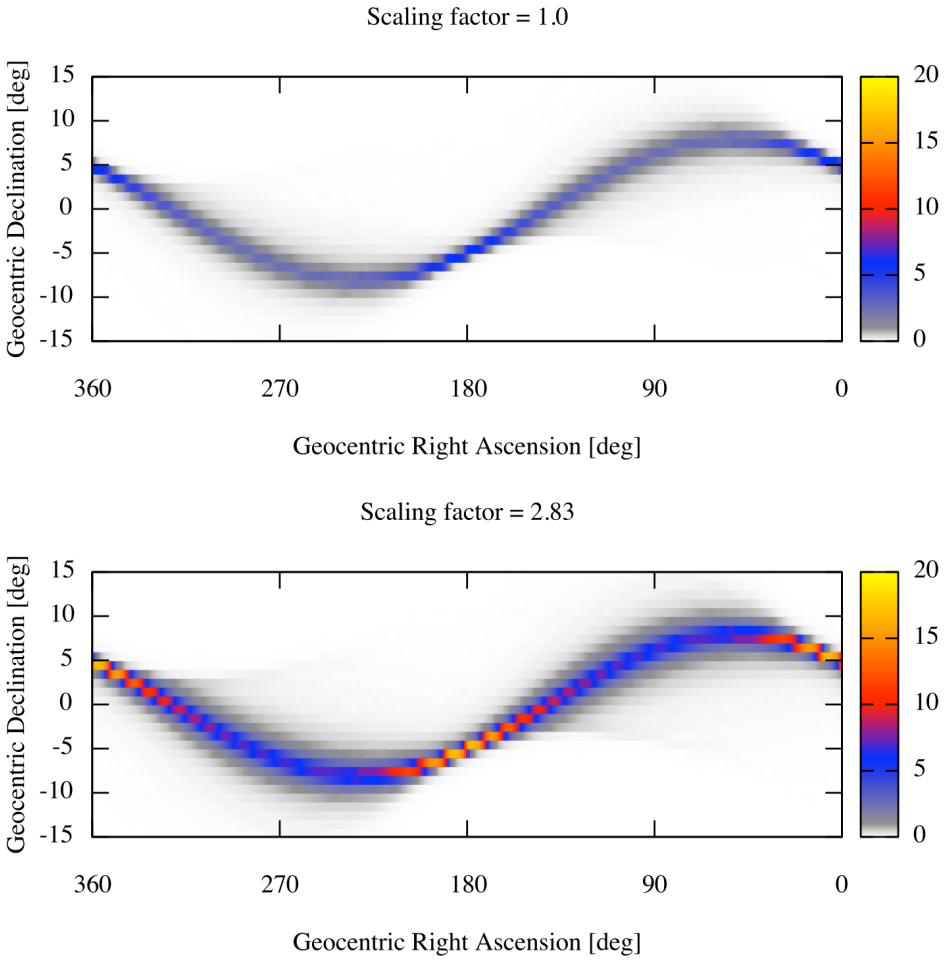


**Figure 5.9: Predicted populations of 1968-081E fragments (≥ 30cm) as of 12 March 2013.** - Top figure assumes the scaling factor of 1.0 as an initial guess and the lower figure assumes the estimated scaling factor of 2.827. A size of a bin is 1° by 1° in the both populations.

### 5.2.2 Iterative method for breakup scale assessment

This section verifies whether or not one can conduct the breakup scale assessment by an iteration process in order to realize the iterative search strategy. The breakup scale assessment requires the outcomes of the hypothesis formulation of target breakups and the probabilistic origin identification of detected tracklets. In the workflow of the iterative search strategy (Figure 5.8), therefore, this section demonstrates iterations over the sequence between the procedure 1 "hypothesis formulation", the procedure 3 "motion prediction", the procedure 6 "origin identification", and the procedure 7 "breakup scale assessment". For the verification, this demonstration adopts the tracklet data set evaluated in Section 4.3 and tracks estimated scaling factors of the multiple targets (i.e., the twelve breakups in this case) at each iteration to confirm their convergence.

There are some tips to properly conduct the breakup scale assessment procedure in the iterative process. When integrating a tracklet into $N_{obs}(L)$, one must consider the probability of origin association between the tracklet and the multiple breakups. In addition, the actual detection number is a positive integer value, so that this situation should be considered in evaluating Eq.(5.2) to avoid unnecessary divergence of estimated scaling factors. The Poisson process can be applied to the theory for $N_{ti}$ calculation. One should evaluate $N_{ti}$ by assuming it as the mean value of a Poissons probability density function. This demonstration takes the floor integer value of $N_{ti}$ as an approximation. In some cases, $N_{ti}$ may become zero which makes $N(L)$ infinite value. From such a zero value, one cannot guess a real situation, i.e., $N(L)$, so that such cases can be avoided for the $N(L)$ calculation if they happen.

As a result of the demonstration of iterations over the sequence aforementioned, the scaling factors of the breakup events of 1968-081E and 1967-066G are estimated. Figure 5.10 shows the degree of convergence of the scaling factors of 1968-081E and 1967-066G against iteration numbers. The scaling factors begin converged at the 3rd iteration. Degree of convergence of each scaling factor is 0.1. It is verified that one can conduct the iteration method for the breakup scale assessment for the iterative search strategy.

The scaling factors of 1968-081E and 1967-066G at the final iteration result are 3.8 and 0.7, respectively. The scaling factors of the other breakups are indeterminable from the TAOS data set because the number of their trajectories were expected to be quite small value in the FOV as shown in Figure 4.6. To estimate their scaling factors, one should select observation

points where a sufficient number of detections are expected for target breakup events. Additional observations at a variety of observation points would contribute to verify and improve the iterative breakup scale assessment. It would be also important to adopt a large aperture telescope or a high sensitivity detection algorithm into the iterative search strategy to improve the sensitivity limit to increase valid data points in a tracklet data set.

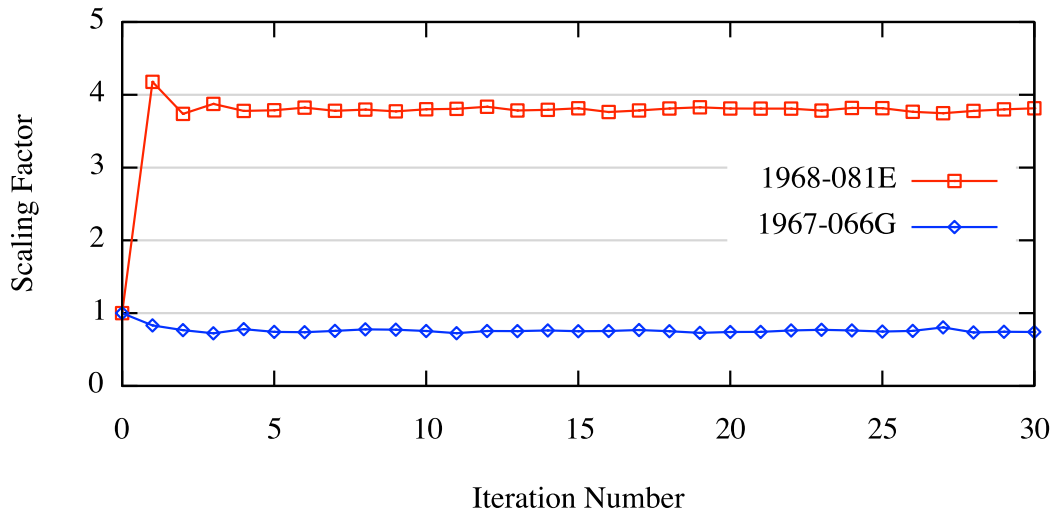


**Figure 5.10: Scaling factors estimated in the iteration method.**

## 5.3 Summary

This chapter proposed and demonstrated practical methods to estimate initial states of fragmentation debris at breakup for better understanding of current OD situations. The proposed methods applied the OD generation and orbit propagation techniques to assess the fragmentation profile and the scale of breakups in the geostationary region. The breakup of the Titan 3C Transtage (1968-081E) was selected for demonstration of the proposed methods.

In the fragmentation profile assessment, the $\Delta V$ distribution of 1968-081E fragments were estimated by using an orbital data set of 1968-081E fragments in the SSN catalogue, which was good for representing the fragmentation profile. A symmetrical feature was confirmed in the $\Delta V$ distribution of the fragmentation debris. It could be concluded that the parent object released its fragments into one direction and its reverse direction at the breakup.

In the breakup scale assessment, a tracklet data set associated with 1968-081E fragments was adopted for the evaluation. A size distribution of 1968-081E fragments was retrieved from the tracklet data set and was fitted to the size distribution model of the NASA standard breakup model 2001 revision. Finally, the scaling factor of 2.827 was estimated for the breakup event of 1968-081E, in which it was inferred that the parent object experienced a major explosion.

Finally, the iterative search strategy, which applied the outcomes of the breakup scale assessment, was proposed for future research and development. This chapter verified its fundamental capabilities in two aspects.

First, the estimated scaling factor was applied to revisit observation plans for 1968-081E fragments. The 1968-081E fragments populations were compared between the estimated scaling factor and the initial guess. It was revealed that an observation plan targeting 1968-081E fragments would remain same if the estimation was conducted. On the other hand, an observation plan targeting fragments of other breakups would be affected by whether or not the estimation was conducted because the population of 1968-081E fragments might influence probabilistic assessments for origin identification of the observation target.

Second, the iterative method for the scaling factor estimation was proposed and demonstrated. It was confirmed that the estimated scaling factors were converged by applying several nights of observation data set associated with target breakup events. The proposed method showed a conservative behavior in the scaling factor estimation: it returned indeterminable results for breakup events whose probability of detections were low in the observation region of the data set, whereas it returned converged results for breakup events whose probability of detections were high.

# 6

# Unconfirmed event identification

A search for fragmentation debris caused by an unconfirmed breakup of a spacecraft will help in identifying such breakups and to get a better understanding of the current orbital debris situation. This chapter verifies the possibility to conduct the planning of an effective optical survey of fragmentation debris caused by an unconfirmed breakup in the geostationary region.

A clue to a breakup of Earth orbiting spacecraft can be found in archived orbital history as an orbital anomaly. Indeed, some upper-stages and communication satellites inserted into the geostationary region have experienced such orbital anomalies as mentioned by several researchers, e.g., Johnson (2001); Oswald (2008); Pensa *et al.* (1996); Rykhlova *et al.* (1997). Figure 6.1 shows an interesting example of an orbital anomaly of the upper-stage Titan Transtage (1967-066G) found in the SSN catalog. Data records of semi-major axis before and after the anomaly show a disconnected leap with a time gap of over twenty days, and the orbital change resulted from the disconnected leap remains permanent after the anomaly. This semi-major axis leap is equivalent to a delta-velocity of approximately 10 m/s. The Transtage 1968-081E, whose breakup was serendipitously observed by the Maui GEODESS telescope, has also experienced a similar level of orbital change at its breakup.

In addition to 1967-066G and 1968-081E, several Transtages have experienced orbital anomalies that might be associated with breakups; for example, Johnson (2001) discussed orbital anomalies of 1966-053J, 1973-100D, and 1978-113D, and Oswald (2008) assessed orbital anomalies of 1966-053J, 1973-040B, 1975-118C, and 1979-053C might be associated with breakups.

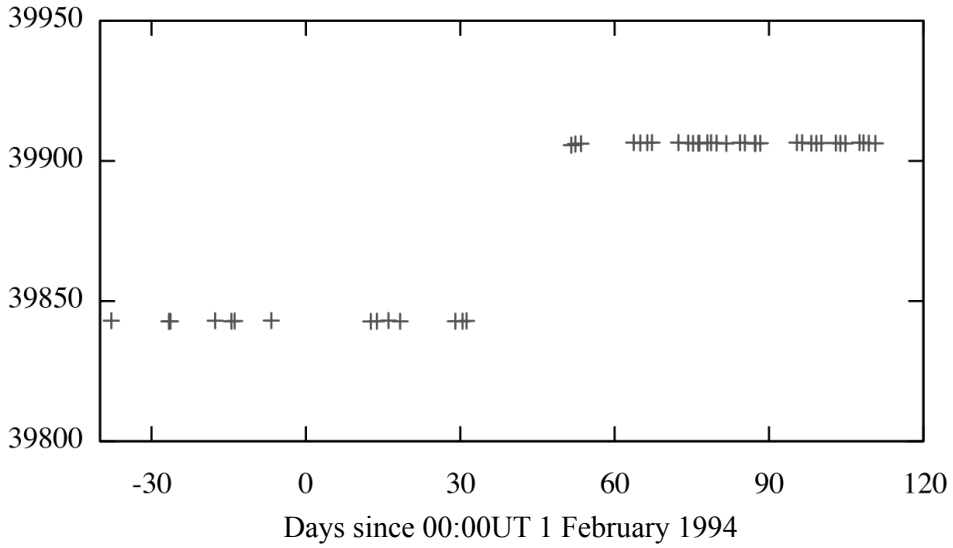


**Figure 6.1: An orbital anomaly of 1967-066G archived in the SSN catalog**

The observation planning approach for searching possible fragments is introduced in this chapter and it consists of two steps. The first step hypothesizes that an object having an orbital anomaly experienced an explosive breakup during the anomaly period. The second step predicts populations of the possible fragments in the celestial sphere at observation epochs. This study selects the orbital anomaly of 1967-066G, depicted in Figure 6.1, as a test case for the hypothesis formulation of the proposed approach. To assess how and when observation planning can be conducted, long-term behaviors of the population of 1967-066G fragments will be discussed after the hypothesis formulation. The observation planning approach proposed is applicable to the search survey step in an observation campaign. Candidates of the possible fragments can be detected in the survey regions specified by the observation planning if the hypothesis is true. After the detections, follow-up observations will help to further investigate associations between the selected orbital anomaly and the hypothesized breakup.

This chapter also conducts an optical survey of the possible breakup fragments of the US Titan 3C Transtage 1967-066G. Origins of detected UCTs will be assessed by applying the deterministic origin identification method summarized in Section 3.4.

## 6.1 Hypothesis formulation

To prepare the numerical prediction data of 1967-066G fragments for the population assessment in the following section, this section describes approaches for numerical generation of possible fragments and their orbit propagation. When looking into the data records before and after the orbital anomaly of 1967-066G, it can be hypothesized that a breakup happened between 05:09:09.14UT 1 February 1994 and 14:01:38.30UT 21 February 1994. Sixty cases of the breakup epoch are randomly selected from this possible breakup period. In each MC run, orbital elements from the 1967-066G at the start epoch of the orbital anomaly (specified in Table. 6.1) are propagated till the randomly selected breakup epoch to simulate the proper breakup position.

**Table 6.1:** Orbital elements of 1967-066G at the start epoch

| Keyword | Parameter |
|---|---|
| Epoch | 05:09:09.137UT 1 Feb. 1994 |
| Semi-major axis | 39841.866km |
| Eccentricity | 0.00535 |
| Inclination | 11.665° |
| Right ascension of the ascending node | 25.584° |
| Argument of perigee | 25.370° |
| Mean anomaly | 101.179° |

After the parent object arrangement, the NASA breakup model 2001 revision (Johnson *et al.*, 2001) is applied to generate fragmentation debris of 1967-066G. The scaling factor is assumed to be 1.0 for the initial guess. With the scaling factor of 1.0, the NASA breakup model generates 238 fragments larger than 10 cm.

Orbit propagation period for the generated fragments is set to be 54 years, accounting for perturbation period of typical objects in the geostationary region. Thirty days interval is applied to generate snapshots during the 54 years orbit propagation period to assess how the breakup epoch uncertainty affects the resulting population. The general perturbation theory including perturbation forces by the $J_2$ term (zonal harmonics) and third bodies (the Sun and the Moon) is applied to orbit propagation of fragments. Perturbation forces by the $J_{22}$ term (sectorial harmonics) and SRP are not considered in this study to simplify discussions because they affect long-term behaviors of group of fragments in the geostationary region to a negligible

degree. Hanada & Yasaka (2005), for example, has confirmed that only 9 fragments out of approximately 240 fragments, with a size of down to 10 cm in diameter, generated from a parent object at the nominal geostationary altitude might get trapped into the libration region due the $J_{22}$ perturbation. A/m is a dominant parameter to determine the magnitude of SRP acting on a space object. Usually smaller fragments have higher A/m, though it is also confirmed in this preliminary study that SRP of even the sub-meter sized fragments does not strongly interfere with the long-term behavior of a group of fragments.

## 6.2 Long-term behavior of breakup fragments

This section assesses long-term behaviors of the 1967-066G fragments population. The definition applied to the population in this study is the time-averaged distribution of fragments in the gridded celestial sphere whose coordinate is defined by geocentric right ascension ($\alpha$), and geocentric declination ($\delta$), as introduced in Section 2.2.1. This study defines each bin size as 1° by 1° to assume a typical telescope's FOV used for debris surveys. This population definition is appropriate to assess suitable observation points where the fragments are most likely to be detected.

Fragmentation debris of a single breakup form two dense regions at phase positions opposite one another as demonstrated in Section 2.2.1. One of these dense regions is formed at the pinch point where an orbital plane change is occurred to each fragment at breakup. Figures 6.2 and 6.3 represents how the breakup epoch uncertainty affects the population prediction of 1967-066G fragments. A left-hand snapshot shows the cumulative population of all 60 MC runs, and a right-hand snapshot indicates the distribution of the densest bins, where most of the fragments will be, extracted from aforementioned two dense regions formed by each breakup case. Right after the breakup, the dense region is located along the parent objects trajectory because the pinch point is different from each breakup case. In this case, the true dense regions cannot be specified.

The situation is dramatically changed after the third snapshots; two dense regions get formed as a result of orbit perturbations. Trajectories of fragmentation debris of one breakup in the geostationary region get converged into two regions even if there is a breakup epoch uncertainty of nearly three weeks. To discuss the convergence feature in detail, Figure 6.4 illustrates the evolution of the densest bins of each breakup case that is shown in the right-hand

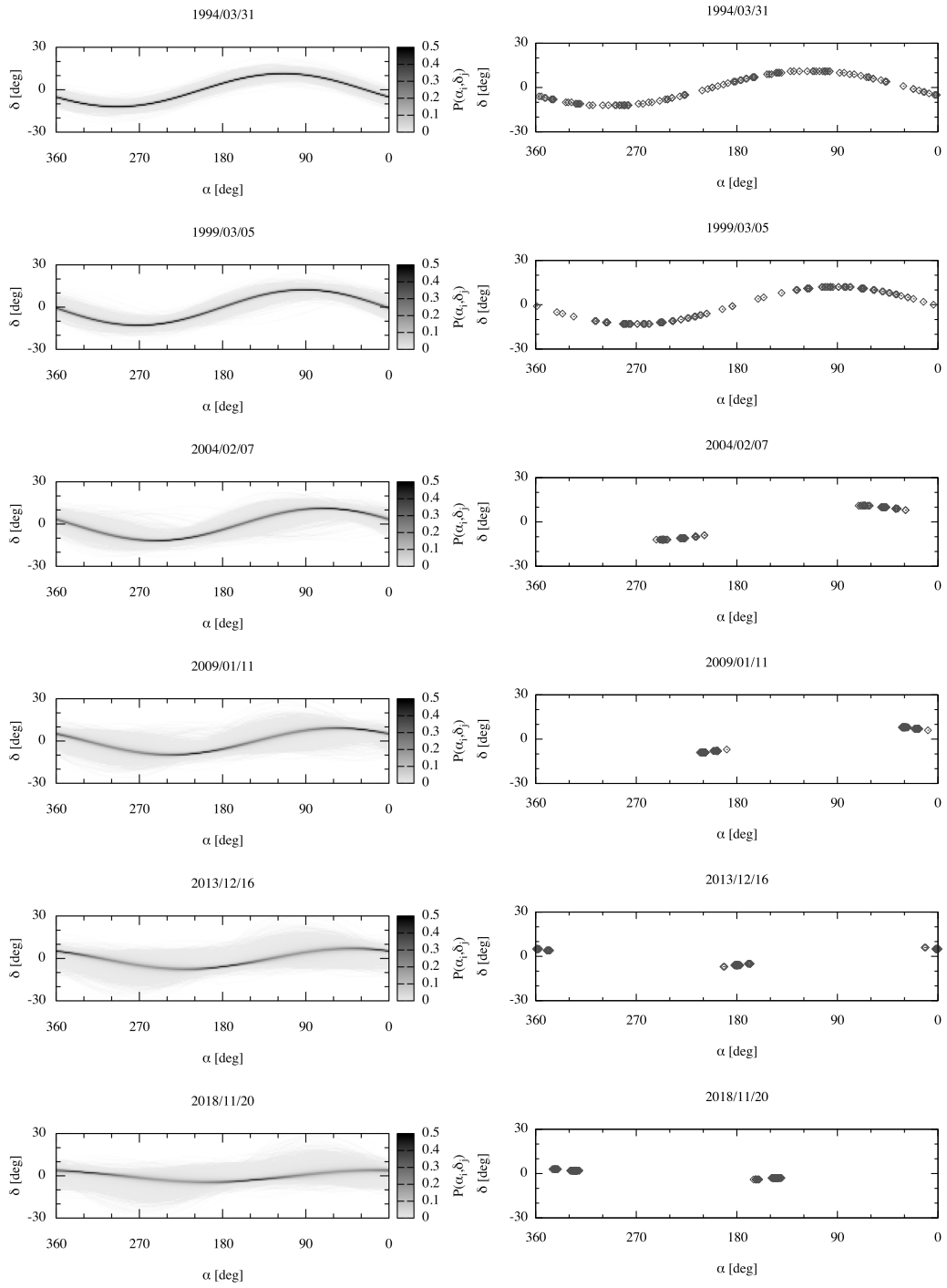


**Figure 6.2: Populations of 1967-066G fragments evaluated from 54 years propagations with 60 MC runs. (1994-2018)** - Cumulative distributions of each MC run are shown in the right hand, and the densest bins in the each snapshot of each MC run are shown in the right hand.

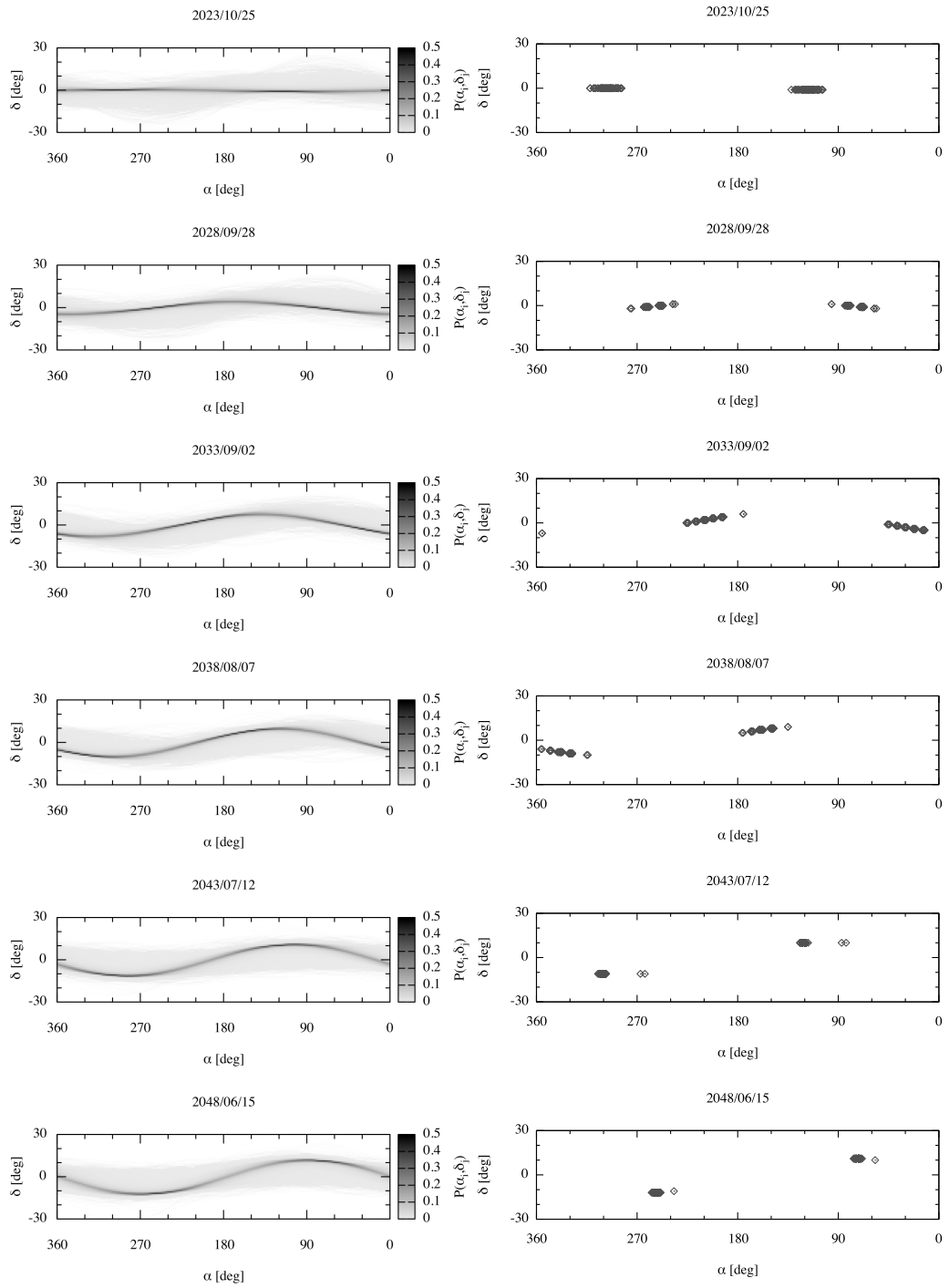


**Figure 6.3: Populations of 1967-066G fragments evaluated from 54 years propagations with 60 MC runs. (2023-2048)** - Cumulative distributions of each MC run are shown in the right hand, and the densest bins in the each snapshot of each MC run are shown in the right hand.

of Figures 6.2 and 6.3. In this case, the densest bins converge approximately 3500 days, i.e., 9.5 years, after the epoch in Figure 6.4 (00:00UT 31 March 1994). Figure 6.4 also supports the presence of the dense region motion that can be confirmed in Figures 6.2 and 6.3. The period of this motion will be consistent with approximately the major perturbation period in the geostationary region (approximately 54 years). The converged region gets wider especially after the fragments population reaches 0° inclination around 2030, though still keeps its form. Once the fragments population gets the highest inclination again around 2045, the converged region gets narrower again. It should be noted that outliers of the densest bins exist in several breakup cases, but even in this case some fragments are expected to be detected at the dense regions predicted in Figures 6.2 and 6.3 because both outlier's populations and others are aligned with each other. These assessments conclude that effective observation points can be specified even if there is uncertainty in the breakup epoch.

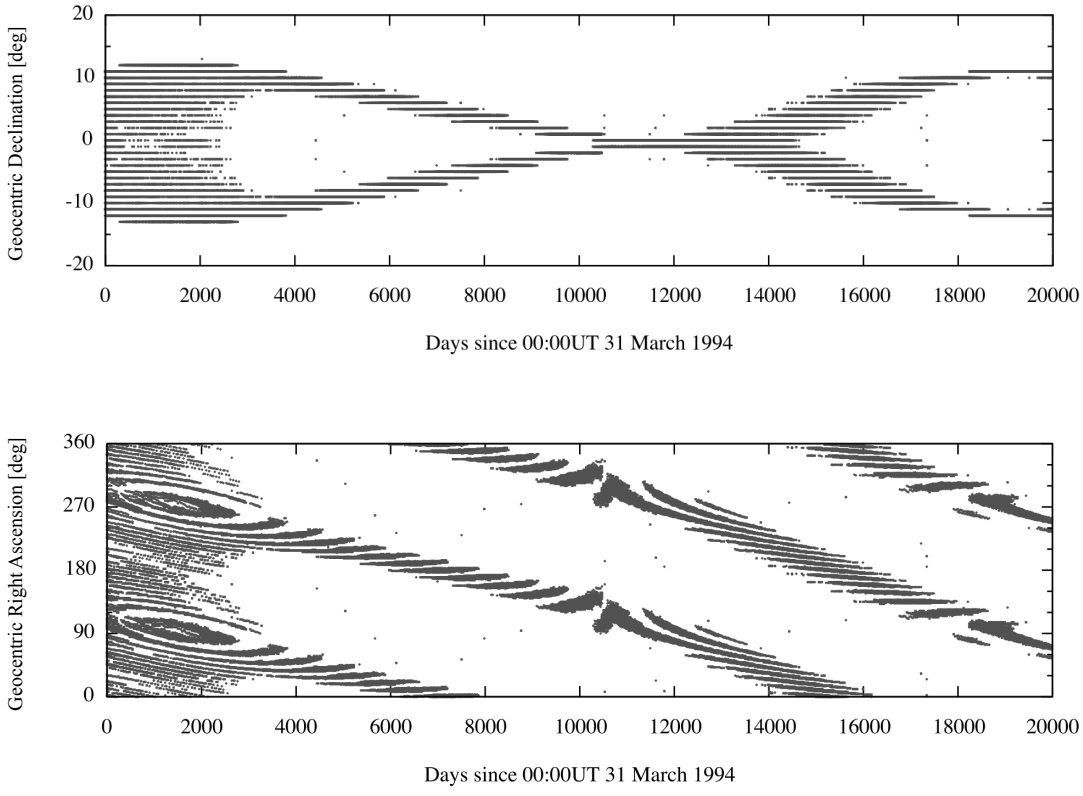


**Figure 6.4: Transitions of the densest bins of 1967-066G fragments population at each MC run.**

It is also important to confirm whether or not a sufficient number of detections are expected

at the dense regions of 1967-066G fragments during observations if the breakup hypotheses are true. Sensors should be oriented at a single inertial point for a long period (e.g., the order of hours per a night) in the search for uncatalogued debris because their temporal positions are unknown as is applied to 1967-066G fragments. Thus, the expected number of detections of fragments to be searched during an observation period is evaluated by using Eq.(4.1). This study takes for example the fifth population snapshot in Figure 6.2 (as of 16 December 2013) to evaluate the expected number of detections of the fragments whose trajectories exist in the densest bin at (180°, -6°). The observation period of six hours is assumed to evaluate the effectiveness, whereas other calculation conditions (i.e., the scaling factor of 1.0 and the FOV of 1° by 1°) are the same as described in Section 6.1. On these assumptions, the expected number of detections of 1967-066G fragments during six hours becomes 47.92 ± 6.90, in terms of nominal value ± standard deviation, resulted from 60 MC runs. The nominal value is at the same level as the expected number of detections of 1968-081E fragments that has been evaluated in Section 4.2.3. Due to the breakup epoch uncertainty, the standard deviation becomes slightly larger, although value still within a feasible range. A sufficient number of detections, thus, can be expected for breakup fragments even if there is the uncertainty in the breakup epoch.

## 6.3 Hypothesis verification

This section verifies the hypotheses formulated in Section 6.1 by conducting an optical survey of the possible fragments of 1967-066G. The objective of the optical survey is to detect the possible fragments and then conduct follow-up observations for precise orbit determination. Once the orbital parameters of the possible fragments are retrieved, one can verify whether or not the origins belong to 1967-066G by the deterministic origin identification method summarized in Section 3.4. The deterministic origin identification method assesses whether or not a detected fragment is associated with multiple features of a breakup: the motion vector features and the orbital plane features. The motion vector feature can be confirmed at an inertial point where the large number of the fragments will pass through. The orbital plane features, which consist of right ascension of ascending node ($\Omega$) and inclination ($i$), can be confirmed in two projection spaces: the first one consists of the orbital plane vector ($i\cos(\Omega)$, $i\sin(\Omega)$) where the fragments will form a linear distribution at the breakup epoch, and the second one is the celestial sphere, where the trajectories of the fragments of one breakup event will have a pinch

point at the breakup epoch. This section demonstrates the origin identification method to see if the possible fragments to be detected in the optical survey coincide with the features of the possible breakup of 1967-066G.

### 6.3.1 Observation planning

The observations are planned around the new moon term in February 2013 at the observatory JNO. The sensor used at the observatory is the 35-cm aperture telescope Takahashi $\epsilon$-350 equipped with the CCD camera FLI-ML23042. It should be noted that the CCD camera is replaced with the previous one used in Chapters 2-4. The sensor has a FOV of 1.41° by 1.41°, and a pixel scale of 15 μm/pixel. A readout time per one picture is less than 4 seconds.

Observation points suitable for the survey of the possible fragments of 1967-066G are selected in this section. Figure 6.5 predicts the population of the possible fragments of 1967-066G in the celestial sphere as of 10 February 2013. This population represents a time-averaged distribution of the fragments generated by the NASA standard breakup model 2001 revision (Johnson *et al.*, 2001). The hypotheses applied to the breakup event is the scaling factor of 1.0 that generates 238 fragments down to 10 cm and the two weeks uncertainties of the breakup epoch that can be confirmed in the orbital history of 1967-066G (Figure 6.1). There are two dense regions where a high probability of detections are expected if the hypotheses are true.

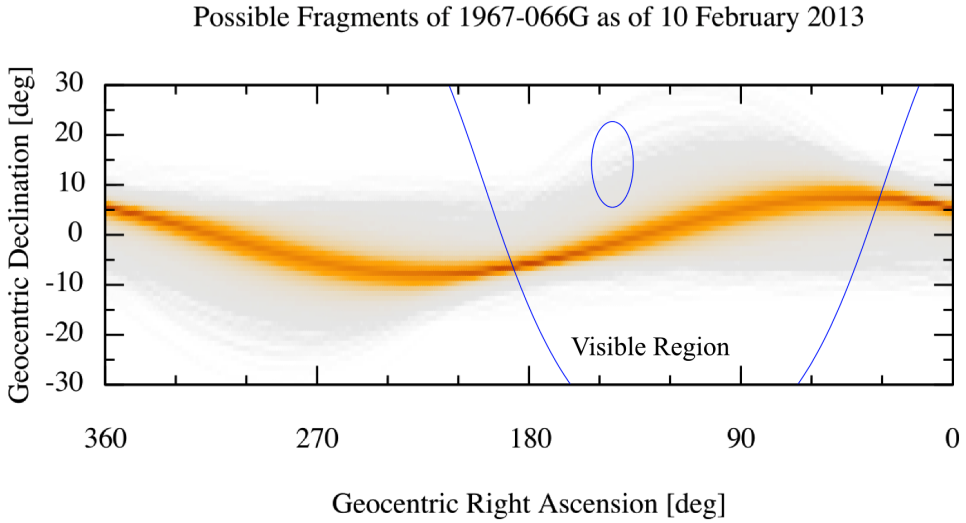


**Figure 6.5: Predicted population of the possible fragments of 1967-066G as of 10 February 2013.**

As a result, two observation points are selected to maximize a total observation period at each night by considering the region visible from the observatory during observation periods. The visible region from the observatory at the midnight is specified in Figure 6.5 for reference. The selected observation points consist of Point A and Point B, respectively. The observation coordinate for each of them is specified in Table 6.2, where $\alpha$ denotes the geocentric right ascension, $\delta$ denotes the geocentric declination, and $r$ denotes the geocentric radius. This plan observes Point A for the first half night, and Point B for the latter half night. An observation period to take one image sequences is set to 4 minutes, which results in a maximum of 166 observations per one night.

**Table 6.2:** Selected observation points

| Name | $\alpha$ [°] | $\delta$ [°] | $r$ [km] |
|---|---|---|---|
| Point A | 71.5 | 7.8 | 40000.0 |
| Point B | 180.5 | -5.5 | 40000.0 |

To assess the detection probability of 1967-066G fragments at the selected observation points, a detection rate of 1967-066G fragments in terms of the time-integrated number of fragments in the FOV per one hour is predicted. Figure 6.6 compares the predicted detection rates between the scaling factors of 0.1, 0.6, and 1.0. A data point in this figure represents a detection rate for fragments whose size is larger than a corresponding value in the horizontal axis. The nominal value and the standard deviation in the figure are evaluated based on the result of 100 MC runs of this predictive analysis. It may be noted that these MC runs consider 100 cases of breakup epochs randomly selected from the orbital anomaly period. It can be guessed from this result that the sensor will detect several 1967-066G fragments at each observation point if the target object 1967-066G experienced a major breakup whose scaling factor is around 1.0 or larger. The same type object 1968-061E experienced a major breakup so that this hypothesis may be also possible for the 1967-066G. In case 1967-066G experienced a minor breakup, the sensor might not be able to detect its fragmentation debris due to the sensor's detection sensitivity limit (approximately 17-18 magnitude, which is equivalent to 0.3-0.5 m in size).

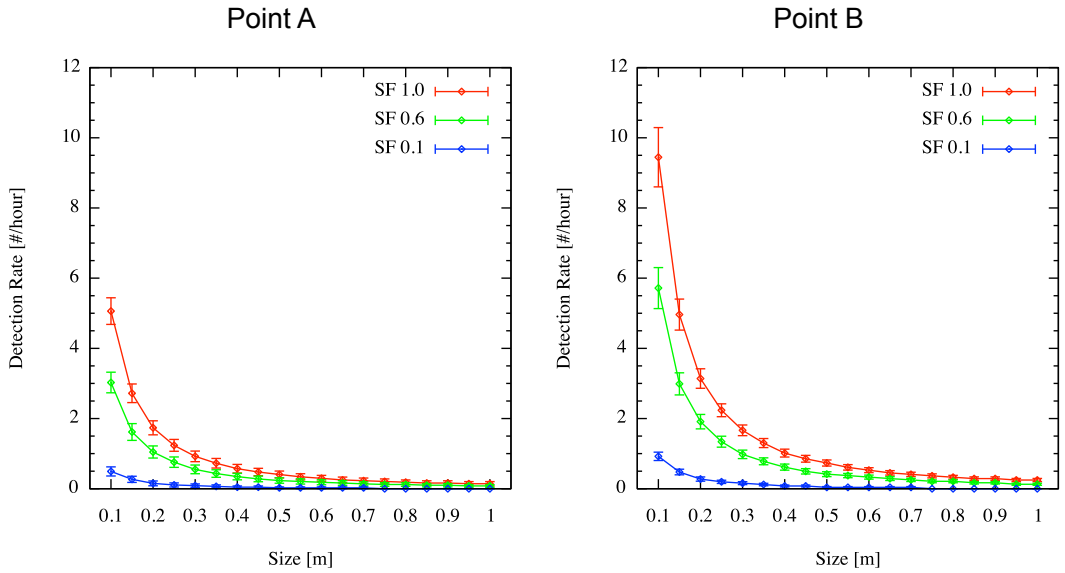


**Figure 6.6: Predicted detection rates at Point A and Point B.** - SF denotes the scaling factor.

### 6.3.2 Origin identification

As a result of the optical survey of 1967-066G fragments conducted during 08-13 February 2013 at JNO, the follow-up observations of three UCTs were performed. After the follow-up observations, these uncatalogued objects, JAXA-UCTs, were identified as JAXA-d0044, JAXA-d0045, and JAXA-d0046, respectively.

This section addresses the origin identification of JAXA-UCTs detected in the observations. First, tracklets of JAXA-UCTs are assessed in terms of the motion vector. Second, orbits of JAXA-UCTs are assessed in terms of the orbital plane vector and the pinch points, respectively. To conclude the origin of a UCT is associated with the breakup event, the UCT must be associated with every one of the breakup features in these assessments.

#### 6.3.2.1 Motion vector

The motion vector $(\Delta X, \Delta Y)$ and a size of each JAXA-UCT are evaluated in this section. An object's size is evaluated in terms of the diameter of the Lambert sphere whose albedo is 0.1. The evaluated properties of tracklets of JAXA-UCTs are summarized in the Table 6.3. In the table, "Point" denotes the observation point where the UCTs are detected, and "V-mag"

denotes the visual magnitude of a detected object. It may be noted that V magnitude of the faintest object among all objects detected is around twentieth magnitude, though the detection sensitivity is quite low for such faint objects.

**Table 6.3:** Properties of tracklets at the observation epochs

| Object ID | Point | Epoch [UT] | V-mag | $\Delta X$ [arcsec/sec] | $\Delta Y$ [arcsec/sec] | Size [m] |
|---|---|---|---|---|---|---|
| JAXA-d0044 | A | 2013/2/08 13:46:26 | 14.34 | -0.11 | 1.02 | 3.03 |
| JAXA-d0044 | A | 2013/2/13 13:14:27 | 14.35 | -0.08 | 1.00 | 3.16 |
| JAXA-d0045 | B | 2013/2/09 17:58:25 | 17.26 | 0.20 | 3.87 | 0.53 |
| JAXA-d0045 | B | 2013/2/13 17:22:26 | 16.63 | 0.20 | 3.79 | 0.70 |
| JAXA-d0046 | B | 2013/2/09 17:38:26 | 16.60 | 0.36 | 3.68 | 0.73 |
| JAXA-d0046 | B | 2013/2/13 16:30:26 | 16.64 | 0.36 | 3.67 | 0.72 |

The motion vectors of tracklets detected at Point A and Point B are assessed in Figures 6.7 and 6.8, respectively. In each figure, the detected tracklets are distinguished as CTs, UCTs, and several relevant CTs, respectively. The contours represent the possible region where the motion vectors of 1967-066G fragments will exist when assuming the scaling factor of 1.0. At Point A, JAXA-d0044 has weak relevance to 1967-066G fragments. However, the distance between JAXA-d0044 and 1968-081J is close so that they might have correlations. 1968-081J is a fragment generated by the 1968-081E's breakup. At Point B, JAXA-d0045 and JAXA-d0046 have weak relevance to 1967-066G fragments, too. Though, they are very close to the CTs, which are launched during the late 70's and the early 80's, so that they might be associated with debris of these CTs.

#### 6.3.2.2 Orbital plane vector

To conduct origin identification of JAXA-UCTs with the possible breakup event of 1967-066G, the orbits at observation epochs of JAXA-d0044, JAXA-d0045, and JAXA-d0046 are back-propagated to the 1967-066G's TLE epoch 05:09:09.14UT 1 February 1994. At the back propagated epoch, the beginning of the orbital anomaly can be confirmed in its orbital history as shown in Figure 6.1. The orbit propagation adopts special perturbation theories including perturbation forces by non-spherical part of the Earth gravity (by applying EGM96 to the 8th

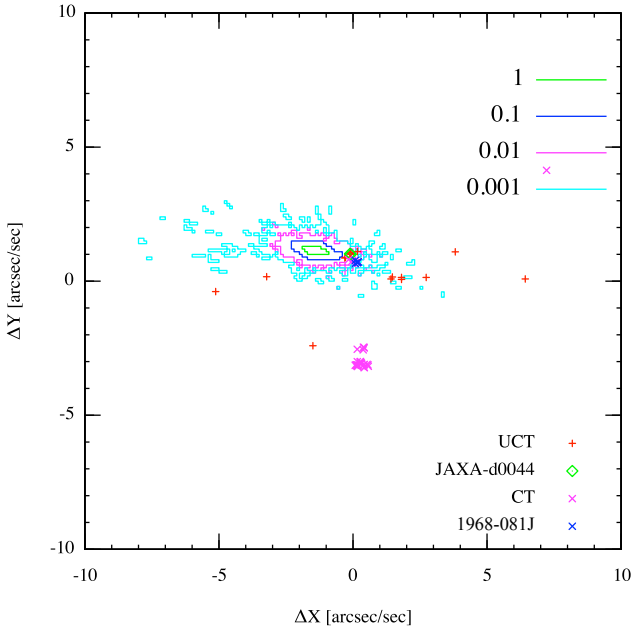


**Figure 6.7: Correlation of the motion vectors at Point A.**

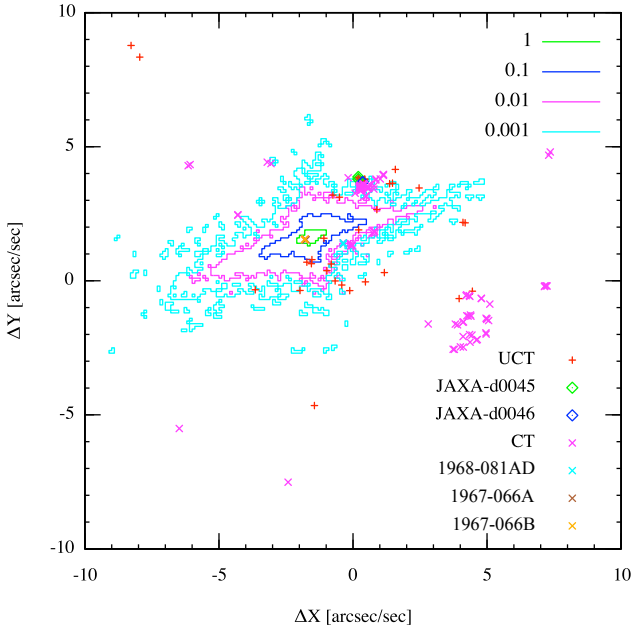


**Figure 6.8: Correlation of the motion vectors at Point B.**

**Table 6.4:** Orbits of JAXA-UCTs back-propagated to the possible breakup epoch

| Object ID | $a$ [km] | $e$ | $i$ [°] | $\Omega$ [°] | $\omega$ [°] |
|---|---|---|---|---|---|
| JAXA-d0044 | 42131.233 | 0.008 | 14.246 | 15.044 | 174.940 |
| JAXA-d0045 | 42068.045 | 0.020 | 11.611 | 38.139 | 72.782 |
| JAXA-d0046 | 41902.138 | 0.005 | 11.690 | 43.532 | 158.066 |

order), third bodies (the Sun and the Moon), and SRP. A/m of 0.01 $m^2$/kg is assumed for each object. Their orbital elements before/after the propagation are summarized in Table 6.4.

As demonstrated in Section 2.5, the orbital plane vectors ($i\cos(\Omega)$, $i\sin(\Omega)$) of fragmentation debris of a same parent object show a linear distribution at its breakup epoch. If UCTs and a possible parent object are in a line with at near its breakup epoch, the UCTs may be associated with the breakup. This study assumes that 1967-066G is the possible parent object.

The orbital plane vectors of JAXA-UCTs and 1967-066G at the beginning of the possible breakup period are shown in Figure 6.9. One has to distinguish the features of 1967-066G fragments and 1968-081E fragments because the breakup epoch of 1968-081E is only two years before the possible breakup of 1967-066G and these parent objects have similar orbital plane parameters. Thus, 1968-081E and its 22 fragments catalogued by SSN are also back-propagated to the aforementioned epoch and plotted in Figure 6.9. In the figure, JAXA-d0045, JAXA-d0046, and 1967-066G are correlated because they are in a line, whereas 1968-081E and its fragments are in another line deformed a little. These lines have slightly different inclinations, thus they can be distinguished. JAXA-d0044 is not associated with any of the lines.

As demonstrated in Section 3.3, orbits of fragmentation debris of a same parent object share a same intersection, i.e., the pinch point, at near its breakup epoch. The position of the pinch point corresponds to where the breakup occurs. One can also confirm the pinch point in the trajectories of fragments in the celestial sphere. To assess if one can confirm a pinch point between JAXA-UCTs and 1967-066G, their trajectories at the aforementioned possible breakup epoch are drawn in Figure 6.10. The trajectories of 1968-081E and its fragments are also drawn in this figure due to the same reason mentioned in the previous paragraph. In this figure, one can confirm a pinch point between JAXA-d0045, JAXA-d0046, and 1967-066G, and also another pinch point between 1968-081E and its fragments (drawn in gray color).

These pinch points are a little apart so that they can be distinguished. JAXA-d0044 is not associated with any of the intersections.

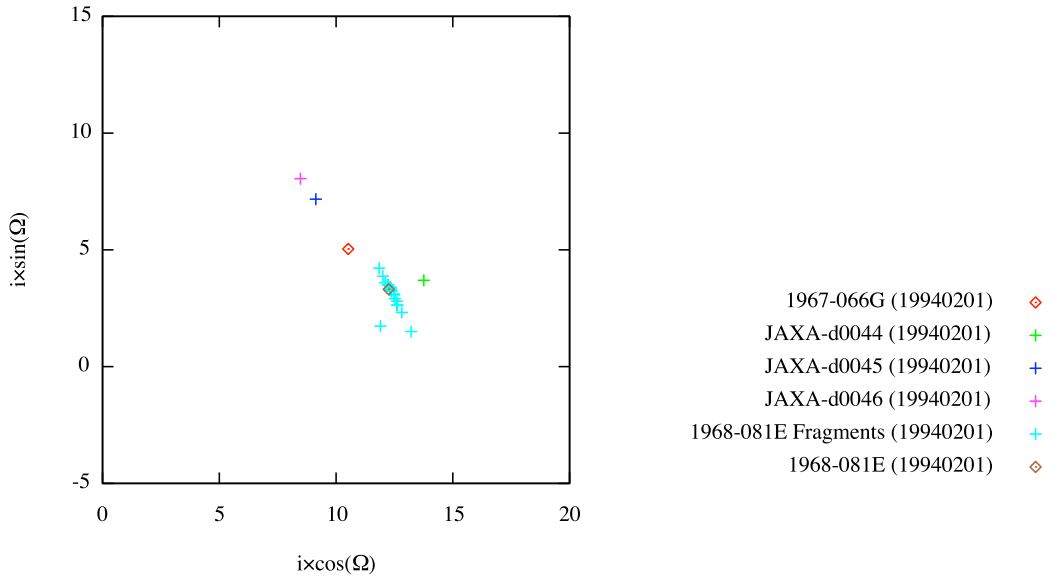


**Figure 6.9: Correlation of the orbital plane vectors.**

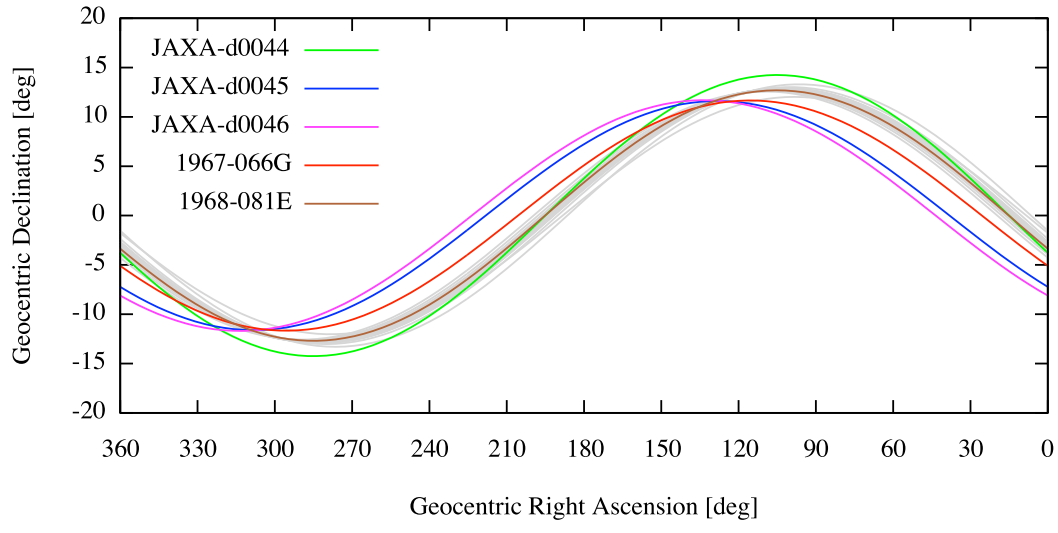


**Figure 6.10: Correlation of the pinch points.**

To further verify the pinch points, the distances between JAXA-UCTs and 1967-066G at the pinch points are evaluated by using the close approach method. The closest points between

each JAXA-UCT and 1967-066G are specified in the Earth inertial frame at the beginning of the possible breakup period of 1967-066G, and then the distance is evaluated in the satellite origin frame $NTW$ of 1967-066G. Distance between JAXA-UCTs and 1967-066G at the pinch points are calculated as 1934.701 km (JAXA-d0044), 1455.202 km (JAXA-d0045), and 2046.567 km (JAXA-d0046), respectively. It turned out that JAXA-UCTs are so far from 1967-066G at its breakup epoch that they might not have correlations even though the pinch points in the celestial sphere are correlated.

## 6.4 Summary

This chapter proposed to verify whether or not it is possible to conduct effective observation planning to search possible fragments whose parent object might have experienced a breakup in the geostationary region. To do this, this chapter formulated the hypothesis that an orbital anomaly of a satellite to be searched was associated with its breakup, and predicted the population of the possible fragments in the celestial sphere with consideration of the breakup epoch uncertainty. The orbital anomaly of 1967-066G, whose breakup possibility was mentioned by several authors, was selected as the test case to demonstrate this approach. The long-term population prediction of 1967-066G fragments was conducted to demonstrate and confirm the convergence of the dense population region approximately 10 years after the possible breakup period. It was also assessed that a sufficient number of detections of 1967-066G fragments were also expected during one night of observation with a sensor pointing at a dense region. From this result, it was specified where an observer should search in the celestial sphere to get high probability of detections of the possible fragments. Finally, it was concluded that the proposed observation planning approach was applicable for verifying the presence of unconfirmed breakup events that might have happened in the geostationary region even if there was only a possible evidence of a breakup: the orbital anomaly in archived orbital history.

As a result of the optical survey of 1967-066G fragments, it might be concluded that tracklets of JAXA-UCTs were not associated with the 1967-066G event regarding the motion vectors, however orbits of JAXA-d0045 and JAXA-d0046 were associated with the event regarding the orbital plane vectors and the pinch points of their trajectories. A breakup fragment that was generated by an event should be associated with each feature of the event, i.e., the motion vector, the orbital plane vector, and the pinch point. Moreover, results of close approach between

JAXA-UCTs and 1967-066G showed that the distances between each JAXA-UCT and 1967-066G was the order of 1000 km so that this evidence supported the false of the hypothesis that 1967-066G experienced a breakup.

Though this study surveyed the regions where the probability of detections of 1967-066G fragments were predicted to be high, the result was not quite associated with the possible breakup event of 1967-066G. Consequently, it might be possible that the breakup scale was quite small or the orbital anomaly of 1967-066G was not an evidence of its breakup. If the latter case was true, a remaining possible cause of the orbital anomaly would be the propellant venting of the Transtage as was inferred by Johnson (2001).

## 6. UNCONFIRMED EVENT IDENTIFICATION

# 7

# Conclusion

This dissertation formulated the search strategy applicable for breakup fragments in the geostationary region. Effectiveness of the search strategy was verified by theoretical and empirical confirmations.

The search strategy formulated in this dissertation was designed to devise observation planning, detection, and origin identification of breakup fragments by applying OD modeling techniques, which consisted of OD generation and orbit propagation. The OD modeling techniques were utilized to formulate hypotheses of target breakups such as orbits of target breakup fragments at breakup epochs and observation epochs. This dissertation verified that the hypotheses could be applied to population prediction, motion prediction and origin identification of target breakup fragments. In the observation planning, the population prediction enabled to specify observation points suited for searching fragments, even if there was uncertainties in the breakup epoch, and the motion prediction assisted the observation point selection in terms of improving S/N of target fragments in each image frame. In the detection, the motion prediction succeeded in reducing the computational workload of the stacking method, which was capable of detecting faint OD from image sequences. In the origin identification, it was confirmed that the origins of detected UCTs could be deterministically identified by applying the orbital plane features of fragments at breakup and also probabilistically identified by applying the motion prediction. The deterministic origin identification enabled to assess the relation between orbital anomalies and unconfirmed breakups. The probabilistic origin identification, on the other hand, enabled to characterize a target breakup by estimating its breakup scale. A combination of the probabilistic origin identification and the breakup characterization was led to propose the

iterative search strategy, which was designed to verify and improve reliabilities of hypotheses at every observation.

It was verified that the search strategy was capable of devising the observation planning, the detection, and the origin identification of target breakup, and even characterizing the target breakups by utilizing observation results acquired. This dissertation concludes that the search strategy contributed to better understand current OD situations in the geostationary region, and pave a new path to further research and development in order to resolve OD issues for sustainable space exploration.

# Appendix A

# Coordinate system

This appendix describes coordinate systems involved in the dissertation based on (Vallado, 2001).

## A.1 Geocentric equatorial coordinate system (IJK)

In the *IJK* system, its origin is at the center the Earth, the $I$ axis points towards the vernal equinox, the $J$ axis is 90° to the East in the equatorial plane, and the $K$ axis extends through the North Pole. This dissertation distinguishes the geocentric Earth-fixed (GF) coordinate system ($I_{GF}J_{GF}K$) from the *IJK* system. The $I_{GF}$ axis is fixed on the Greenwich meridian in the equatorial plane and the $J_{GF}$ is 90° to the East. The angle between the $I$ axis and the $I_{GF}$ axis can be expressed by GMST, $\theta_G$. Figure A.1 illustrates the orientation of the $I_{GF}J_{GF}K$ system with respect to the IJK system.

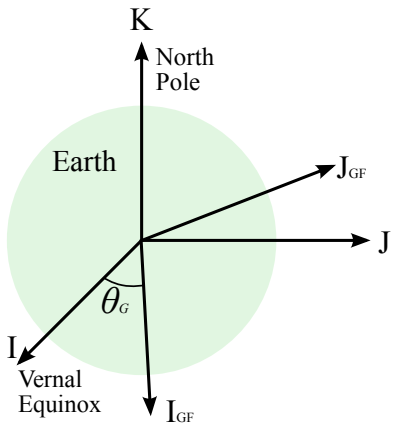


**Figure A.1: The *IJK* system and the $I_{GF}J_{GF}K$ system.**

## A.2 Classical orbital elements representation

This dissertation utilizes the classical orbital elements to represent the orbit of a satellite in the geocentric equatorial coordinate system, as illustrated in Figure A.2. The semi-major axis, $a$, defines the size of the orbit. The eccentricity, $e$, defines the shape of the orbit. The argument of perigee, $\omega$, defines the angle between the ascending node and the perigee. The inclination, $i$, defines the angle between the equatorial plane and the orbital plane. The right ascension of the ascending node, $\Omega$, defines the angle between the vernal equinox and the ascending node. The true anomaly, $f$, defines the angle between the perigee and the satellite's orbital position.

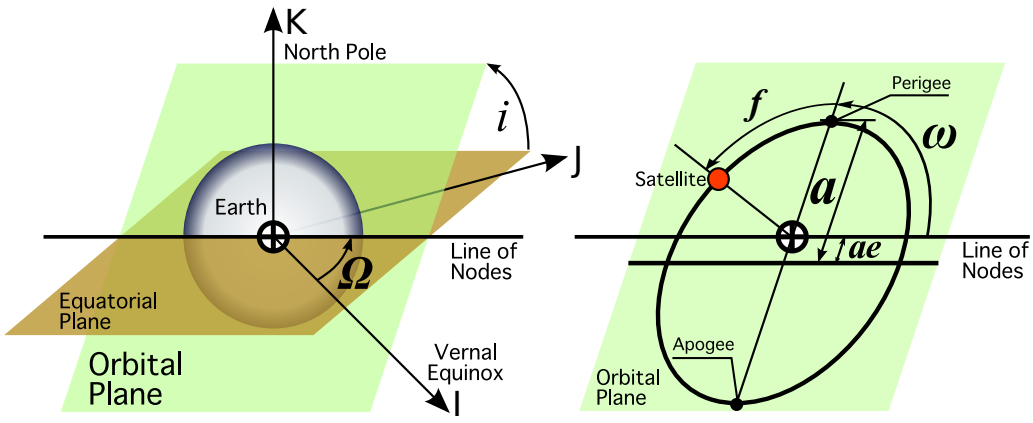


**Figure A.2: The classical orbital elements in the *IJK* system.**

The eccentric anomaly, $E$, and the mean anomaly, $M$, are also used to express the satellite's orbital position. A relation between the mean anomaly and the eccentric anomaly can be described by the Kepler's equation.

$$M = E - e \sin E \tag{A.1}$$

A geometrical relation between the eccentric anomaly and the true anomaly is defined by

$$\sin E = \frac{r \sin f}{a\sqrt{1-e^2}} \tag{A.2}$$

$$\cos E = \frac{ae + r \cos f}{a} \tag{A.3}$$

then we can obtain

$$\tan\left(\frac{f}{2}\right) = \sqrt{\frac{1+e}{1-e}}\tan\left(\frac{E}{2}\right) \tag{A.4}$$

$$\tan\left(\frac{E}{2}\right) = \sqrt{\frac{1-e}{1+e}}\tan\left(\frac{f}{2}\right) \tag{A.5}$$

## A.3 Spherical coordinate representation

Position of a satellite can be represented by the spherical coordinate with respect to a Cartesian coordinate system, thus to the *IJK* system. Figure A.3 illustrates the orientation of a satellite represented by the spherical coordinate, where $\alpha$ denotes the geocentric right ascension, $\delta$ denotes the geocentric declination, and $r$ denotes the geocentric radius.

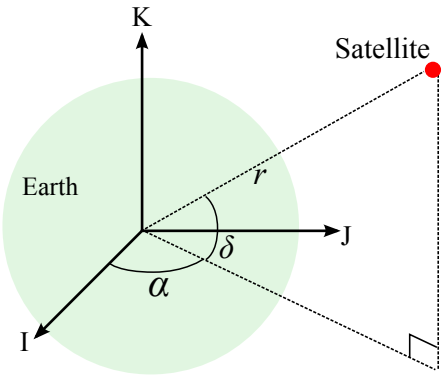


**Figure A.3: The spherical coordinate representation of a satellite's position in the *IJK* system.**

## A.4 Periforcal coordinate system (PQW)

In the *PQW* system, the fundamental plane is the satellite orbit, and the origin is at the center of the Earth. The *P* axis points towards perigee, and the *Q* axis is 90° from the P axis in the direction of satellite motion. The *W* axis is normal to the orbit. Figure A.4 illustrates the *PQW* system.

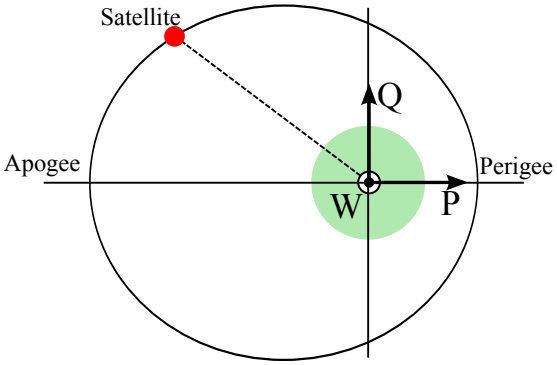


**Figure A.4: The *PQW* system.**

## A.5 Topocentric equatorial coordinate system

This system is essentially the geocentric equatorial coordinate system with the origin translated from the Earth's center to the observer. The orientation of the axes is the same as the *IJK* system. This dissertation utilizes the Topocentric earth-fixed (TF) coordinate system ($I_{TF}J_{TF}K_{TF}$) to describe states of satellites in a sensor plane. The $I_{TF}$, $J_{TF}$, and $K_{TF}$ axes are parallel to the $I_{GF}$, $J_{GF}$, and $K$ axes, respectively. Figure A.5 illustrates the orientation of the $I_{TF}J_{TF}K_{TF}$ system with respect to the $I_{GF}J_{GF}K$ system. This figure also illustrates the orientation of a satellite represented by the spherical coordinate, where $\alpha_{TF}$ denotes the topocentric earth-fixed right ascension, $\delta_{TF}$ denotes the topocentric earth-fixed declination, and $r_{TF}$ denotes the topocentric earth-fixed radius.

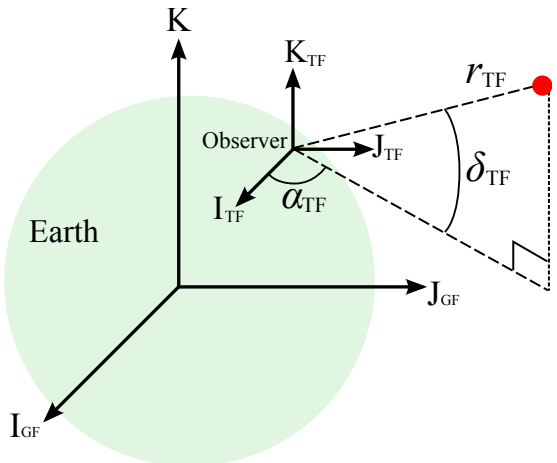


**Figure A.5: The $I_{TF}J_{TF}K_{TF}$ system and the $I_{GF}J_{GF}K$ system.**

## A.6 Satellite coordinate system (RSW and NTW)

This dissertation utilizes the two satellite coordinate systems, *RSW* and *NTW*. In the *RSW* system, its origin is centered at the satellite, the *R* axis is defined as always pointing from the Earth's center along the radius vector towards the satellite as it moves through the orbit, the *W* axis is fixed along the direction normal to the orbital plane, and the *S* axis points in the direction of the velocity vector and is perpendicular to the radius vector. In the *NTW* system, whereas, the *T* axis is tangential to the orbit and always points to the velocity vector ($\boldsymbol{v}$), the *N* axis lies in the orbital plane normal to the velocity vector, and the *W* axis is normal to the orbital plane (as in the *RSW* system). Figure A.6 illustrates the orientation of the *RSW* system and the *NTW* system.

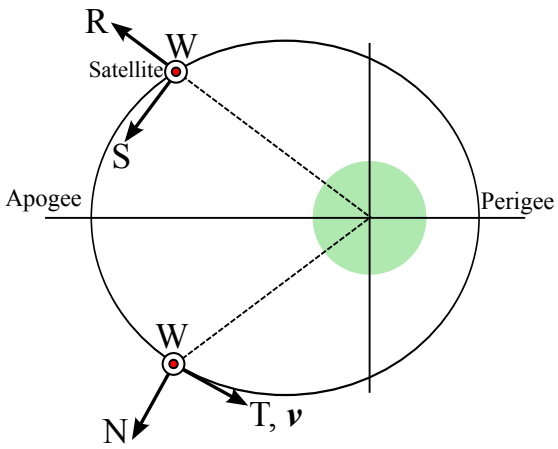


**Figure A.6: The *RSW* system and the *NTW* system.**

# Appendix B

# Coordinate transformation

This appendix describes coordinate transformations involved in the dissertation.

## B.1 Transformation in Cartesian coordinate system

The coordinate transformation from the Cartesian coordinate system A to the Cartesian coordinate system B can be described by

$$\boldsymbol{r}_B = {}^{B}[R]_A \boldsymbol{r}_A \tag{B.1}$$

where $\boldsymbol{r}$ is a position vector in each coordinate system and ${}^{B}[R]_A$ is a rotation matrix from the system A to the system B. Each rotation matrix ${}^{B}[R]_A$ appeared in the following sections forms an orthogonal set , thus, the inverse is simply the transpose. Therefore,

$$\boldsymbol{r}_A = {}^{A}[R]_B \boldsymbol{r}_B \tag{B.2}$$

$$\boldsymbol{r}_A = {}^{B}[R]_A^T \boldsymbol{r}_B \tag{B.3}$$

Following sections describe the rotational matrixes involved in each coordinate transformation.

### B.1.1 GI(IJK) and GF(IJK)

The rotation matrix to convert a vector from the geocentric inertial coordinate system (GI) to the geocentric earth-fixed coordinate system (GF) can be defined by

$${}^{GF}[R]_{GI} = \begin{bmatrix} \cos\theta_G & \sin\theta_G & 0 \\ -\sin\theta_G & \cos\theta_G & 0 \\ 0 & 0 & 1 \end{bmatrix} \tag{B.4}$$

where $\theta_G$ is GMST.

### B.1.2 IJK and NTW

Let $\boldsymbol{r}$ and $\boldsymbol{v}$ denote the position vector and the velocity vector in the *IJK* coordinate system, respectively. The rotation matrix to convert a vector from the *NTW* coordinate system to the *IJK* coordinate system can be defined by

$$^{IJK}[R]_{NTW} = \begin{bmatrix} \hat{\boldsymbol{N}} & \hat{\boldsymbol{T}} & \hat{\boldsymbol{W}} \end{bmatrix} \tag{B.5}$$

where $\hat{\boldsymbol{N}}$, $\hat{\boldsymbol{T}}$, and $\hat{\boldsymbol{W}}$ are denoted as

$$\hat{\boldsymbol{T}} = \frac{\boldsymbol{v}}{|\boldsymbol{v}|} \tag{B.6}$$

$$\hat{\boldsymbol{W}} = \frac{\boldsymbol{r} \times \boldsymbol{v}}{|\boldsymbol{r} \times \boldsymbol{v}|} \tag{B.7}$$

$$\hat{\boldsymbol{N}} = \hat{\boldsymbol{T}} \times \hat{\boldsymbol{W}} \tag{B.8}$$

### B.1.3 IJK and RSW

The rotation matrix to convert a vector from the *RSW* coordinate system to the *IJK* coordinate system can be defined by

$$^{IJK}[R]_{RSW} = \begin{bmatrix} \hat{\boldsymbol{R}} & \hat{\boldsymbol{S}} & \hat{\boldsymbol{W}} \end{bmatrix} \tag{B.9}$$

where $\hat{\boldsymbol{W}}$ is the same as Eq.(B.7). $\hat{\boldsymbol{R}}$ and $\hat{\boldsymbol{S}}$ are denoted as

$$\hat{\boldsymbol{R}} = \frac{\boldsymbol{r}}{|\boldsymbol{r}|} \tag{B.10}$$

$$\hat{\boldsymbol{S}} = \hat{\boldsymbol{W}} \times \hat{\boldsymbol{R}} \tag{B.11}$$

### B.1.4 PQW and RSW

The rotation matrix to convert a vector from the *PQW* coordinate system to the *RSW* coordinate system can be defined by

$$^{RSW}[R]_{PQW} = \begin{bmatrix} \cos f & \sin f & 0 \\ -\sin f & \cos f & 0 \\ 0 & 0 & 1 \end{bmatrix} \tag{B.12}$$

where $f$ is the true anomaly.

## B.2 Spherical coordinate representation

Spherical coordinate representations may be needed for satellites in the dissertation. The spherical coordinate consists of the right ascension $\alpha$, the declination $\delta$, and the radius $r$. The position vector $\boldsymbol{r}_c = (x, y, z)$ and the velocity vector $\boldsymbol{v}_c = (\dot{x}, \dot{y}, \dot{z})$ of a satellite in a Cartesian coordinate system can be described by

$$\boldsymbol{r}_c = \begin{Bmatrix} r\cos\delta\cos\alpha \\ r\cos\delta\sin\alpha \\ r\sin\delta \end{Bmatrix} \tag{B.13}$$

$$\boldsymbol{v}_c = \dot{\boldsymbol{r}}_c = \begin{Bmatrix} \dot{r}\cos\delta\cos\alpha - r\dot{\delta}\sin\delta\cos\alpha - r\dot{\alpha}\cos\delta\sin\alpha \\ \dot{r}\cos\delta\sin\alpha - r\dot{\delta}\sin\delta\sin\alpha + r\dot{\alpha}\cos\delta\cos\alpha \\ \dot{r}\sin\delta + r\dot{\delta}\cos\delta \end{Bmatrix} \tag{B.14}$$

The inverse representation can be given as follows.

$$r = |\boldsymbol{r}_c| \tag{B.15}$$

$$\sin\alpha = \frac{y}{\sqrt{x^2+y^2}} \qquad \cos\alpha = \frac{x}{\sqrt{x^2+y^2}} \tag{B.16}$$

$$\sin\delta = \frac{z}{r} \qquad \cos\delta = \frac{\sqrt{x^2+y^2}}{r} \tag{B.17}$$

$$\dot{r} = \frac{\boldsymbol{r}_c \cdot \boldsymbol{v}_c}{r} \tag{B.18}$$

$$\dot{\alpha} = \frac{\dot{x}y - \dot{y}x}{-y^2 - x^2} \tag{B.19}$$

$$\dot{\delta} = \frac{\dot{z} - \dot{r}\left(\frac{z}{r}\right)}{\sqrt{x^2+y^2}} \tag{B.20}$$

# Appendix C

# Breakup model

This appendix describes theories of the NASA standard breakup model 2001 revision (Johnson *et al.*, 2001), involved in the OD generation process in the dissertation. According to (Johnson *et al.*, 2001), the NASA standard breakup model 2001 revision is an empirical model depended on data collected since the early 1980's, including:

1. the Solwind (P-78) (Kling, 1986) and the USA 19 (Delta-180) (Johnson, 1986; Kling, 1987) deliberate hypervelocity collisions in low Earth orbit in 1985 and 1986, respectively
2. the ground-based Satellite Orbital Debris Characterization Impact Test (SOCIT) series in 1991 and 1992 (McKnight *et al.*, 1995)
3. the Ariane upper stage sub-scale explosion tests supervised by the European Space Agency (Fucke & Sdunnus, 1993)
4. an extensive compilation of historical orbital data (i.e., TLE sets) for explosion and collision debris used to determine ejection velocity and area-to-mass ratio distributions (Reynolds *et al.*, 1998)

The NASA standard breakup model 2001 revision consists of three models that describe initial states of fragmentation debris at breakup, including the size distribution model, the A/m distribution model, and the $\Delta V$ distribution model. The size distribution model is different between explosion breakup and collision breakup so that this appendix focuses on the explosion breakup mode, which is applied to the dissertation.

Figure C.1 illustrates a workflow of the OD generation in the NASA standard breakup model 2001 revision. The size distribution model is functions of the size of debris and the

scaling factor. Once the scaling factor ($S$) and the lower threshold of the size ($L_c$) is given, the number of debris to be generated is determined. For each debris, A/m and $\Delta V$ are evaluated based on probability density functions. The A/m distribution model is a function of the size of individual debris. On the other hand, the $\Delta V$ distribution model is a function of the A/m of individual debris determined by the A/m distribution model. The generation of OD is repeated based on the workflow (Figure. C.1) until the number of debris generated reaches the number of debris to be generated, which is determined by the size distribution model. Equations for the size distribution model, the A/m distribution model, and the $\Delta V$ distribution model are introduced in the following paragraphs.

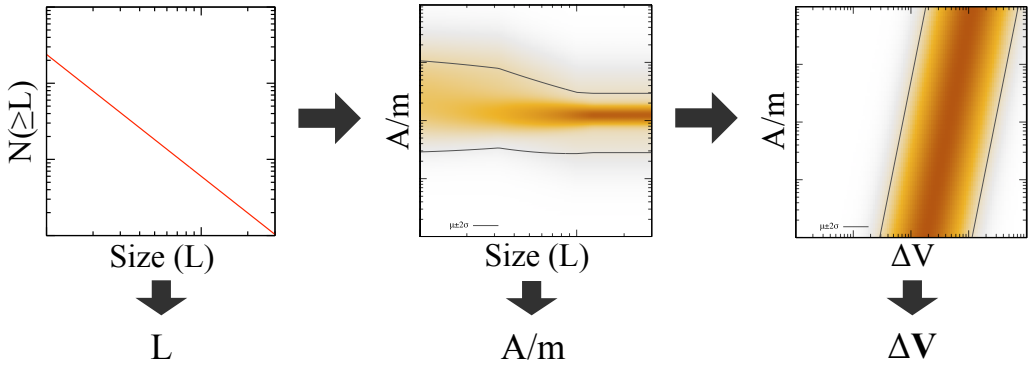


**Figure C.1: A sequence of OD generation in the NASA standard breakup model 2001 revision.**

The number of explosion fragments of size $L_c$, or larger, in meters, is governed by the following equation:

$$N(L_c) = S\,6L_c^{-1.6} \tag{C.1}$$

where $S$ is the scaling factor, which is a type-dependent, unit-less number.

The A/m distribution model distinguishes the distribution functions between the upper-stage fragments and the spacecraft fragments whose size ($L_c$) is larger than 11 cm. The distribution function for upper stage fragments with $L_c$ larger than 11 cm is given by

$$\begin{aligned} D_{A/m}^{\mathrm{R/B}}(\lambda_c, x) &= \alpha^{\mathrm{R/B}}(\lambda_c) N(\mu_1^{\mathrm{R/B}}(\lambda_c), \sigma_1^{\mathrm{R/B}}(\lambda_c), x) \\ &\quad + (1 - \alpha^{\mathrm{R/B}}(\lambda_c)) N(\mu_2^{\mathrm{R/B}}(\lambda_c), \sigma_2^{\mathrm{R/B}}(\lambda_c), x) \end{aligned} \tag{C.2}$$

where $\lambda_c$, the variable $x$, and the normal distribution function $N$ are given as follows.

$$\lambda_c = \log_{10}(L_c) \tag{C.3}$$

$$x = \log_{10}(A/m) \tag{C.4}$$

$$N(\mu, \sigma, x) = \frac{1}{\sigma\sqrt{2\pi}} \exp\left(\frac{-(x-\mu)^2}{2\sigma^2}\right) \tag{C.5}$$

The weighted parameter $\alpha^{\mathrm{R/B}}$, the mean values $\mu_1^{\mathrm{R/B}}$, $\mu_2^{\mathrm{R/B}}$, and the standard deviations $\sigma_1^{\mathrm{R/B}}$, $\sigma_2^{\mathrm{R/B}}$ are defined as follows.

$$\alpha^{\mathrm{R/B}} = \begin{cases} 1 & (\lambda_c \leq -1.4) \\ 1 - 0.3571(\lambda_c + 1.4) & (-1.4 < \lambda_c < 0) \\ 0.5 & (\lambda_c \geq 0) \end{cases} \tag{C.6}$$

$$\mu_1^{\mathrm{R/B}} = \begin{cases} -0.45 & (\lambda_c \leq -0.5) \\ -0.45 - 0.9(\lambda_c + 0.5) & (-0.5 < \lambda_c < 0) \\ -0.9 & (\lambda_c \geq 0) \end{cases} \tag{C.7}$$

$$\sigma_1^{\mathrm{R/B}} = 0.55 \tag{C.8}$$

$$\mu_2^{\mathrm{R/B}} = -0.9 \tag{C.9}$$

$$\sigma_2^{\mathrm{R/B}} = \begin{cases} 0.28 & (\lambda_c \leq -1.0) \\ 0.28 - 0.1636(\lambda_c + 1) & (-1.0 < \lambda_c < 0.1) \\ 0.1 & (\lambda_c \geq 0.1) \end{cases} \tag{C.10}$$

The corresponding distribution function for spacecraft fragments with size $L_c$ larger than 11 cm is given by

$$\begin{aligned} D_{A/m}^{\mathrm{S/C}}(\lambda_c, x) = {} & \alpha^{\mathrm{S/C}}(\lambda_c) N(\mu_1^{\mathrm{S/C}}(\lambda_c), \sigma_1^{\mathrm{S/C}}(\lambda_c), x) \\ & + (1 - \alpha^{\mathrm{S/C}}(\lambda_c)) N(\mu_2^{\mathrm{S/C}}(\lambda_c), \sigma_2^{\mathrm{S/C}}(\lambda_c), x) \end{aligned} \tag{C.11}$$

where

$$\alpha^{\mathrm{S/C}} = \begin{cases} 0 & (\lambda_c \leq -1.95) \\ 0.3 + 0.4(\lambda_c + 1.2) & (-1.95 < \lambda_c < 0.55) \\ 1 & (\lambda_c \geq 0.55) \end{cases} \tag{C.12}$$

$$\mu_1^{\mathrm{S/C}} = \begin{cases} -0.6 & (\lambda_c \leq -1.1) \\ -0.6 - 0.318(\lambda_c + 1.1) & (-1.1 < \lambda_c < 0) \\ -0.95 & (\lambda_c \geq 0) \end{cases} \tag{C.13}$$

$$\sigma_1^{\mathrm{S/C}} = \begin{cases} 0.1 & (\lambda_c \leq -1.3) \\ 0.1 + 0.2(\lambda_c + 1.3) & (-1.3 < \lambda_c < -0.3) \\ 0.3 & (\lambda_c \geq -0.3) \end{cases} \tag{C.14}$$

$$\mu_2^{\mathrm{S/C}} = \begin{cases} -1.2 & (\lambda_c \leq -0.7) \\ -1.2 - 1.333(\lambda_c + 0.7) & (-0.7 < \lambda_c < -0.1) \\ -2.0 & (\lambda_c \geq -0.1) \end{cases} \tag{C.15}$$

$$\sigma_2^{\mathrm{S/C}} = \begin{cases} 0.5 & (\lambda_c \leq -0.5) \\ 0.5 - (\lambda_c + 0.5) & (-0.5 < \lambda_c < -0.3) \\ 0.3 & (\lambda_c \geq -0.3) \end{cases} \tag{C.16}$$

For objects with $L_c$ smaller than 8 cm, a single A/M distribution function for both of upper stages fragments and spacecraft fragments as follows.

$$D_{A/m}^{\mathrm{SOC}}(\lambda_c, x) = N(\mu^{\mathrm{SOC}}(\lambda_c), \sigma^{\mathrm{SOC}}(\lambda_c), x) \tag{C.17}$$

where

$$\mu^{\mathrm{SOC}} = \begin{cases} -0.3 & (\lambda_c \leq -1.75) \\ -0.3 - 1.4(\lambda_c + 1.75) & (-1.75 < \lambda_c < -1.25) \\ -1.0 & (\lambda_c \geq -1.25) \end{cases} \tag{C.18}$$

$$\sigma^{\mathrm{SOC}} = \begin{cases} 0.2 & (\lambda_c \leq -3.5) \\ 0.2 + 0.1333(\lambda_c + 3.5) & (\lambda_c > -3.5) \end{cases} \tag{C.19}$$

In the generation of fragments in the size range (8cm $\leq$ $L_c$ < 11cm), an A/m distribution function is probabilistically adopted by judging if a normalized size parameter $\lambda_n$ is greater than or less than a value ($\lambda_p$) returned by a uniform probability density function whose range is [0.0,1.0). The normalized size parameter $\lambda_n$ is

$$\lambda_n = \frac{\lambda_c - \log_{10} 0.08}{\log_{10} 0.11 - \log_{10} 0.08} \tag{C.20}$$

For upper stage fragments, (8cm $\leq$ $L_c$ < 11cm), the A/m distribution $D_{A/m}$ is adopted as follows.

$$D_{A/m} = \begin{cases} D_{A/m}^{\mathrm{SOC}} & (\lambda_n < \lambda_p) \\ D_{A/m}^{\mathrm{R/B}} & (\lambda_n \geq \lambda_p) \end{cases} \tag{C.21}$$

For spacecraft fragments (8cm $\leq$ $L_c$ < 11cm), the A/m distribution $D_{A/m}$ is adopted in the same manner as follows.

$$D_{A/m} = \begin{cases} D_{A/m}^{\mathrm{SOC}} & (\lambda_n < \lambda_p) \\ D_{A/m}^{\mathrm{S/C}} & (\lambda_n \geq \lambda_p) \end{cases} \tag{C.22}$$

Using A/m as the independent variable instead of $L_c$, The $\Delta V$ distribution model for explosion fragments is given as follows.

$$D_{\Delta V}^{\mathrm{EXP}}(x, \nu) = N(\mu^{\mathrm{EXP}}(x), \sigma^{\mathrm{EXP}}(x), \nu) \tag{C.23}$$

where

$$x = \log_{10}(A/M) \tag{C.24}$$

$$\nu = \log_{10}(\Delta V) \tag{C.25}$$

$$\mu^{\mathrm{EXP}} = 0.2x + 1.85 \tag{C.26}$$

$$\sigma^{\mathrm{EXP}} = 0.4 \tag{C.27}$$

It should be noted that a uniform probability density function is assumed to evaluate directional components of $\Delta V$ of each fragment in the dissertation.

# Appendix D

# Orbit propagation

This appendix describes the general perturbation theories and the special perturbation theories, adopted in the orbit propagation in the dissertation. The general perturbation theories are applied to effectively and accurately propagate several tens of thousands of orbits of breakup fragments generated by the NASA standard breakup model 2001 revisionfor the hypotheses formulation in the search strategy. Whereas, conventional special perturbation theories are convenient to propagate the orbits of the relatively small number of catalogued OD and observed OD to be applied in the origin identification. Following sections describe the general perturbation theories and the special perturbation theories.

## D.1 General perturbation theory

This dissertation organizes the general perturbation theories, which can be found in Vallado (2001). Secular term and long term perturbations are considered in the theories to account for long-term orbit propagation.

### D.1.1 Equation of motion

The Lagrangian planetary equations of motion can derive the rate of changes of orbital elements by solving the partial derivatives of a perturbing function denoted by $R$. The Lagrangian

planetary equations of motion are given by

$$\frac{da}{dt} = \frac{2}{na}\frac{\partial R}{\partial M} \tag{D.1}$$

$$\frac{de}{dt} = \frac{1-e^2}{na^2 e}\frac{\partial R}{\partial M} - \frac{\sqrt{1-e^2}}{na^2 e}\frac{\partial R}{\partial \omega} \tag{D.2}$$

$$\frac{di}{dt} = \frac{1}{na^2\sqrt{1-e^2}\sin i}\left(\cos i\frac{\partial R}{\partial \omega} - \frac{\partial R}{\partial \Omega}\right) \tag{D.3}$$

$$\frac{d\Omega}{dt} = \frac{1}{na^2\sqrt{1-e^2}\sin i}\frac{\partial R}{\partial i} \tag{D.4}$$

$$\frac{d\omega}{dt} = \frac{\sqrt{1-e^2}}{na^2 e}\frac{\partial R}{\partial e} - \frac{d\Omega}{dt}\cos i \tag{D.5}$$

$$\frac{dM_0}{dt} = -\frac{2}{na}\frac{\partial R}{\partial a} - \sqrt{1-e^2}\left(\frac{d\omega}{dt} + \frac{d\Omega}{dt}\cos i\right) \tag{D.6}$$

where $a$, $e$, $i$, $\Omega$, $\omega$ and $M$ represent classical orbital elements, corresponding to the semi-major axis, eccentricity, inclination, right ascension of the ascending node, argument of perigee, and mean anomaly, respectively. $M_0$ denotes the initial mean anomaly. $n$ denotes mean motion.

The Gaussian planetary equations of motion can derive the rate of changes of orbital elements based on the disturbing force acting on OD in the $RSW$ coordinate system . The Gaussian planetary equations of motion are given by

$$\frac{da}{dt} = \frac{2}{n\sqrt{1-e^2}}\left[e\sin f \cdot F_r + (1+e\cos f)F_s\right] \tag{D.7}$$

$$\frac{de}{dt} = \frac{\sqrt{1-e^2}}{na}\left[\sin f \cdot F_r + \left(\cos f + \frac{e+\cos f}{1+e\cos f}\right)F_s\right] \tag{D.8}$$

$$\frac{di}{dt} = \frac{r\cos u}{na^2\sqrt{1-e^2}}F_w \tag{D.9}$$

$$\frac{d\Omega}{dt} = \frac{r\sin u}{na^2\sqrt{1-e^2}\sin i}F_w \tag{D.10}$$

$$\frac{d\omega}{dt} = \frac{\sqrt{1-e^2}}{nae}\left[\cos f \cdot F_r - \left(\sin f + \frac{\sin f}{1+e\cos f}\right)F_s\right] - \frac{d\Omega}{dt}\cos i \tag{D.11}$$

$$\frac{dM_0}{dt} = n - \frac{2r}{na^2}F_r - \sqrt{1-e^2}\left(\frac{d\omega}{dt} + \frac{d\Omega}{dt}\cos i\right) \tag{D.12}$$

where $F_r$, $F_s$ and $F_w$ represent the disturbing forces, $f$ denotes true anomaly, $r$ denotes geocentric radius, and $u$ is defined as $u = \omega + f$.

### D.1.2 Integrator

To integrate the aforementioned planetary equations of motion in orbit propagation, the Euler integrator (after Leonhard Euler), which is simply a first-order Taylor series, is adopted based on (Vallado, 2001).

$$y(t) \cong y(t_0) + \frac{dy(t_0)}{dt}(t - t_0) \tag{D.13}$$

The time step $(t - t_0)$ is set to be 5 days to adequately track the perturbations.

### D.1.3 Force models

The Lagrangian planetary equations of motion is applied to derive the rate of changes of orbital elements due to the Earth gravitational potential ($J_2$ term) and third body forces (the Sun and the Moon). Whereas, the Gaussian planetary equations of motion is applied to derive the rate of changes of orbital elements due to SRP. Following sections describe the derived equations for each perturbation force.

#### D.1.3.1 Earth gravitational potential ($J_2$ term)

A general method to obtain first-order solution will be described here according to Vinti *et al.* (1998). This method uses true anomaly $f$ as an independent variable, and this procedure will enable to treat the case of eccentricities close to unity.

Letting a perturbing function denoted by $R$ to be separated into a part $\bar{R}$ that is constant in the first approximation and a part $\tilde{R}$ that is short periodic. Then $\bar{R}$ gives rise to secular variations proportional to the time $t$ and $\tilde{R}$ to short periodic variations. Therefore,

$$\bar{R} = \frac{1}{P}\int_0^P R dt = \frac{1}{2\pi}\int_0^{2\pi} R dM \tag{D.14}$$

where $P$ is the period of the unperturbed orbit. In calculation of the first-order perturbations, we begin with unperturbed quantities on the right sides of the variational equations, so that

among these quantities we have the relations

$$dM = ndt \tag{D.15}$$

$$P = \frac{2\pi}{n} \tag{D.16}$$

$$n = \sqrt{\frac{\mu}{a^3}} \tag{D.17}$$

$$r^2\frac{df}{dt} = na^2\sqrt{1-e^2} \tag{D.18}$$

where $\mu$ represents the Earth's gravitational constant. From these equations, one obtains

$$dM = \frac{1}{\sqrt{1-e^2}}\left(\frac{r}{a}\right)^2 df \tag{D.19}$$

From Eqs.(D.14) and (D.35), we find

$$\bar{R} = \frac{1}{2\pi}\int_0^{2\pi} \frac{R}{\sqrt{1-e^2}}\left(\frac{r}{a}\right)^2 df \tag{D.20}$$

A general form of the perturbation function due to the Earth gravitational potential, $R_{Earth}$, is given by

$$R_{Earth} = \sum_{l=0}^{\infty}\sum_{m=0}^{l}\frac{\mu}{r}\left(\frac{a_e}{r}\right)^l P_{l,m}(\sin\phi)(C_{l,m}\cos m\lambda + S_{l,m}\sin m\lambda) \tag{D.21}$$

where $a_e$ is the mean equatorial radius of the Earth, $\phi$ is the geocentric latitude, $\lambda$ is the geocentric longitude, $P_{l,m}$ is the associated Legendre polynomials, and $C_{l,m}$ and $S_{l,m}$ are the coefficients to represent the Earth gravitational potential distribution. The perturbation function due to a second-order zonal harmonics (i.e., $l$=2 and $m$=0), $R_2$, is given by

$$R_2 = \frac{\mu}{r}J_2\left(\frac{a_e}{r}\right)^2 P_{2,0}(\sin\phi) = \frac{\mu J_2 a_e^2}{2r^3}(1-3\sin^2 i\sin^2 u) \tag{D.22}$$

where $J_2 \equiv -C_{2,0}$. Substituting Eq.(D.22) into Eq.(D.20), we obtain the first-order perturbation function by $J_2$ term, $\bar{R}_2$, as follows.

$$\begin{aligned}\bar{R}_2 &= \frac{\mu J_2 a_e^2}{4\pi a^3\sqrt{1-e^2}}\int_0^{2\pi}(1-3\sin^2 i\sin^2 u)\frac{a}{r}df \\ &= \frac{\mu J_2 a_e^2}{2a^3(1-e^2)^{\frac{3}{2}}}\left(1-\frac{3}{2}\sin^2 i\right)\end{aligned} \tag{D.23}$$

Substituting the resulting equation into the the Lagrangian planetary equations of motion, then we obtain

$$\frac{da}{dt} = 0 \tag{D.24}$$

$$\frac{de}{dt} = 0 \tag{D.25}$$

$$\frac{di}{dt} = 0 \tag{D.26}$$

$$\frac{d\Omega}{dt} = -\frac{3}{2}\frac{J_2 a_e^2}{\left(a(1-e^2)\right)^2} n \cos i \tag{D.27}$$

$$\frac{d\omega}{dt} = \frac{3}{2}\frac{J_2 a_e^2}{\left(a(1-e^2)\right)^2} n\left(1 - \frac{3}{2}\sin^2 i\right) - \frac{d\Omega}{dt}\cos i \tag{D.28}$$

$$\frac{dM_0}{dt} = 3\frac{J_2 a_e^2}{\left(a(1-e^2)\right)^2} n\sqrt{1-e^2}\left(1 - \frac{3}{2}\sin^2 i\right) - \sqrt{1-e^2}\left(\frac{d\omega}{dt} + \frac{d\Omega}{dt}\cos i\right) \tag{D.29}$$

#### D.1.3.2 Third body forces

Letting a perturbing function due to the i-th body denoted by $R_i$ to be separated into a part $\bar{R}_i$ that is constant in the first approximation and a part $\tilde{R}_i$ that is short periodic. Then, $\bar{R}_i$ gives rise to secular variations proportional to the time $t$ and $\tilde{R}_i$ to short periodic variations. Therefore,

$$\bar{R}_i = \frac{1}{P}\int_0^P R_i dt = \frac{1}{2\pi}\int_0^{2\pi} R_i dM \tag{D.30}$$

In calculation of the first-order perturbations, we begin with unperturbed quantities on the right hand sides of the variational equations, so that among these quantities we have the relations

$$dM = ndt \tag{D.31}$$

$$P = \frac{2\pi}{n} \tag{D.32}$$

$$M \equiv E - e\sin E \tag{D.33}$$

$$r = a(1 - e\cos E) \tag{D.34}$$

where $E$ is the eccentric anomaly. From these equations, we obtain

$$dM = \left(\frac{r}{a}\right)dE \tag{D.35}$$

Thus, from Eqs.(D.30) and (D.35), we find

$$\bar{U}_i = \frac{1}{2\pi}\int_0^{2\pi} U_i\Big(\frac{r}{a}\Big)dE \tag{D.36}$$

The perturbing function due to the i-th body, $U_i$, can be expressed by

$$U_i = \frac{Gm_i}{|\boldsymbol{r_i} - \boldsymbol{r}|} - \frac{Gm_i}{r_i^3}(\boldsymbol{r_i}\cdot\boldsymbol{r}) \tag{D.37}$$

where $G$ represents the universal gravitational constant, $m_i$ is the mass of the i-th body, $\boldsymbol{r_i}$ is the geocentric position vector of the i-th body, and $\boldsymbol{r}$ is the geocentric position vector of the satellite. If $r_i \gg r$, then for $1/|\boldsymbol{r_i} - \boldsymbol{r}|$ we can use the following approximation form:

$$\frac{1}{|\boldsymbol{r_i} - \boldsymbol{r}|} \approx \frac{1}{r_i}\Big[1 + \frac{\boldsymbol{r_i}\cdot\boldsymbol{r}}{r_i^2} + \frac{3}{2}\frac{(\boldsymbol{r_i}\cdot\boldsymbol{r})^2}{r_i^4} - \frac{1}{2}\frac{r^2}{r_i^2} + \Big\{\frac{5}{2}\frac{(\boldsymbol{r_i}\cdot\boldsymbol{r})^3}{r_i^6} - \frac{3}{2}\frac{\boldsymbol{r_i}\cdot\boldsymbol{r}}{r_i^2}\frac{r^2}{r_i^2}\Big\}\Big] \tag{D.38}$$

The third order terms ({ } part in the above equation) can be neglected for the Sun but up to third order terms for the Moon should be taken into account. Substituting the above equation into the perturbing function, then we can obtain

$$R_i \approx \frac{Gm_i}{r_i}\Big[\frac{3}{2}\frac{(\boldsymbol{r_i}\cdot\boldsymbol{r})^2}{r_i^4} - \frac{1}{2}\frac{r^2}{r_i^2} + \Big\{\frac{5}{2}\frac{(\boldsymbol{r_i}\cdot\boldsymbol{r})^3}{r_i^6} - \frac{3}{2}\frac{\boldsymbol{r_i}\cdot\boldsymbol{r}}{r_i^2}\frac{r^2}{r_i^2}\Big\}\Big] \tag{D.39}$$

$(\boldsymbol{r_i}\cdot\boldsymbol{r})/r_i^2$ can be expressed by

$$\frac{\boldsymbol{r_i}\cdot\boldsymbol{r}}{r_i^2} = \frac{r}{r_i}(p\cos f + q\sin f) = \frac{a}{r_i}\Big(p(\cos E - e) + q\sqrt{1-e^2}\sin E\Big) \tag{D.40}$$

The relation between $(p, q, w)$ and the geocentric cosine direction $(l, m, n)$ form for the i-th body can be expressed by

$$\begin{Bmatrix} p \\ q \\ w \end{Bmatrix} = {}^{PQW}[R]_{IJK}\begin{Bmatrix} l \\ m \\ n \end{Bmatrix} \tag{D.41}$$

where $(l, m, n)$ is denoted as

$$\begin{Bmatrix} l \\ m \\ n \end{Bmatrix} = \begin{Bmatrix} \cos\beta\cos\lambda \\ \cos\epsilon\cos\beta\sin\lambda - \sin\epsilon\sin\beta \\ \sin\epsilon\cos\beta\sin\lambda + \cos\epsilon\sin\beta \end{Bmatrix} \tag{D.42}$$

where $\lambda$ represents ecliptic longitude, $\beta$ ecliptic latitude, $\epsilon$ obliquity.

Averaging the perturbing function due to the i-th body, $R_i$, over a revolution, then we obtain

$$\begin{aligned}\bar{R}_i &= \frac{1}{4}\frac{Gm_i}{r_i}\left(\frac{a}{r_i}\right)^2(3p^2+3q^2-2+3e^2(rp^2-q^2-1)) \\ &\quad -\left\{\frac{5}{16}\frac{Gm_i}{r_i}\left(\frac{a}{r_i}\right)^3 ep(3(5p^2+5q^2-4)+e^2(20p^2-15q^2-9))\right\} \end{aligned} \tag{D.43}$$

Therefore, the rates of change in the orbital elements may be given by

$$\frac{da}{dt} = 0 \tag{D.44}$$

$$\begin{aligned}\frac{de}{dt} &= -\frac{15}{2}\frac{\sqrt{1-e^2}}{na}\frac{Gm_i}{r_i^2}\frac{a}{r_i}(epq) \\ &\quad +\left\{\frac{15}{16}\frac{\sqrt{1-e^2}}{na}\frac{Gm_i}{r_i^2}\left(\frac{a}{r_i}\right)^2 q(5p^2+5q^2-4+e^2(30p^2-5q^2-3))\right\} \end{aligned} \tag{D.45}$$

$$\begin{aligned}\frac{di}{dt} &= \frac{3}{2}\frac{w}{na\sqrt{1-e^2}}\frac{Gm_i}{r_i^2}\frac{a}{r_i}((1+4e^2)p\cos\omega-(1-e^2)q\sin\omega) \\ &\quad +\left\{\frac{15}{16}\frac{ew}{na\sqrt{1-e^2}}\frac{Gm_i}{r_i^2}\left(\frac{a}{r_i}\right)^2\right. \\ &\quad \left.\times((15p^2+5q^2-4+e^2(20p^2-5q^2-3))\cos\omega-10(1-e^2)pq\sin\omega)\right\} \end{aligned} \tag{D.46}$$

$$\begin{aligned}\frac{d\Omega}{dt} &= \frac{3}{2}\frac{w\csc i}{na\sqrt{1-e^2}}\frac{Gm_i}{r_i^2}\frac{a}{r_i}((1+4e^2)p\sin\omega+(1-e^2)q\cos\omega) \\ &\quad -\left\{\frac{15}{16}\frac{ew\csc i}{na\sqrt{1-e^2}}\frac{Gm_i}{r_i^2}\left(\frac{a}{r_i}\right)^2\right. \\ &\quad \left.\times((15p^2+5q^2-4+e^2(20p^2-5q^2-3))\sin\omega+10(1-e^2)pq\cos\omega)\right\} \end{aligned} \tag{D.47}$$

$$\begin{aligned}\frac{d\omega}{dt} &= \frac{3}{2}\frac{\sqrt{1-e^2}}{na}\frac{Gm_i}{r_i^2}\frac{a}{r_i}(4p^2-q^2-1) \\ &\quad -\left\{\frac{15}{16}\frac{\sqrt{1-e^2}}{nae}\frac{Gm_i}{r_i^2}\left(\frac{a}{r_i}\right)^2\right. \\ &\quad \left.\times p(5p^2+5q^2-4+e^2(20p^2-15q^2-9))\right\}-\frac{d\Omega}{dt}\cos i \end{aligned} \tag{D.48}$$

$$\begin{aligned}\frac{dM_0}{dt} &= -\frac{1}{na}\frac{Gm_i}{r_i^2}\frac{a}{r_i}(3p^2+3q^2-2+3e^2(4p^2-q^2-1)) \\ &\quad +\left\{\frac{15}{8}\frac{1}{na}\frac{Gm_i}{r_i^2}\left(\frac{a}{r_i}\right)^2\right. \\ &\quad \left.\times ep(3(5p^2+5q^2-4)+e^2(20p^2-15q^2-9))\right\} \\ &\quad -\sqrt{1-e^2}\left(\frac{d\omega}{dt}+\frac{d\Omega}{dt}\cos i\right) \end{aligned} \tag{D.49}$$

#### D.1.3.3 Solar radiation pressure

The solar radiation pressure is not a conservative force so that we cannot use Vinti *et al.* (1998) to obtain first-order solution as in the Earth's zonal harmonics. A method adopted here to obtain first-order solution will starts with the Gaussian planetary equations of motion. Letting the rate of the change of a osculating element denoted by $dF/dt = \dot{F}$ to be separated into a part $\bar{\dot{F}}$ that is constant in the first approximation and a apart $\Delta\dot{F}$ that is short periodic. Then $\bar{\dot{F}}$ gives rise to secular variation proportional to the time $t$ and $\Delta\dot{F}$ to short periodic variations. Therefore,

$$\bar{\dot{F}} = \frac{1}{P}\int_0^P \dot{F}dt = \frac{1}{2\pi}\int_0^{2\pi} \dot{F}dM \tag{D.50}$$

In calculation of the first-order perturbations, we begin with unperturbed quantities on the right sides of the variational equations, so that among these quantities we have the relations

$$dM = ndt \tag{D.51}$$
$$P = \frac{2\pi}{n} \tag{D.52}$$
$$M = E - e\sin E \tag{D.53}$$
$$r = a(1 - e\cos E) \tag{D.54}$$

From these equations, we obtain

$$dM = \left(\frac{r}{a}\right)dE \tag{D.55}$$

From Eqs.(D.50) and (D.55), we find

$$\bar{\dot{F}} = \frac{1}{2\pi}\int_0^{2\pi} \dot{F}\left(\frac{r}{a}\right)dE \tag{D.56}$$

The expression for the acceleration of a satellite due to the solar radiation pressure may be given by

$$\boldsymbol{a} = -P_S C_r \frac{A}{m}\frac{\boldsymbol{e}_{Sun}}{\boldsymbol{r}^2_{Sun}} \tag{D.57}$$

where $P_S$ represents the solar radiation pressure if one assumes that the satellite's surface absorbs all photons and is perpendicular to the incoming radiation. The radiation pressure

coefficient, $C_r$, stands for

$$C_r = 1 + \epsilon \tag{D.58}$$

where $\epsilon$ is the reflectivity. The A/m represents the area-to-mass ratio. $\boldsymbol{r}_{Sun}$ (in AU) represents the distance between the Earth and the Sun and the reciprocal of $\boldsymbol{r}_{Sun}$ squared explains an annual variation of the solar radiation pressure due to the eccentricity of the Earth's heliocentric orbit. Let $\boldsymbol{e}_{Sun}$ expressed in the satellite coordinate system $RSW$.

$$\boldsymbol{e}_{Sun} = \begin{Bmatrix} p\cos f + q\sin f \\ -p\sin f + q\cos f \\ w \end{Bmatrix}_{RSW} \tag{D.59}$$

The relation between $(p, q, w)$ and the geocentric cosine direction of the Sun $(l, m, n)$ can be found in Eq.(D.41). Substituting Eq.(D.59) into Eq.(D.57), then we obtain

$$\boldsymbol{a} = -P_S C_r \frac{A}{m} \frac{1}{r_{Sun}^2} \begin{Bmatrix} p\cos f + q\sin f \\ -p\sin f + q\cos f \\ w \end{Bmatrix}_{RSW} \tag{D.60}$$

Let substitute Eq.(D.60) into the Gaussian planetary equations of motion to obtain the rates of change in the orbital elements due to SRP for a satellite in sunlight during the entire orbit are given by

$$\frac{da}{dt} = 0 \tag{D.61}$$

$$\frac{de}{dt} = -\frac{3}{2}\frac{q\sqrt{1-e^2}}{na} \tag{D.62}$$

$$\frac{di}{dt} = \frac{3}{2}\frac{ew\cos\omega}{na\sqrt{1-e^2}} \tag{D.63}$$

$$\frac{d\Omega}{dt} = \frac{3}{2}\frac{ew\sin\omega}{na\sqrt{1-e^2}\sin i} \tag{D.64}$$

$$\frac{d\omega}{dt} = \frac{3}{2}\frac{p\sqrt{1-e^2}}{nae} - \frac{d\Omega}{dt}\cos i \tag{D.65}$$

$$\frac{dM_0}{dt} = -3\frac{ep}{na} - \sqrt{1-e^2}\left(\frac{d\omega}{dt} + \frac{d\Omega}{dt}\cos i\right) \tag{D.66}$$

## D.2 Special perturbation theory

This dissertation adopts Cowell's formulation to conduct orbit propagation by the special perturbation theories. Recalling the equation of motion for the two-body problem, one can generally describe the equation of motion for a satellite under perturbating accelerations, $\boldsymbol{a}_p$, as follows.

$$\ddot{\boldsymbol{r}} = -\frac{\mu}{r^3}\boldsymbol{r} + \boldsymbol{a}_p \tag{D.67}$$

Let $\boldsymbol{r}$ and $\dot{\boldsymbol{r}}$ denote the position vector and the velocity vector of a satellite in *IJK* coordinate system, respectively. It should be noted that perturbing accelerations can be added to Eq.(D.67) linearly. We can organize $\boldsymbol{r}$ and $\dot{\boldsymbol{r}}$ by introducing $\boldsymbol{X}$ as follows.

$$\boldsymbol{X} = \begin{Bmatrix} \boldsymbol{r} \\ \\ \dot{\boldsymbol{r}} \end{Bmatrix} = \begin{Bmatrix} x \\ y \\ z \\ \dot{x} \\ \dot{y} \\ \dot{z} \end{Bmatrix} \tag{D.68}$$

Finally, the second-order differential equation (Eq.(D.67)) can be reduced to the first-order differential equation by differentiating $\boldsymbol{X}$.

$$\frac{d\boldsymbol{X}}{dt} = \begin{Bmatrix} x \\ y \\ z \\ \dot{x} \\ \dot{y} \\ \dot{z} \end{Bmatrix} = \begin{Bmatrix} \dot{x} \\ \dot{y} \\ \dot{z} \\ -\frac{\mu}{r^3}x + a_{px} \\ -\frac{\mu}{r^3}y + a_{py} \\ -\frac{\mu}{r^3}z + a_{pz} \end{Bmatrix} \tag{D.69}$$

Eq.(D.69) can be directly solved by numerical integrators. This dissertation adopts the Adams-Bashforth-Moulton method to solve Eq.(D.69) in variable-step. The gradient of a perturbation function, $R$, appeared in the general perturbation theories can express the perturbing accelerations to be added to Eq.(D.69). Also, there are several modifications for the force models in the special perturbation theories from the general perturbation theories. In calculation of the perturbing acceleration due to the Earth gravitational potential, the geopotential model EGM-96 (Earth Gravitational Model 1996) (Lemoine *et al.*, 1998) is adopted to give precise parameters to each order of the coefficients $C_{l,m}$ and $S_{l,m}$.

In calculation of the SRP perturbation, on the other hand, the shadow analysis is considered to calculate the SRP more accurately. Most satellites including geosynchronous satellites experiences periodic eclipses. Of course, when the satellite is eclipsed, it's not exposed to SRP affecting the satellite dynamics. When we need high accuracy, we must develop models that turn the solar-radiation calculations "on" and "off", as appropriate, to account for these periods of inactivity. Begin by examining the geometry of the problem. We have assumed the Sun is infinitely far from the Earth, so the light rays are parallel, producing a cylindrical Earth shadow of radius $R_{Es}$. Let $\boldsymbol{r}_{Sun}$ and $\boldsymbol{r}$ denote the geocentric position vectors of the Sun and the satellite. The fundamental plane, which is perpendicular to the shadow axis and passes through the satellite, then intersects the shadow axis at a distance from the center of the Earth,

$$s = \boldsymbol{r} \cdot \frac{\boldsymbol{r}_{Sun}}{r_{Sun}} = \boldsymbol{r} \cdot \boldsymbol{e}_{Sun} \tag{D.70}$$

where $\boldsymbol{e}_{Sun}$ represents the unit vector along the geocentric position vector of the Sun. If $s > 0$, then the satellite will be always illuminated by the Sun because the satellite will be always between the Sun and the Earth. For $s < 0$, the satellite could be in the shadow of the Earth when the distance from the shadow axis to the satellite is less than the Earth's radii, then we can obtain the following inequality:

$$|\boldsymbol{r} - s\boldsymbol{e}_{Sun}| = \sqrt{r^2 - s^2} < R_{Es} \tag{D.71}$$

Therefore, the condition that the satellite will be illuminated by the Sun can be expressed by

$$\begin{aligned} s &> 0 \\ &\text{or} \\ \sqrt{r^2 - s^2} &> R_{Es} \end{aligned} \tag{D.72}$$

# References


Bishop, C.M. *et al.* (2006). *Pattern recognition and machine learning*, vol. 1. springer New York. 50

Flohrer, T. (2013). Classification of geosynchronous objects. *GEN-DB-LOG-00101-HSO-GR*. 1

Fucke, W. & Sdunnus, H. (1993). Population model of small size space debris. *Battelle Institut EV Frankfurt Am Main*. 111

Gural, P.S., Larsen, J.A. & Gleason, A.E. (2005). Matched filter processing for asteroid detection. *The Astronomical Journal*, **130**, 1951. 24

Hanada, T. & Matney, M. (2002). Using breakup models and propagators to devise debris search strategies in geo. In *Proceedings of the Ninth International Space Conference of Pacific-Basin Societies*, 373–385. 28

Hanada, T. & Yasaka, T. (2005). Orbital evolution of cloud particles from explosions of geosynchronous objects. *Journal of spacecraft and rockets*, **42**, 1070–1076. 28, 84

Hanada, T., Uetsuhara, M., Yanagisawa, T. & Kitazawa, Y. (2013). Effective search strategy applicable for breakup fragments in the geostationary region. *Journal of Spacecraft and Rockets*, **Accepted**. 5

Ikeda, H., Hanada, T. & Yasaka, T. (2008). Searching for lost fragments in geo. *Acta Astronautica*, **63**, 1312–1317. 28

Johnson, N., Krisko, P., Liou, J.C. & Anz-Meador, P. (2001). Nasa's new breakup model of evolve 4.0. *Advances in Space Research*, **28**, 1377–1384. 7, 13, 34, 52, 63, 70, 72, 83, 89, 111

Johnson, N.L. (1986). The collision of satellites 16937 and 16938: Preliminary report. Tech. rep., CS87-LKD-002, Teledyne Brown Engineering. 111

Johnson, N.L. (2001). Evidence for historical satellite fragmentations in and near the geosynchronous regime. In *Space Debris*, vol. 473, 355–359. 2, 81, 97

Kling, R. (1986). Postmortem of a hypervelocity impact: Summary. *Teledyne Brown Engineering, CS86-LKD-001*. 111

Kling, R. (1987). The collision of satellites 16937 and 16938: Debris characterization. Tech. rep., CS87-LKD-005, Teledyne Brown Engineering. 111

Krag, H. (2002a). Proof-2001. In *Minutes of the 20th Inter-Agency Space Debris Coordination Committee Meeting*. 2

Krag, H. (2002b). Status of master-2001 development. In *Minutes of the 20th Inter-Agency Space Debris Coordination Committee Meeting*, Guildford, UK. 2

Lemoine, F.G., Kenyon, S.C., Factor, J.K., Trimmer, R.G., Pavlis, N.K., Chinn, D.S., Cox, C.M., Klosko, S.M., Luthcke, S.B., Torrence, M.H. *et al.* (1998). The development of the joint nasa gsfc and the national imagery and mapping agency(nima) geopotential model egm 96. *NASA*. 126

McKnight, D., Johnson, N., Fudge, M. & Maclay, T. (1995). Satellite orbital debris characterization impact test (socit) series data collection report. *Kaman Sciences Corp., Contract NAS*, 9–19215. 111

Molotov, I., Agapov, V., Titenko, V., Khutorovsky, Z., Burtsev, Y., Guseva, I., Rumyantsev, V., Ibrahimov, M., Kornienko, G., Erofeeva, A., Biryukov, V., Vlasjuk, V., Kiladze, R., Zalles, R., Sukhov, P., Inasaridze, R., Abdullaeva, G., Rychalsky, V., Kouprianov, V., Rusakov, O., Litvinenko,

## REFERENCES


E. & Filippov, E. (2008). International scientific optical network for space debris research. *Advances in Space Research*, **41**, 1022 – 1028. 1

Molotov, I., Agapov, V., Chestnov, D., Matkin, A. & Lapshin, A. (2012). Observations with survey instruments of the ison network. In *39th COSPAR Scientific Assembly. Held 14-22 July 2012, in Mysore, India. Abstract F2. 4-11-12, p. 1267*, vol. 39, 1267. v, 2, 3

Nelder, J.A. & Mead, R. (1965). A simplex method for function minimization. *The computer journal*, **7**, 308–313. 64

Oswald, M. (2008). *New Contributions to Space Debris Environment Modeling*. Shaker. ix, 2, 51, 62, 81

Pensa, A., Powell, G., Rork, E. & Sridharan, R. (1996). Debris in geosynchronous orbits. *Spaceflight mechanics 1996*, 277–288. 2, 12, 51, 81

Reynolds, R.C., Bade, A., Eichler, P., Jackson, A.A., Krisko, P.H., Matney, M., Kessler, D.J. & Anz-Meador, P.D. (1998). Nasa standard breakup model, 1998 revision. *Lockheed Martin Space and Mission Systems and Services Report LMSMMSS-32532*. 111

Rykhlova, L., Kasimenko, T., Mikisha, A. & Smirnov, M. (1997). Explosions in the geostationary orbit. *Advances in Space Research*, **19**, 313–319. 2, 67, 81

Schildknecht, T., Hugentobler, U. & Ploner, M. (1999). Optical surveys of space debris in geo. *Advances in Space Research*, **23**, 45–54. 1

Schildknecht, T., Hugentobler, U. & Ploner, M. (2000). First geo survey test observations with the esa 1 m telescope in tenerife. In *Proceedings of the 2000 Space Control Conference*, 73–79, DTIC Document. 1

Schildknecht, T., Ploner, M. & Hugentobler, U. (2001). The search for debris in geo. *Advances in Space Research*, **28**, 1291–1299. 2

Space-Track (2013). https://www.space-track.org. 2

Talent, D., Potter, A. & Henize, K. (1997). A search for debris in geo. In *Second European Conference on Space Debris*, vol. 393, 99. 1

Uetsuhara, M. & Hanada, T. (2013a). An iterative search strategy for characterizing spacecraft breakup events. In *Proceedings of the 29th International Symposium on Space Technology and Science*, 2013–r–20. 7

Uetsuhara, M. & Hanada, T. (2013b). Practical method to identify orbital anomaly as spacecraft breakup in the geostationary region. *Advances in Space Research*, **Accepted**. 7

Uetsuhara, M., Hanada, T. & Kitazawa, Y. (2012a). Effective strategy to identify origins of fragments from breakups in geo. *Advances in the Astronautical Sciences*, **142**. 6

Uetsuhara, M., Hanada, T., Yamaoka, H., Yanagisawa, T., Kurosaki, H. & Kitazawa, Y. (2012b). Strategy to search fragments from breakups in geo. *Advances in Space Research*, **49**, 1151–1159. 5

Uetsuhara, M., Hanada, T., Yanagisawa, T. & Kitazawa, Y. (2013a). A search for possible breakup fragments in the geostationary region. In *Proceedings of the 6th European Conference on Space Debris*, 1a.P–20. 7

Uetsuhara, M., Hanada, T., Yanagisawa, T. & Kitazawa, Y. (2013b). Spacecraft explosion event characterization using correlated observations. In *Proceedings of the 23rd AAS/AIAA Space Flight Mechanics Meeting*, AAS13–315. 7

Uetsuhara, M., Yanagisawa, T., Kinoshita, D., Hanada, T. & Kitazawa, Y. (2013c). Observation campaign dedicated to 1968-081e fragments identification. *Advances in Space Research*, **51**, 2207–2215. 7

Vallado, D.A. (2001). *Fundamentals of astrodynamics and applications*, vol. 12. Springer. 64, 101, 117, 119

Vinti, J.P., Der, G.J. & Bonavito, N.L. (1998). *Orbital and celestial mechanics*, vol. 177. Aiaa. 119, 124

Yanagisawa, T. & Umehara, H. (2009). Strategy for detection of eccentric objects near the geosynchronous region. *Acta Astronautica*, **65**, 1001–1006. 27

Yanagisawa, T., Nakajima, A., Kadota, K.I., Kurosaki, H., Nakamura, T., Yoshida, F., Dermawan, B. & Sato, Y. (2005). Automatic detection algorithm for small moving objects. *Publications of the Astronomical Society of Japan*, **57**, 399–408. 26

Yanagisawa, T., Kurosaki, H. & Nakajima, A. (2009). Activities of jaxa's innovative technology center on space debris observation. In *Advanced Maui Optical and Space Surveillance Technologies Conference, Poster presentations*. 23, 40

Yanagisawa, T., Hanada, T., Kurosaki, H., Kitazawa, Y., Uetsuhara, M. & Kinoshita, D. (2012). Detection of small sized geo debris using fpga based stacking method. In *39th COSPAR Scientific Assembly. Held 14-22 July 2012, in Mysore, India. Abstract E1. 9-10-12, p. 2196*, vol. 39, 2196. 57, 71